

Optical properties of ion beam modified waveguide
materials doped with erbium and silver

*Optical properties of ion beam modified waveguide materials
doped with erbium and silver*
Christof Strohhofer

ISBN 90-9015330-6

A digital version of this thesis can be downloaded from <http://www.amolf.nl>

Optical properties of ion beam modified waveguide materials doped with erbium and silver

Optische eigenschappen van lichtgeleider materialen gedoteerd met erbium en zilver en bestraald met ionenbundels

(met een samenvatting in het Nederlands)

Proefschrift

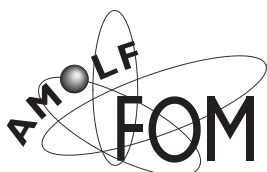
ter verkrijging van de graad van doctor aan de Universiteit Utrecht
op gezag van de Rector Magnificus, Prof. Dr. W. H. Gispen,
ingevolge het besluit van het College voor Promoties
in het openbaar te verdedigen
op maandag 10 december 2001 des ochtends te 10.30 uur

door

Christof Strohhofer

geboren op 22 juni 1970 te Nürnberg

Promotor: Prof. Dr. A. Polman
Faculteit der Natuur- en Sterrenkunde, Universiteit Utrecht
FOM-Instituut voor Atoom- en Molecuulfysica, Amsterdam



The work described in this thesis was performed at the FOM Institute for Atomic and Molecular Physics, Kruislaan 407, 1098 SJ Amsterdam, The Netherlands. It is part of the research programme of the Foundation for Fundamental Research on Matter (FOM), and was made possible by financial support from the Dutch Organisation for the Advancement of Research (NWO), IOP Electro-Optics, the ESPRIT basic research programme SCOOP of the European Union, and Symmorphix, Inc.

Contents

1 What this thesis is about ... 1

The work reported in this thesis is put into perspective within the developments in integrated optics and optical communication technology.

I Codoping erbium doped waveguides 9

2 Selective modification of the Er^{3+} ${}^4\text{I}_{11/2}$ branching ratio by energy transfer to Eu^{3+} 11

This chapter describes the effect of Eu^{3+} on the transition between the second and first excited states of Er^{3+} in Y_2O_3 . By means of selective energy transfer, this transition can be accelerated, effectively relocating population from the second to the first excited state.

3 Enhancement of Er^{3+} ${}^4\text{I}_{13/2}$ population by energy transfer to Ce^{3+} 23

This chapter describes the influence of Ce^{3+} on the luminescent properties of Er^{3+} in Y_2O_3 . As europium in chapter 2, cerium codoping enhances the transition rate between the second and first excited states of Er^{3+} . A comparison with the results of chapter 2 is made.

4 Absorption and emission spectroscopy in Er^{3+} - Yb^{3+} doped aluminum oxide waveguides 35

In this chapter we obtain absorption cross sections between 400 nm and 1700 nm for Er^{3+} and Yb^{3+} energy levels in Al_2O_3 by waveguide transmission spectroscopy. Yb^{3+} acts as a sensitiser for Er^{3+} . We determine the energy transfer rate constant between Yb^{3+} and Er^{3+} .

| | |
|---|------------|
| 5 Relationship between gain and Yb³⁺ concentration in Er³⁺-Yb³⁺ doped waveguide amplifiers | 49 |
| In this chapter we use the spectroscopic data obtained in chapter 4 to calculate the gain of an Al ₂ O ₃ waveguide amplifier doped with Er ³⁺ and various concentrations of Yb ³⁺ , and pumped at 980 nm. The results show the need for careful optimisation of the Yb ³⁺ concentration. | |
| 6 Energy transfer to Er³⁺ in Ag ion-exchanged glass | 65 |
| The photoluminescence of Er ³⁺ in Ag ion-exchanged waveguides can be efficiently excited in a broad spectral range between 350 nm and 600 nm. This is attributed to silver related defects (e.g. pairs of ions/atoms) in the glass, which absorb light and transfer the energy to Er ³⁺ . | |
| II Silver nanocrystals in silicate glass | 73 |
| 7 Formation mechanism of silver nanocrystals made by ion irradiation of Na⁺ ↔ Ag⁺ ion-exchanged sodalime glass | 75 |
| By ion irradiation of sodalime glass containing Ag ⁺ , silver clusters in the nanometer size range are formed. The formation process appears to be linked to the energy deposited in atomic displacements during the irradiation. | |
| 8 Silver nanocrystal doped waveguides with controlled transmission | 87 |
| In this chapter we derive the optical constants of a glass/Ag nanocrystal composite made by ion irradiation as described in chapter 7. Subsequently the transmission through channel waveguides defined by ion exchange and containing Ag nanocrystals is explained in terms of these optical constants. | |
| 9 Highly dispersive micropatterns in ion-exchanged glass formed by ion irradiation through a mask of colloidal particles | 101 |
| We apply the high refractive index contrast between ion-exchanged glass before and after irradiation with heavy ions (see chapters 7 and 8) to fabricate a hexagonal diffraction grating. This is achieved by ion irradiation of ion-exchanged glass through a mask formed of self-organised silica colloidal particles. | |
| Bibliography | 109 |
| Summary | 119 |
| Samenvatting | 121 |
| Zusammenfassung | 123 |
| Publications | 125 |
| Dankwoord | 127 |
| Curriculum Vitae | 129 |

Chapter ONE

What this thesis is about ...

1.1 The role of integrated optics in optical communications

It's all about economics! The fierce global competition in the communications sector forces companies to look for ever cheaper ways to transmit data. Glass fibers for optical telecommunications play a crucial role in this effort. Not only are glass fibres less expensive than copper coaxial cables, but only with the development of optical fibre networks have very high, terabit-per-second¹, transmission rates become possible. The physical limit for information transmitted via a light wave is given by half the carrier wave's frequency (around 10^{15} s^{-1}), yet technology for optical communication is still limited by electronics: digital signals have to be generated by laser diodes driven electronically; although the losses of signals in optical fibres approach 0.1 dB/km and pulse broadening (dispersion) can be controlled effectively, periodic amplification and reshaping is necessary; the optical signal has to be converted back to electronic to be understood by everyday appliances such as telephones, faxes, and computers. The last point gains special importance from the fact that hardly any building is connected directly to the optical fibre network yet, and thus signal distribution takes place via the local – electronic – telephone network.

This is where integrated optics makes its appearance. Just as integrated electronics, which proved to be a successful and inexpensive alternative to perform complicated electronic functions and made possible the wide-spread distribution of personal computers, global navigation systems, and talking automobiles, integrated optics attempts to combine several manipulations of the optical signal on a small chip. Instead of

¹Let us take a minute to understand what this means: a terabit, 10^{12} bits, $1.25 \cdot 10^{11}$ letters or digits, 62.5 million pages of typical paperback novels, around 210000 novels, some pretty large libraries — per second. Or, for the post-vinyl, post-paper generation, 190000 CDs — per second. Or about 36 million telephone conversations simultaneously.

converting light into an electronic signal, the photons are manipulated directly. Advantages for the telecom industry: the components are less bulky than fibre optic components and easy to manufacture, little material and ease of manufacture translates to low cost. Advantages for the consumer: it becomes possible to extend the reach of the optical network directly into the homes at a reasonable price.

The functions that integrated optics will have to perform and that are under development include signal splitting and combining, amplification, and switching. Splitters might just distribute one common signal to different users, or select a certain wavelength out of a multi-colour transmission. This latter function has become important with the advent of wavelength multiplexing in fibre optic communications, which makes use of the same fibre for signals of different wavelengths, originally 4, now 16, with 64 demonstrated and 128 and more planned. Amplifiers are one of the key components in data transmission, since they compensate the losses due to transmission and distribution. While erbium doped fibre amplifiers are well-established by now and in use in the most recent transoceanic transmission lines, reducing their size to be compatible with integrated optics has met with some difficulties due to interaction between individual ions in the gain medium. Nonetheless several optical amplifiers have been demonstrated by research groups and further development is now moving to industry. Switches are important in signal distribution. Several kinds have been demonstrated, mostly based on thermo-optic and electro-optic effects. The dream of an all optical switch based purely on nonlinear optical effects has yet to be realised. Combined with an optical amplifier it would constitute an optical transistor, one important step to all optical computing.

1.2 Materials issues in integrated optics

Research and development for integrated optics is faced with two challenges: making the structures by which light is guided and manipulated, and developing the materials from which these structures are made. The materials issue is the more fundamental of the two, since it also plays a role in the fabrication of the structures. The structures themselves, e.g. waveguides, gratings, or photonic crystals, act on the light through a spatial variation of the index of refraction in order to confine or scatter light (cf. figure 1.1 for waveguide structures used in this thesis). This variation can be achieved either by etching, diffusion, or by exploiting photosensitive reactions. The materials issues involved in structure fabrication are evident: to get high-quality, i.e. low-loss components that perform as demanded, it is necessary to know the reaction of each material to each fabrication process and optimise the process parameters accordingly.

Equally important is the choice of materials for their optical properties. Simple waveguides have to be highly transparent at the wavelength of the signal, they have to be fabricated without scattering or absorption centres. The performance of erbium doped amplifiers, for instance, depends crucially on the host material and the doping process. The host material determines the atomic-scale structure around the erbium ions, which in turn, via the crystal field at the position of the erbium ions determines

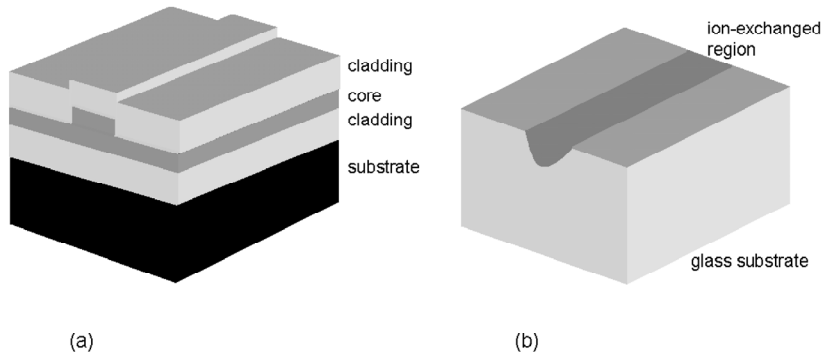


FIGURE 1.1: Examples of two light-guiding structures: (a) partially etched core with high index of refraction between two low-index cladding layers. The light is guided by the thick part of the core. (b) The index of refraction of the core region is increased by substitution of ionic components of the glass. The index profile is not constant, but is determined by diffusion.

the width and oscillator strength of the optical transitions. Optical switches, as another example, rely on the properties of materials to change their index of refraction under the influence of temperature, electric or magnetic fields. As a further requirement, amplification and switching have to be performed efficiently at low levels of supplied power.

There is an infinite number of materials to be explored for each application. Therefore it will take yet a while before an “ideal” material has been identified. As a step towards this goal, great effort is put into improving the properties of existing materials by controlled engineering on the atomic scale. This is the main theme of this thesis: modifying materials by careful choice of dopants and treatments to obtain new or improved optical properties. Our focus is on erbium doped waveguide materials for amplification of light, and on glass containing silver nanocrystals for filtering or possibly switching of light.

1.3 Codoping erbium doped waveguides

The Er^{3+} ion is the gain medium of choice in optical amplifiers for telecommunications. It can emit infrared light around 1530 nm (see figure 1.2 (a)), the wavelength at which most optical telecommunications systems operate. For amplification, population inversion between the first excited state and the ground state has to be reached. This can be achieved by exciting Er^{3+} with radiation at 980 nm into its second excited state. From that energy level the ion relaxes to its first excited state, where the energy is stored, since the decay rate of this level is small.

Sensitising Er^{3+} by suitable codopants has a long history since energy transfer

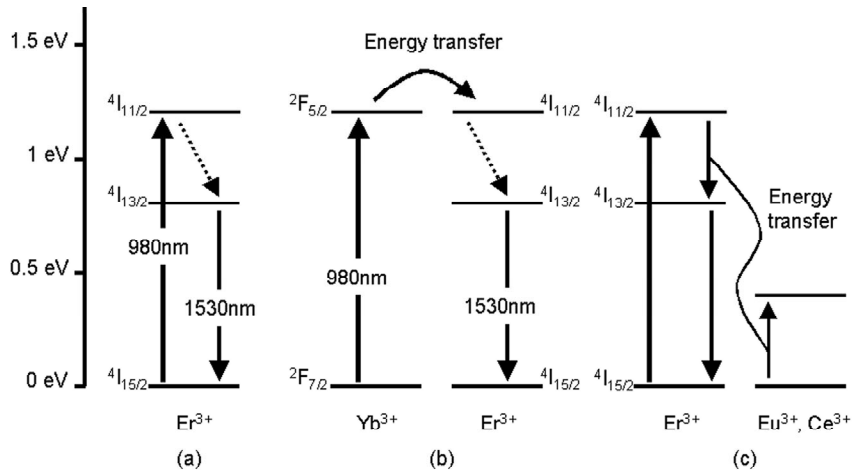


FIGURE 1.2: (a) Energy level diagram of Er^{3+} . For application as an amplifier for 1530 nm light the second excited state is excited with 980 nm radiation. After relaxation to the first excited state amplification at 1530 nm can take place. (b) Sensitisation scheme of Er^{3+} via Yb^{3+} . Most of the pump light is absorbed by Yb^{3+} due to its high absorption cross section at 980 nm. Er^{3+} is excited by energy transfer from Yb^{3+} . (c) Scheme to increase the transition rate between the second and first excited state of Er^{3+} by energy transfer to a suitable acceptor ion.

between rare earth ions has been explored systematically by Auzel (1973). A weak absorption at a given wavelength can be compensated for by introducing a second rare earth that absorbs light more efficiently and transfers the absorbed energy to Er^{3+} . Yb^{3+} is a well-known example of such a sensitizer (see figure 1.2 (b)). The absorption cross section of Yb^{3+} at 980 nm is higher by an order of magnitude than that of Er^{3+} . Since the energies of the second excited state of Er^{3+} and the first excited state of Yb^{3+} are approximately equal, energy can be transferred from an excited Yb^{3+} to an unexcited Er^{3+} via dipolar interaction (Förster, 1948; Dexter, 1953). This is an example for energy transfer into the ensemble of Er^{3+} ions.

The inverse process is of course also possible, namely the removal of excess energy from Er^{3+} . This may become necessary in materials with low phonon energies, where the transition rate between second and first excited state of Er^{3+} is small. In this case only little of the absorbed energy reaches the first excited state. Suitable codopants, like Ce^{3+} , Eu^{3+} , or Tb^{3+} , can accept the energy difference between the second and first excited states of Er^{3+} (see figure 1.2 (c)). This energy transfer increases the transition rate from the second to the first excited state of Er^{3+} and enhances the population in the latter.

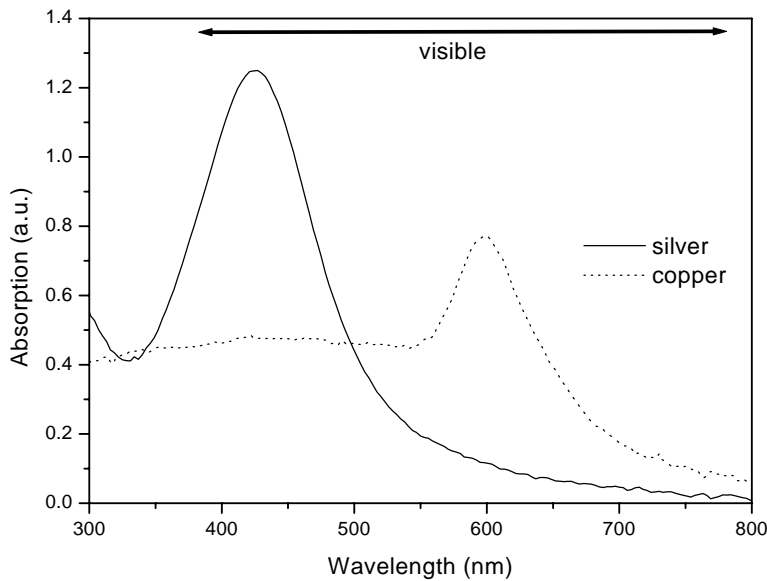


FIGURE 1.3: Absorption of silver nanocrystals in glass and of copper nanocrystals in Al_2O_3 . The broad peaks seen in both spectra are due to the surface plasmon resonances of the metal particles.

1.4 Silver nanocrystals in silicate glass

Glass/metal nanoparticle composites have been in use for centuries as coloured glasses in church windows and other works of art. These composites absorb light in a distinct wavelength region depending on the metal. As figure 1.3 shows, small silver particles will produce a yellow coloration of the glass because they absorb in the blue, while copper particles absorb in the red and give the glass a blue appearance. The optical absorption takes place via generation of surface plasmons, collective excitations of the conduction electrons in the nanoscale particles. This behaviour has been described by Mie (1908).

Research on the linear and especially the nonlinear optical properties of glass/metal nanoparticle composites has seen an enormous boom over recent years. The reason is that these composites have large third order nonlinear susceptibilities of the order of 10^{-9} esu and above in the spectral region of the plasmon band. These nonlinear susceptibilities increase when the size of the metal nanocrystals is reduced. With nonlinear optical properties like these, an all optical switch seemed feasible. Chances, however, are slight that one based on these glass/metal composites will ever work well enough for applications, due to a strong two-photon absorption between electronic bands of the metals. This means that the signal propagating in such a device is not only reduced by the linear absorption of the plasmon resonance, but also by the

additional nonlinear absorption caused by the light necessary to achieve a nonlinear effect.

Nonetheless glass/metal nanoparticle composites have interesting properties for applications. Both their linear and nonlinear absorption can be used for integrated optic devices, like filters and optical limiters. Furthermore the index of refraction of such composites reaches very high values around the surface plasmon band. The nanoparticles in the glass give rise not only to an important index contrast between composite medium and bulk glass, but also a high dispersion over the whole visible range. The high index of refraction also opens possibilities outside integrated optics, in applications like reflection gratings where absorption inside the material plays a minor role. It might also be interesting for the design of photonic bandgap materials.

1.5 What you will find in this thesis

This thesis describes both work on the optical properties of erbium-doped waveguides codoped with different ions, and of ion-exchanged waveguides containing silver nanocrystals.

Chapters 2 and 3 explore the interactions between Er^{3+} and Eu^{3+} or Ce^{3+} , respectively, in Y_2O_3 . Both ions can accept the energy difference between the second and first excited states of Er^{3+} , yet with different energy transfer efficiencies. The increase of the transition rate between the two excited states of Er^{3+} is explained by a rate equation model, and the energy transfer rate constants are determined and compared.

In chapter 4 we turn to the interaction between Er^{3+} and Yb^{3+} in Al_2O_3 . Important parameters like absorption and emission cross sections are derived from waveguide transmission, and the energy transfer coefficient is determined from photoluminescence measurements. The data thus obtained are then used in chapter 5 as input into a rate equation propagation model to investigate the influence of Yb^{3+} concentration on the performance of an Er^{3+} doped waveguide amplifier. The results show that careful optimisation of the Yb^{3+} concentration is necessary with respect to other waveguide parameters such as length and available pump power.

Chapter 6 is dedicated to the interaction of Er^{3+} with Ag^+ ions in ion-exchanged waveguides on glass. Ag^+ ion or atom pairs act as sensitisers for Er^{3+} emission at 1540 nm when excitation takes place in the visible and ultraviolet regions of the spectrum.

Turning to the second topic of this thesis, chapter 7 describes the fabrication of glass waveguides doped with silver nanocrystals by a combination of ion exchange and ion irradiation. Waveguides containing up to 1% silver nanocrystals can be obtained in this way. Nanocrystal formation has been identified to depend on the energy deposited in atomic displacement collisions during the irradiation.

In chapter 8 we investigate the optical properties of waveguides doped with silver nanocrystals. The optical constants of the composite are determined on a planar

waveguide. Channel waveguides containing silver nanocrystal doped regions of different lengths were fabricated. Their transmission can be explained by the absorption of the silver nanocrystals. These waveguides act as low pass filters whose cut-off wavelength shifts towards longer wavelengths with increasing length of the region containing silver nanocrystals.

Finally, in chapter 9 we make use of the elevated index of refraction of a glass/silver nanocrystal composite to write a diffraction grating in ion-exchanged glass. This is achieved by ion implantation through a hexagonal array of self-organised colloidal silica particles deposited on the surface of the glass.

Part I

Codoping erbium doped waveguides

Chapter TWO

Selective modification of the Er^{3+} ${}^4\text{I}_{11/2}$ branching ratio by energy transfer to Eu^{3+}

WE PRESENT AN INVESTIGATION OF Er^{3+} PHOTOLUMINESCENCE IN Y_2O_3 WAVEGUIDES CODOPED WITH Eu^{3+} . AS A FUNCTION OF EUROPIUM CONCENTRATION WE OBSERVE AN INCREASE IN DECAY RATE OF THE ERBIUM ${}^4\text{I}_{11/2}$ ENERGY LEVEL AND AN INCREASE OF THE RATIO OF PHOTOLUMINESCENCE EMISSION FROM THE ${}^4\text{I}_{13/2}$ AND ${}^4\text{I}_{11/2}$ STATES. USING A RATE EQUATION MODEL, WE SHOW THAT THIS IS DUE TO AN ENERGY TRANSFER FROM THE ${}^4\text{I}_{11/2} \rightarrow {}^4\text{I}_{13/2}$ TRANSITION IN ERBIUM TO EUROPIUM. THIS INCREASES THE BRANCHING RATIO OF THE ${}^4\text{I}_{11/2}$ STATE TOWARDS THE ${}^4\text{I}_{13/2}$ STATE AND RESULTS IN A HIGHER STEADY STATE POPULATION OF THE FIRST EXCITED STATE OF ERBIUM. ABSOLUTE INTENSITY ENHANCEMENT OF THE ${}^4\text{I}_{13/2}$ EMISSION IS OBTAINED FOR EUROPIUM CONCENTRATIONS BETWEEN 0.1 AT.% AND 0.3 AT.%. IN ADDITION, THE PHOTOLUMINESCENCE DUE TO UPCONVERSION PROCESSES ORIGINATING FROM THE ${}^4\text{I}_{11/2}$ STATE IS REDUCED. USING SUCH STATE-SELECTIVE ENERGY TRANSFER, THE EFFICIENCY OF ERBIUM DOPED WAVEGUIDE AMPLIFIERS CAN BE INCREASED.

Erbium-doped optical amplifiers operate at 1540 nm by stimulated emission from the ${}^4I_{13/2}$ state in Er^{3+} . The standard in telecommunications to populate this energy level is via the second excited state ${}^4I_{11/2}$ using 980 nm radiation (cf. figure 2.1). An important ingredient in this pumping scheme is the nonradiative transition between the ${}^4I_{11/2}$ and ${}^4I_{13/2}$ states. Its rate depends on the host material. Incidentally, the most promising materials for erbium doped waveguide amplifiers possess low phonon energies, and therefore small nonradiative transition rates. This is a severe problem, since it gives rise to a significant steady state population of the ${}^4I_{11/2}$ level. As a result, a considerable fraction of Er^{3+} is not available for stimulated emission from the ${}^4I_{13/2}$ state. Moreover, when the ${}^4I_{11/2}$ population is high, excited state absorption and cooperative upconversion processes lead to unwanted excitation of even higher lying energy levels. For these reasons it is desirable to increase the transition rate between the ${}^4I_{11/2}$ and ${}^4I_{13/2}$ energy levels without affecting the optimised properties of the ${}^4I_{13/2}$ state itself. This will make the excitation stored in the ${}^4I_{11/2}$ state available for amplification of 1540 nm radiation, and in the process will also significantly reduce the probability of cooperative upconversion and excited state absorption from the ${}^4I_{11/2}$ state.

One way to enhance the transition rate from the second to the first excited state is engineering the crystal field of the host matrix at the position of the erbium ions. A simpler and newer approach, while leaving the well-established properties of existing waveguide materials unchanged, consists of selectively stimulating the transition between second and first excited state of Er^{3+} by resonant energy transfer to a suitable codopant. Hereby the energy difference between the relevant states of the erbium ion is transferred to the codopant. Mainly Ce^{3+} has been investigated as codopant so far (Simondi-Teisseire et al., 1996; Obaton et al., 1998; Meng et al., 1999), while Eu^{3+} and Tb^{3+} have been suggested (Andronov et al., 1998).

In this chapter we describe codoping of $\text{Er}^{3+}:\text{Y}_2\text{O}_3$ with Eu^{3+} . Yttrium oxide has already proven its suitability for optical amplification in waveguides (van Weerden et al., 1997), thanks to its high refractive index which provides both a high erbium emission cross section and the possibility of integration on a small area. We investigate the energy transfer by studying the erbium photoluminescence intensities and decay rates as a function of europium concentration, and establish a model based on rate equations which reproduces the data. Finally we show that the green upconversion emission of erbium in a planar waveguide is significantly reduced upon codoping with Eu^{3+} .

2.1 Sample preparation and characterisation techniques

The samples used in this study were prepared by sputter deposition of Y_2O_3 on a $3\ \mu\text{m}$ thick thermally grown silicon oxide buffer layer (Hoekstra, 1994). Since Y_2O_3 has a higher index of refraction (1.7 at 1500 nm (Hoekstra, 1994)) than SiO_2 , this

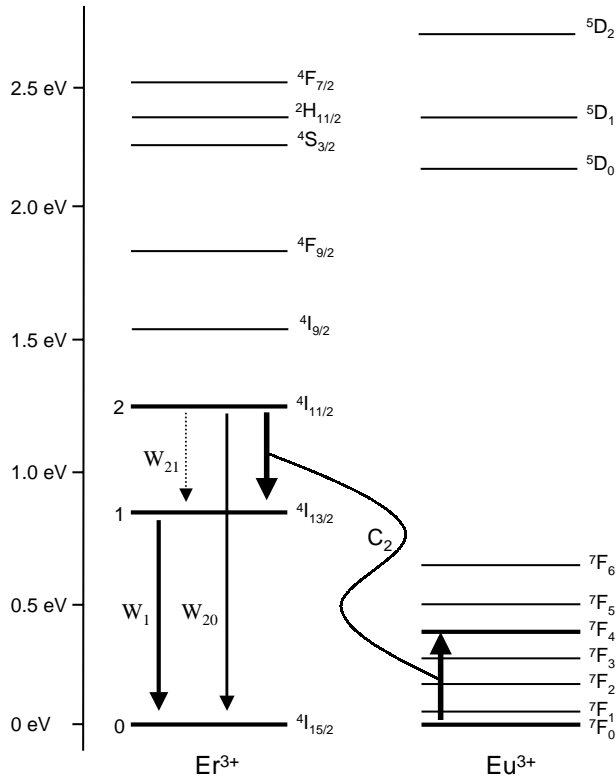


FIGURE 2.1: Energy level diagram of Er^{3+} and Eu^{3+} . Included are the relevant transitions for the rate equation model.

structure acts as a planar waveguide. The films are 800 nm thick as determined using Rutherford Backscattering Spectrometry (RBS). They were doped with erbium by ion implantation at a series of energies between 200 keV and 500 keV to obtain a flat concentration profile ranging from 30 nm to 100 nm below the surface. Subsequently, europium was implanted into the sample, creating a flat concentration profile that overlaps the erbium doped region completely. By implanting only part of the sample with europium we kept an on-wafer reference of only erbium doped Y_2O_3 . In this way variations in luminescent properties caused by slight differences of quality and treatment between samples can be taken into account. Exact concentrations were determined by RBS analysis and amount to 0.19 at.% erbium and to 0.024, 0.048, 0.12, 0.24, and 0.48 at.% europium. After implantation, the samples were heat treated at 700 °C for 30 min in a Rapid Thermal Annealer under oxygen flow.

For photoluminescence measurements we exploited the planar waveguide geometry of the samples. The 488 nm emission line of an Ar^+ laser was mechanically chopped

and then butt-coupled into the waveguide via an optical fibre. Photoluminescence emission was collected perpendicular to the waveguide by a multimode fibre with $600\ \mu\text{m}$ core diameter. The signal was dispersed in a 96 cm monochromator. The Er^{3+} emission around 1540 nm was analyzed with a germanium detector cooled to 77 K. For all emission lines with wavelengths shorter than 1100 nm, an AgOCs photomultiplier tube was used. The detector signal was fed through a lock-in amplifier. Photoluminescence decay traces of the Er^{3+} emission around 1540 nm were obtained using a digital oscilloscope, averaging typically 2500 single traces. The photoluminescence decay of the 980 nm emission of Er^{3+} , as well as of other emission lines at shorter wavelengths, was measured using a photon counting system and a multichannel scaler.

The 488 nm radiation leaving the planar waveguide at the output end served to trigger lock-in amplifier, oscilloscope, and multichannel scaler. In that way variations of the chopping speed will not have an influence on the accuracy of the measurements.

To obtain a good measure for the intensity ratio of the emission originating from the ${}^4\text{I}_{13/2}$ and ${}^4\text{I}_{11/2}$ levels, spectra were taken of the corresponding lines around 1538 nm and 980 nm with the cooled germanium detector, taking care not to change the experimental settings. After correction for the detector response, the total intensity in each line was determined by integrating over the spectra.

In order for the analysis presented in this article to be correct, it is important to perform all measurements in a regime where no saturation of the emission signal due to high pump power takes place. Therefore the pump power dependence of the emission line intensity was monitored before each measurement, and the excitation power adjusted to a value within its region of linearity.

2.2 The rate equation model

Figure 2.1 shows the mechanism we investigated to accelerate the decay rate of the second excited state of Er^{3+} . The rates W_1 , W_{20} , and W_{21} are defined as transition rates of the excited states of Er^{3+} in Y_2O_3 when no codoping with europium has taken place: W_1 is the total decay rate from the ${}^4\text{I}_{13/2}$ level, and is the sum of a radiative rate W_{1r} and a nonradiative rate W_{1nr} . W_{21} is the transition rate between the ${}^4\text{I}_{11/2}$ and ${}^4\text{I}_{13/2}$ states. It consists as well of a nonradiative and a radiative part, this distinction is however unnecessary for the model. W_{20} is the transition rate from the ${}^4\text{I}_{11/2}$ state to the ground state and is taken to be purely radiative. The total decay rate of the ${}^4\text{I}_{11/2}$ state is given by $W_2 = W_{21} + W_{20}$, in the absence of Eu^{3+} . The coupling of the ${}^4\text{I}_{11/2} \rightarrow {}^4\text{I}_{13/2}$ transition with the Eu^{3+} ion is described by the rate constant C_2 . We assume that an excited Eu^{3+} ion relaxes nonradiatively and fast to its ground state via the ${}^7\text{F}_j$ energy level ladder. This is a reasonable conjecture since the energy level spacings of the ${}^7\text{F}_j$ multiplet of Eu^{3+} in Y_2O_3 (Chang and Gruber, 1964) can be bridged by two phonons or less of the Y_2O_3 host (highest phonon density of states at $400\ \text{cm}^{-1}$ (Yamada et al., 1972)).

This idealised model is complicated by undesirable interactions, which are not de-

pictured in figure 2.1. Important are interactions especially of the $^4\text{I}_{13/2}$ state of Er^{3+} with Eu^{3+} (e.g. phonon-assisted energy transfer) or with defects originating from the europium implantation. These constitute additional decay channels for the $^4\text{I}_{13/2}$ state. We take this into account by an interaction rate S_1 , which may depend on europium concentration. The rate equations for the population of the excited erbium levels thus have the following form:

$$\begin{aligned}
 \frac{dN_2}{dt} &= R_2 - W_2N_2 - C_2N_qN_2 \\
 \frac{dN_1}{dt} &= R_1 - W_1N_1 + W_{21}N_2 + C_2N_qN_2 - S_1N_1
 \end{aligned} \tag{2.1}$$

The symbols R_1 , R_2 signify the excitation rate per unit volume into the first and second excited states of Er^{3+} respectively. Here we take into account that in the experiments Er^{3+} is initially excited into the $^4\text{F}_{7/2}$ state, from which the two lowest levels are fed according to some branching ratio. It is assumed that no excitation-induced saturation of Er^{3+} occurs, and that the population of the Er^{3+} energy levels is small enough to neglect nonlinear processes such as cooperative upconversion. N_q represents the concentration of Eu^{3+} . We assume that only an insignificant part of the Eu^{3+} is excited at any time.

The fraction of the population of the $^4\text{I}_{11/2}$ state that is de-excited via energy transfer to Eu^{3+} , so to speak the branching ratio of the energy transfer, is determined by the ratio of the energy transfer rate and the total decay rate of the $\text{Er}^{3+} \ ^4\text{I}_{11/2}$ state at a given Eu^{3+} concentration:

$$Q_2 = \frac{C_2N_q}{W_2 + C_2N_q} \tag{2.2}$$

Similarly, we can write the fraction of the population of the $^4\text{I}_{13/2}$ level that is quenched by the presence of Eu^{3+} or defects caused by the europium implantation as:

$$Q_1 = \frac{S_1}{W_1 + S_1} \tag{2.3}$$

The branching ratios Q_1 and Q_2 are experimentally accessible via decay rate measurements, as will be shown in the next section. They do not depend on erbium concentration. We would like to draw attention to the differences in definition between Q_1 and Q_2 . The interaction that quenches the first excited state of erbium (S_1) may depend on N_q in an unspecified way, while we assume a dependence of Q_2 on N_q as given by an energy transfer towards europium. In this way we include the possibility that the reduction in luminescence efficiency of the first excited state is caused by defects from the europium implantation, which are not annealed out during the heat treatment. On the other hand the model stays sufficiently precise with respect to the energy transfer from the $\text{Er}^{3+} \ ^4\text{I}_{11/2}$ level to Eu^{3+} to be tested by experiment.

The ratio of the emission intensities from the $^4\text{I}_{13/2}$ and $^4\text{I}_{11/2}$ levels can serve as an independent way to test the model. Substituting Q_1 and Q_2 into the rate

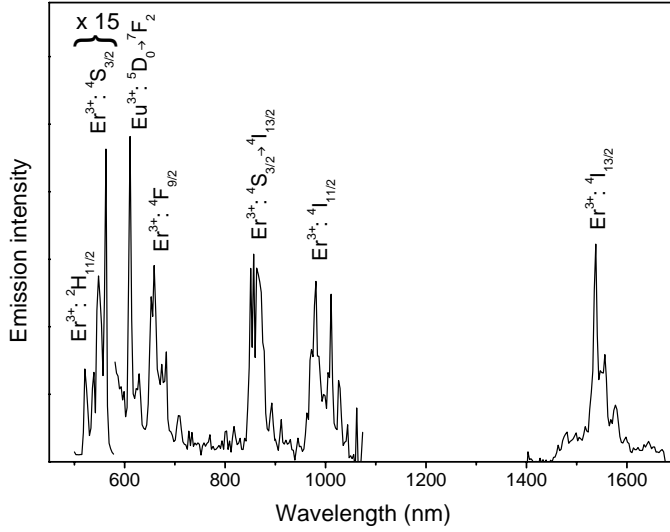


FIGURE 2.2: Typical emission spectrum of an Er^{3+} and Eu^{3+} doped Y_2O_3 waveguide, excited at 488 nm. Where no final state for a transition is given, the excitation relaxes directly to the ground state of the relevant ion.

equations (2.1) at steady state, and writing the intensities as $I_1 = W_{1r} \cdot h\nu_1 \cdot N_1$ and $I_2 = W_{20} \cdot h\nu_2 \cdot N_2$ for the emission from the first and second excited states of Er^{3+} respectively, the intensity ratio is given by the expression

$$\frac{I_1}{I_2} = \frac{1 - Q_1}{1 - Q_2} \frac{I_1^0}{I_2^0} + \frac{W_{1r}}{W_1} \frac{Q_2(1 - Q_1)}{1 - Q_2} \frac{\nu_1}{\nu_2} \quad (2.4)$$

I_1 and I_2 are the emission intensities from the first and second excited states of erbium respectively in the presence of europium, ν_1 and ν_2 the corresponding emission frequencies, and I_1^0/I_2^0 the intensity ratio of the two emission lines in the limit of zero Eu^{3+} concentration. The first term on the right of equation (2.4) describes the change in intensity ratio due to the depopulation of the two levels, while the second term takes into account the feeding of the first excited state from the second via energy transfer to Eu^{3+} .

Along the same line of reasoning, an absolute increase in emission intensity I_1 is achieved when

$$Q_2 > \frac{Q_1}{1 - Q_1} \frac{I_1^0}{I_2^0} \frac{W_1}{W_{1r}} \frac{\nu_2}{\nu_1} \quad (2.5)$$

Let us stress that in the ideal case of $S_1 = 0$ ($Q_1 = 0$) the analysis presented here is greatly simplified. The quenching of the first excited state is very likely linked to the ion implantation, and can be reduced to zero using other doping methods (compare e.g. Meng et al., 1999).

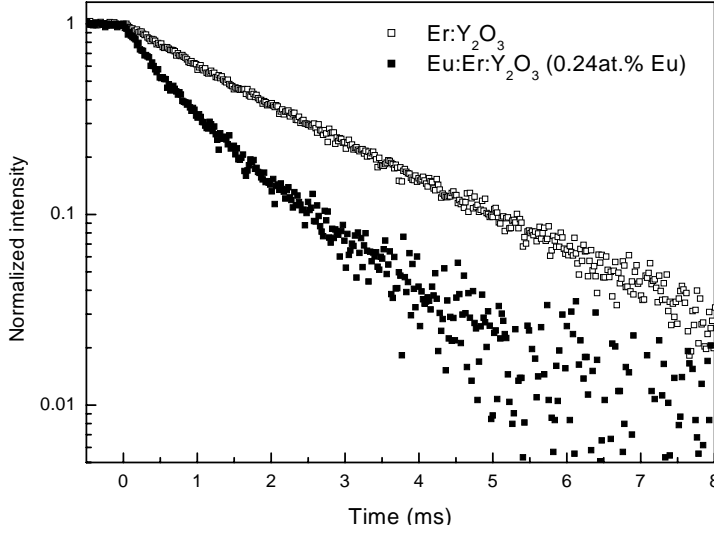


FIGURE 2.3: Photoluminescence decay of the $\text{Er}^{3+} \ ^4\text{I}_{11/2}$ state in Y_2O_3 monitored at 981 nm. The erbium concentration is 0.19 at.%. Decay traces are shown for a sample containing no europium and a sample containing 0.24 at.% europium.

2.3 Experimental results

Figure 2.2 shows the emission spectrum of the sample doped with 0.19 at.% erbium and 0.44 at.% europium in the visible and near infrared region, when excited at 488 nm. Emission lines of both Er^{3+} and Eu^{3+} can be identified, confirming the triply charged state of the ions in the matrix. The weaker emission of Eu^{3+} as compared to Er^{3+} is due to the small excitation cross section of Eu^{3+} at 488 nm. Figure 2.3 compares decay traces at 981 nm originating from the $\text{Er}^{3+} \ ^4\text{I}_{11/2}$ level in Y_2O_3 with and without addition of 0.24 at.% europium. The decay is single-exponential in the sample without europium, with a decay rate of 471 s^{-1} . Upon addition of europium, the decay becomes faster, the decay rate increases to 947 s^{-1} , and the decay becomes nonsingle exponential. By evaluating decay rates from curves taken at 981 nm and 1538 nm, we obtain experimental values for the fraction of the population de-excited via a channel induced by the europium:

$$Q_i^{N_q} = 1 - \frac{W_i^0}{W_i^{N_q}} \quad (2.6)$$

The index i labels the emission wavelength, the superscripts 0 and N_q refer to the europium concentration.

$Q_{1538}^{N_q}$ can be identified directly with Q_1 as given in the previous section, since the definition of the latter does not explicitly state a dependence on N_q . Conversely, if

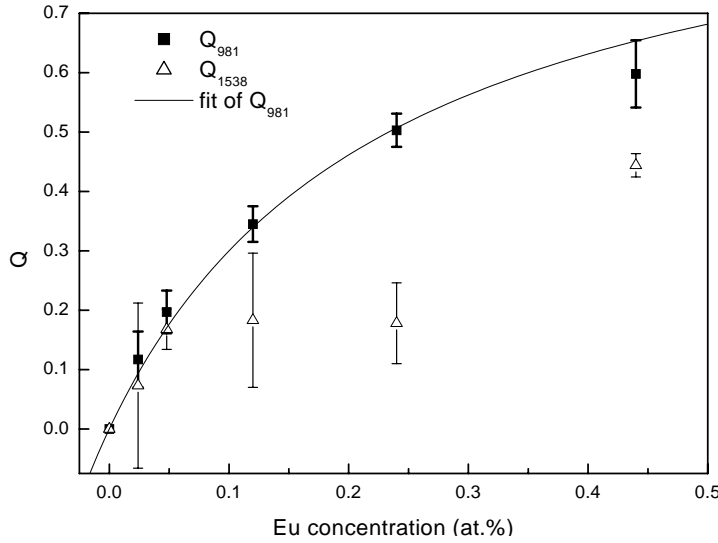


FIGURE 2.4: Branching ratio of the $\text{Er}^{3+} ({}^4I_{11/2} \rightarrow {}^4I_{13/2})$ to Eu^{3+} energy transfer (Q_{981}) and the fraction of energy lost from the $\text{Er}^{3+}: {}^4I_{13/2}$ state due to europium implantation (Q_{1538}). The line is a fit of Q_{981} to equation (2.2).

$Q_{981}^{N_q}$ exhibits the functional form of Q_2 , this is a clear indication that energy transfer towards Eu^{3+} really takes place.

In figure 2.4 we show the values for $Q_{1538}^{N_q}$ and $Q_{981}^{N_q}$ as a function of europium concentration. $Q_{981}^{N_q}$ increases monotonically and seems to saturate for high europium concentrations. $Q_{1538}^{N_q}$, however, increases for low europium concentrations, and saturates for intermediate europium concentrations. At $N_q = 0.44$ at.% we see another increase. Included in figure 2.4 is a fit of equation (2.2) to the data of $Q_{981}^{N_q}$, with C_2 as the single free parameter. The data is reproduced well for an energy transfer coefficient C_2 of $2.9 \cdot 10^{-18} \text{ cm}^3/\text{s}$. This value is nearly an order of magnitude higher than the cooperative upconversion coefficient from the first excited state of Er^{3+} in Y_2O_3 (Radius, 1994), indicating that the energy transfer towards europium is indeed efficient.

The data for $Q_{1538}^{N_q}$, on the other hand, cannot even be partially fitted to an equation of the form of equation (2.2), justifying the open definition of Q_1 . With these data we can exclude that the increase in decay rate of the ${}^4I_{13/2}$ level is caused by energy transfer to Eu^{3+} . Both resonant and phonon assisted energy transfer have the same dependency on N_q , and should therefore be reproduced by a function of the form of equation (2.2). This stands in clear contrast to our observations. Rather, we attribute the increase of the ${}^4I_{13/2}$ decay rate to quenching via implantation induced defects.

It is clear from figure 2.4 that through the right choice of europium concentration,

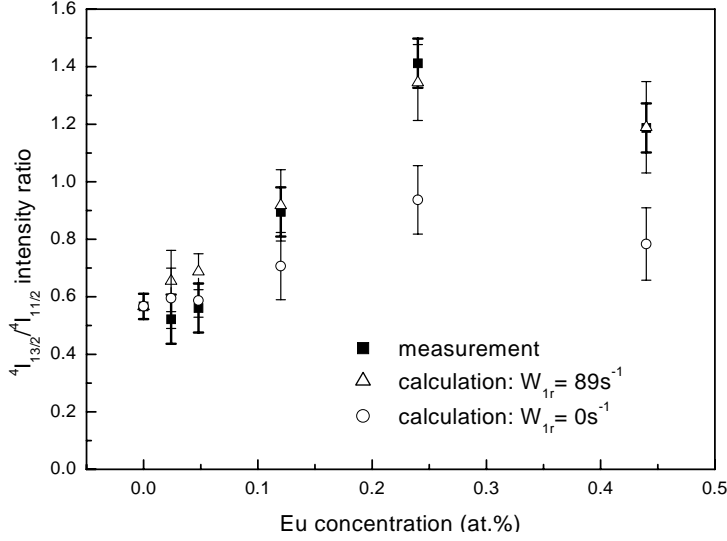


FIGURE 2.5: Ratio of emission intensity from the Er^{3+} ${}^4\text{I}_{13/2}$ and ${}^4\text{I}_{11/2}$ energy levels. Included are calculations according to equation (2.4) with $W_{1r} = 89\text{ s}^{-1}$ and $W_{1r} = 0\text{ s}^{-1}$.

a substantial increase of the transition rate from the second to the first excited state of erbium can be induced at a low cost in lifetime of the first excited state itself.

For completeness let us state that we have also measured the change in decay rate of erbium energy levels in the visible region. A significant increase is observed only for the sample containing 0.44 at.% europium. In this case, the ${}^2\text{H}_{11/2}$ and ${}^4\text{S}_{3/2}$ levels are the only ones affected, with Q_{563} and Q_{521} amounting to 0.2 ± 0.1 . This may be due to nonresonant energy transfer to the ${}^5\text{D}_{0,1}$ levels of Eu^{3+} (cf. figure 2.1).

The validity of the model can be independently checked by measuring the intensity ratio of the emission originating from the ${}^4\text{I}_{13/2}$ and ${}^4\text{I}_{11/2}$ levels. Figure 2.5 shows these measurements as a function of europium concentration. The intensity ratio increases from 0.57 without europium to 1.41 at 0.24 at.% europium. A slightly lower value is observed at 0.44 at.% europium. Included in the figure are data calculated according to equation (2.4), with the data of figure 2.4 as input. The measurement is once again reproduced well by the calculation. The only free parameter here is the radiative decay rate of the first excited state, W_{1r} , which has been adjusted to 89 s^{-1} for the best fit. As a comparison, the total decay rate W_1 was measured to be 115.7 s^{-1} .

To illustrate the effect of the increased branching ratio from the ${}^4\text{I}_{11/2}$ to the ${}^4\text{I}_{13/2}$ state, we have also plotted the calculated values for $W_{1r} = 0$. It is clear that for high europium concentrations the second term on the right-hand side of equation (2.4) contributes significantly to the intensity ratio. As stated earlier, this term repre-

sents the contribution caused by the additional feeding of the ${}^4I_{13/2}$ level via the interaction between the ${}^4I_{11/2}$ level and Eu^{3+} . It is only this term that contains the adjustable parameter W_{1r} . In case all europium-induced de-excitation of the ${}^4I_{11/2}$ state were towards the ground state, this term would be zero (this is equivalent to setting $W_{1r} = 0$). The values of the first term of equation (2.4), however, lie significantly lower than the measurement points, especially at high europium concentrations, as shown in figure 2.5. Accordance can only be achieved by postulating the model detailed in the previous section. From the intensity ratios we can therefore exclude direct de-excitation of the ${}^4I_{11/2}$ level to the ground state via e.g. defects.¹

From the experimental data it follows that inequality (2.5) is fulfilled for Eu^{3+} concentrations between 0.1 at.% and 0.3 at.%. Assuming that the rate equation model fully describes the physics in our samples, this means that in spite of the higher decay rate of the ${}^4I_{13/2}$ state, in this region absolute intensity enhancement is achieved. For the sample with the highest Eu^{3+} concentration, this is not any more the case, since the increase of the decay rate of the ${}^4I_{13/2}$ state is too high. This problem might be overcome by using a doping method other than ion implantation, which does not affect the decay rate of the ${}^4I_{13/2}$ state.

Two of the great loss mechanisms of excitation in integrated optical amplifiers are cooperative upconversion and excited state absorption. These two processes are enhanced by population build-up in an excited state. Increasing the decay rate of the second excited state of erbium should therefore decrease the green emission due to upconversion processes originating from this state. Figure 2.6 compares optical images of planar waveguides doped with 0.19 at.% erbium, one of them codoped with 0.44 at.% europium. Excitation takes place by coupling 979 nm radiation into the waveguide from a fibre (left side of the images). The excitation power was adjusted such that the emission at 1538 nm, a measure for the population of the ${}^4I_{13/2}$ level, had the same intensity for both measurements. The green emission due to upconversion is clearly reduced on codoping with europium.

The reduction of upconversion emission due to codoping with Eu^{3+} can also find application in erbium-doped amplifiers pumped directly into the ${}^4I_{13/2}$ level, e.g. with 1480 nm light. In highly doped amplifiers, cooperative upconversion and excited state absorption from the ${}^4I_{13/2}$ state lead to a significant population of the ${}^4I_{11/2}$ level. The same mechanisms of gain reduction as described for 980 nm pumping come into effect, on a somewhat lesser scale. Even in such a system it is therefore desirable to increase the transition rate between the ${}^4I_{11/2}$ and ${}^4I_{13/2}$ states.

¹Actually the argument has to be extended slightly. Assuming an additional de-excitation channel proportional to N_q , leading from the ${}^4I_{11/2}$ level to the ground state, will change the dependencies on europium concentration of neither Q_2 nor the intensity ratio. The parameter arrived at in figure 2.5 then constitutes a lower limit for W_{1r} rather than W_{1r} itself. On the other hand, the measured lifetime of the ${}^4I_{13/2}$ state extrapolated to zero erbium concentration (96 s^{-1} (Hoekstra, 1994)) provides an upper limit for W_{1r} . Since the radiative decay rate has not been determined independently, we have to conclude by pointing out that the limits to W_{1r} do not allow for enough variation to jeopardise the statements made in the main text.

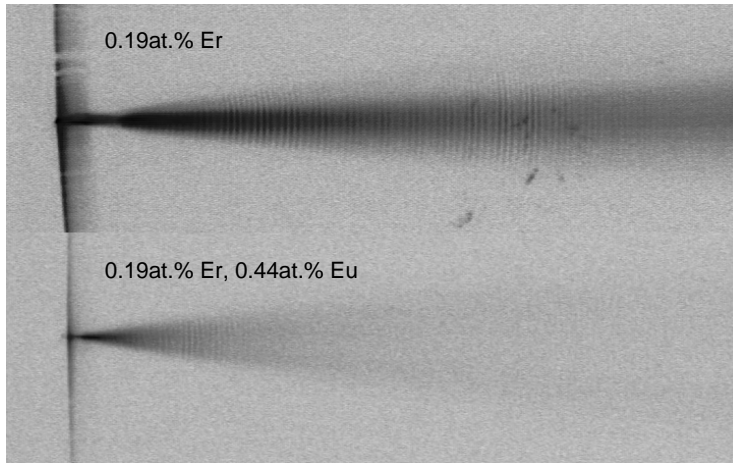


FIGURE 2.6: False colour image of the green emission of Er^{3+} with and without europium. The green emission from the $\text{Er}^{3+} \ ^4\text{S}_{3/2}$ state is represented in black. 980 nm light is coupled into the planar waveguide from a fibre (left hand side of the images). In the presence of 0.44 at.% europium, the green upconversion emission is reduced considerably.

2.4 Summary

The population in the first excited state of Er^{3+} in a Y_2O_3 matrix, under excitation at 980 nm can be increased by codoping with Eu^{3+} . This is due to a controlled resonant energy transfer from the second excited state of Er^{3+} towards Eu^{3+} , reducing the population in that state in favour of the population in the first excited state. This process of selective increase of the decay rate of a certain energy level with control over the transition's final state is especially useful for materials with low phonon energies.

We have been able to show that energy transfer between Er^{3+} and Eu^{3+} is responsible for the acceleration of the decay of the erbium's second excited state in Y_2O_3 doped by ion implantation. The energy transfer coefficient from Er^{3+} to Eu^{3+} was determined as $2.9 \cdot 10^{-18} \text{ cm}^3/\text{s}$. This means that by codoping with 0.44 at.% europium we have achieved a 60% efficiency of the energy transfer in depopulating the second excited state. This is reflected in the emission intensities: the emission from the first excited state is significantly increased for europium concentrations above 0.1 at.%. The reduced population of the second excited state leads further to a decrease in green upconversion photoluminescence under 980 nm excitation. In this way an important loss channel in highly pumped optical amplifiers can be effectively closed.

Chapter THREE

Enhancement of Er^{3+} ${}^4\text{I}_{13/2}$ population by energy transfer to Ce^{3+}

WE REPORT MEASUREMENTS OF THE ENERGY TRANSFER BETWEEN Er^{3+} AND Ce^{3+} IN Y_2O_3 . THE TRANSITION BETWEEN THE Er^{3+} ${}^4\text{I}_{11/2}$ AND ${}^4\text{I}_{13/2}$ EXCITED STATES CAN BE STIMULATED BY ENERGY TRANSFER TO Ce^{3+} , AUGMENTING THE POPULATION IN THE ${}^4\text{I}_{13/2}$ STATE AT THE EXPENSE OF THAT IN THE ${}^4\text{I}_{11/2}$ STATE. EXPERIMENTS WERE PERFORMED ON Y_2O_3 PLANAR WAVEGUIDES DOPED WITH 0.2 AT.% ERBIUM AND 0 – 0.42 AT.% CERIUM BY ION IMPLANTATION. FROM MEASUREMENTS OF Er^{3+} DECAY RATES AS A FUNCTION OF CERIUM CONCENTRATION WE DERIVE AN ENERGY TRANSFER RATE CONSTANT OF $1.3 \cdot 10^{-18} \text{ cm}^3/\text{s}$. THE EFFICIENCY OF THE ENERGY TRANSFER AMOUNTS TO 0.47 AT 0.42 AT.% CERIUM. THE ENERGY TRANSFER RATE CONSTANT MEASURED IN Y_2O_3 IS TWO TIMES SMALLER FOR $\text{Er}^{3+} \longrightarrow \text{Ce}^{3+}$ THAN THAT FOR $\text{Er}^{3+} \longrightarrow \text{Eu}^{3+}$ IN THE SAME MATERIAL.

Optical amplifiers in telecommunications networks make use of population inversion between the first excited (${}^4I_{13/2}$) and ground (${}^4I_{15/2}$) states of Er^{3+} to achieve amplification around 1540 nm (cf. figure 3.1). Population inversion is obtained by exciting the second excited state ${}^4I_{11/2}$ with 980 nm radiation, from where the ion relaxes to the ${}^4I_{13/2}$ level by interactions with matrix vibrations. To attain high population of the ${}^4I_{13/2}$ state, this nonradiative de-excitation route has to be efficient compared to the radiative transitions from the ${}^4I_{11/2}$ and ${}^4I_{13/2}$ levels to the ground state.

In many promising amplifier and laser materials this is not the case. Their phonon energies are low, therefore multiple phonons are required to bridge the energy gap between the ${}^4I_{11/2}$ and ${}^4I_{13/2}$ levels, making the de-excitation inefficient. This means that when Er^{3+} is excited with 980 nm radiation, a considerable amount of energy is stored in the second excited state, and is not available for stimulated emission from the ${}^4I_{13/2}$ level. The efficiency of the transition from the ${}^4I_{11/2}$ to the ${}^4I_{13/2}$ state can be improved by transferring the energy difference between the two levels to a suitable acceptor ion. This process has been shown for Ce^{3+} (Simondi-Teisseire et al., 1996; Obaton et al., 1998; Meng et al., 1999, 2000; Choi et al., 2000b) and Eu^{3+} (Andronov et al., 1998; Strohhöfer et al., 2000, see chapter 2) in glasses and crystalline materials. It is not known, however, which of these ions acts as the most efficient acceptor in a given material.

In this article we describe codoping of $\text{Er}^{3+}:\text{Y}_2\text{O}_3$ with cerium. The choice of the host was suggested by its established properties as waveguide and amplifier material (Hoekstra, 1994; van Weerden et al., 1997). We are able to show that codoping with Ce^{3+} indeed increases the decay rate of the second excited state of Er^{3+} and the population in its first excited state. Comparing our present results to our data on the energy transfer between Er^{3+} and Eu^{3+} in Y_2O_3 (chapter 2), we show that the energy transfer efficiency between Er^{3+} and Ce^{3+} is lower by a factor of two.

3.1 Sample preparation and characterisation techniques

Yttrium oxide planar waveguides were fabricated by sputter deposition on thermally oxidised silicon wafers (Hoekstra, 1994). The SiO_2 and Y_2O_3 layer thicknesses are $3\ \mu\text{m}$ and $750\ \text{nm}$, respectively, as determined with Rutherford Backscattering Spectrometry (RBS). To dope the Y_2O_3 with the rare earth ions we have used ion implantation, as it is known to lead to well controlled doping profiles and a homogeneous distribution of the implanted ions. The samples were implanted with erbium at energies between 200 keV and 500 keV to a total fluence of $1.34 \cdot 10^{15}\ \text{cm}^{-2}$ to create a flat dopant profile at a concentration of $1.38 \cdot 10^{20}\ \text{cm}^{-3}$ (0.21 at.%) over the depth from 30 nm to 130 nm from the surface. Cerium was then co-implanted into parts of the samples at energies between 185 keV and 425 keV. These energies were chosen such as to match the cerium and erbium dopant profiles. Total implantation fluences were $2.7 \cdot 10^{14}$, $6.9 \cdot 10^{14}$, $1.73 \cdot 10^{15}$, and $2.68 \cdot 10^{15}\ \text{cm}^{-2}$. The cerium concentra-

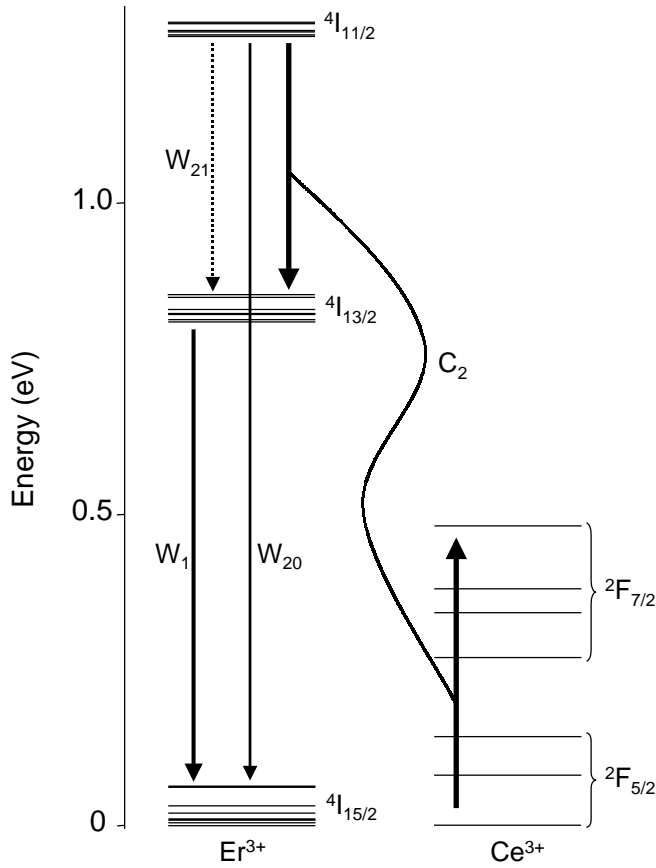


FIGURE 3.1: Energy levels of Er^{3+} and Ce^{3+} . The arrows indicate the relevant transitions for the rate equation model.

tions were obtained by RBS and amount to 0.05, 0.07, 0.25, and 0.42 at.%. The sample temperature was kept at 77 K during all implantations. After ion implantation, the samples were annealed at 700 °C for one hour in a vacuum furnace at a base pressure below 10^{-4} Pa. The part of the samples not implanted with cerium serves as an on-wafer reference for the analysis. In this way slight differences in luminescent properties between the samples can be taken into account.

Room temperature photoluminescence from Er^{3+} was measured by exploiting the planar waveguide geometry of the samples. Light from an Ar^+ ion laser operating at 488 nm was mechanically chopped and butt-coupled into the waveguides using an optical fibre. The photoluminescence emission from the different energy levels of Er^{3+} was collected perpendicular to the waveguide plane with an optical fibre of core

diameter 0.6 mm. The light was dispersed in a 96 cm monochromator and detected with an AgOCs photomultiplier tube in the wavelength region between 500 nm and 1100 nm, and a germanium detector cooled to 77 K in the region around 1500 nm.

Photoluminescence decay traces of the $\text{Er}^{3+} \ ^4\text{I}_{13/2}$ energy level at 1538 nm were recorded on a digital oscilloscope, averaging typically 2500 single traces for each measurement. The decay traces of the $\ ^4\text{I}_{11/2}$ level at 980 nm as well as of the higher lying energy levels were measured using a photon counting system and a multichannel scaler. The decay traces were fitted by single exponential functions to obtain the decay rates. Only the decay of the $\ ^4\text{I}_{11/2}$ level in the sample with the highest cerium concentration was not single exponential. In this case the first e-folding time has been used to define the decay rate.

Values for the ratio of intensities emitted from the $\ ^4\text{I}_{13/2}$ and $\ ^4\text{I}_{11/2}$ states were obtained by measuring photoluminescence spectra of the corresponding emission lines under identical experimental conditions, using the Ge detector. The spectral resolution was set to 3 nm, the Er^{3+} was excited with 488 nm radiation. Standard lock-in techniques were employed to reduce the noise level. The spectra were corrected for the detector response and integrated in the frequency domain to obtain the emission intensity in each line.

To directly measure the changes of photoluminescence emission intensity from the $\text{Er}^{3+} \ ^4\text{I}_{13/2}$ state caused by codoping with Ce^{3+} , we used radiation from a continuous wave titanium-sapphire laser at 982.3 nm to excite the Er^{3+} into its $\ ^4\text{I}_{11/2}$ state. Excitation took place through the surface of the yttrium oxide under an angle of approximately 30° . The emission of the $\ ^4\text{I}_{15/2}$ level was imaged onto the entrance slit of the monochromator and detected with the germanium detector as described above. The integral of the photoluminescence spectra served as a measure for the emitted intensity.

For all the measurements reported in this article, care has been taken to keep the excitation power so low as to ensure a linear relationship between excitation and emission intensities. In this way power and population dependent effects, like cooperative upconversion and excited state absorption, can be excluded and do not have to be taken into account for the analysis.

3.2 Rate equation model

The rate equation model used to describe Er^{3+} , Ce^{3+} , and their interaction is identical to the one described in chapter 2 for europium codoping. We refer the interested reader to the relevant section 2.2 for details. Here we will be brief.

In figure 3.1 we show a schematic of the mechanism that accelerates the transition between the $\text{Er}^{3+} \ ^4\text{I}_{11/2}$ and $\ ^4\text{I}_{13/2}$ states. The transition rates W_1 , W_{20} , and W_{21} are defined as the intrinsic Er^{3+} rates in Y_2O_3 . W_1 is the decay rate of the $\ ^4\text{I}_{13/2}$ level. W_{21} and W_{20} are the rates of the transitions from the $\ ^4\text{I}_{11/2}$ level to the $\ ^4\text{I}_{13/2}$ and $\ ^4\text{I}_{15/2}$ states, respectively. We define W_{21} as the sum of the relevant radiative

and nonradiative transition rates, while we assume W_{20} to be purely radiative. The sum of W_{21} and W_{20} , W_2 , is the total decay rate of the $^4\text{I}_{11/2}$ level.

The coupling between the $\text{Er}^{3+} \ ^4\text{I}_{11/2} \rightarrow ^4\text{I}_{13/2}$ transition with Ce^{3+} is described by the rate constant C_2 . We will assume the population in the $^2\text{F}_{7/2}$ state of Ce^{3+} to be negligible at all times. This presumption is plausible at room temperature, considering that the Stark levels of both the $^2\text{F}_{7/2}$ and $^2\text{F}_{5/2}$ energy levels are split widely in Y_2O_3 (Chang et al., 1982) and all energy gaps can be bridged by two to three phonons of the Y_2O_3 host (highest phonon density of states at 400 cm^{-1} (Yamada et al., 1972)).

As shown in section 2.2, we can define the fraction of the population in the $^4\text{I}_{11/2}$ level that is de-excited via energy transfer to Ce^{3+} as

$$Q_2 = \frac{C_2 N_q}{W_2 + C_2 N_q} \quad (3.1)$$

The choice of this function, namely the linear dependence of the energy transfer rate $C_q N_q$ on cerium concentration, is justified by experiment (cf. section 3.3). Similarly we can write the fraction of population in the $^4\text{I}_{13/2}$ level that is de-excited due to the interaction S_1 as

$$Q_1 = \frac{S_1}{W_1 + S_1} \quad (3.2)$$

These branching ratios serve as a measure for the efficiency of the de-excitation processes undergone by the two energy levels and are determined by means of decay rate measurements.

The ratio between the emission intensities from the $^4\text{I}_{11/2}$ and $^4\text{I}_{13/2}$ states can be written as (cf. chapter 2)

$$\frac{I_1}{I_2} = \frac{1 - Q_1}{1 - Q_2} \frac{I_1^0}{I_2^0} + \frac{W_{1r}}{W_1} \frac{Q_2(1 - Q_1)}{1 - Q_2} \frac{\nu_1}{\nu_2} \quad (3.3)$$

The rate equations (2.1) are easily adapted to describe excitation of the $^4\text{I}_{11/2}$ state by radiation around 980 nm. The only change necessary is setting $R_1 = 0$. By exciting at 980 nm, we can estimate the effect of codoping directly by measuring the emission intensities from the $^4\text{I}_{13/2}$ state of Er^{3+} in the presence and absence of cerium. The ratio of these intensities is given by

$$\frac{I_1^q}{I_1^0} = (1 - Q_1)(1 - Q_2) + \frac{W_2}{W_{21}} (1 - Q_1) Q_2 \quad (3.4)$$

Here I_1^q and I_1^0 represent the emission intensities from the $^4\text{I}_{13/2}$ state in the presence of cerium at a concentration q and in the limit of zero cerium concentration, respectively.

3.3 Experimental results

Figure 3.1 shows the energy levels for Er^{3+} and Ce^{3+} in Y_2O_3 as reported by Chang et al. (1982). The Stark levels of the Ce^{3+} ${}^2\text{F}_{7/2}$ and ${}^2\text{F}_{5/2}$ states are split widely and therefore provide for efficient de-excitation of the upper levels via vibrational interactions with the Y_2O_3 lattice. The transition between the lowest energy Stark level of the ground state and the highest energy Stark level of the excited state is resonant with the transition between the ${}^4\text{I}_{11/2}$ and ${}^4\text{I}_{13/2}$ levels of Er^{3+} . This is the condition necessary for active transfer of population from the ${}^4\text{I}_{11/2}$ to the ${}^4\text{I}_{13/2}$ state of Er^{3+} and thus for an increased transition rate between these two levels.

The interaction between Er^{3+} and Ce^{3+} manifests itself by an increased decay rate of the Er^{3+} ${}^4\text{I}_{11/2}$ level. The difference between the ${}^4\text{I}_{11/2}$ decay rates for cerium concentrations N_q and zero can be interpreted as the energy transfer rate from the Er^{3+} ${}^4\text{I}_{11/2}$ state to cerium:

$$W_{tr}^{N_q} = W_{981}^{N_q} - W_{981}^0 \quad (3.5)$$

with W_{981}^{0,N_q} the measured decay rates at cerium concentrations of zero and N_q . As shown in the inset of figure 3.2, a double logarithmic plot of W_{tr} against N_q , the transfer rate depends linearly on cerium concentration. This result justifies the definition of equation (3.1) as the efficiency of de-excitation via Ce^{3+} .

The energy transfer efficiency between Er^{3+} and Ce^{3+} can be derived from experimental data as:

$$Q_{981}^{N_q} = 1 - \frac{W_{981}^0}{W_{981}^{N_q}} \quad (3.6)$$

and a similar definition can be given for the energy transfer efficiency from the Er^{3+} ${}^4\text{I}_{13/2}$ state, $Q_{1538}^{N_q}$.

The values obtained for both $Q_{981}^{N_q}$ and $Q_{1538}^{N_q}$ at different cerium concentrations are plotted in figure 3.2. Q_{981} rises monotonically over the full concentration range, reaching a value of 0.47 for 0.42 at.% cerium. This behaviour is expected when energy transfer from the Er^{3+} ${}^4\text{I}_{11/2}$ level to Ce^{3+} takes place. By fitting the data Q_{981} with the function given by equation (3.1), we determine the energy transfer coefficient C_2 to be $(1.3 \pm 0.1) \cdot 10^{-18} \text{ cm}^3/\text{s}$. Q_{1538} also increases with cerium concentration. The data cannot be described, however, by a function of the form of equation (3.1) and therefore by an energy transfer to cerium. Similar behaviour has been observed in previous work on the same system using Eu^{3+} as the codopant (Strohhöfer et al., 2000, see chapter 2). It is attributed to defects induced by the ion implantation that are not removed during the anneal of the samples.

The increase of the decay rate of the Er^{3+} ${}^4\text{I}_{11/2}$ state due to cerium codoping does of course also have an influence on the shape of the decay curves of the ${}^4\text{I}_{13/2}$ state. The ${}^4\text{I}_{13/2}$ state receives excitation from the ${}^4\text{I}_{11/2}$ state on the time scale of the ${}^4\text{I}_{11/2}$ decay rate W_{981} . This can be discerned in the ${}^4\text{I}_{13/2}$ decay at short

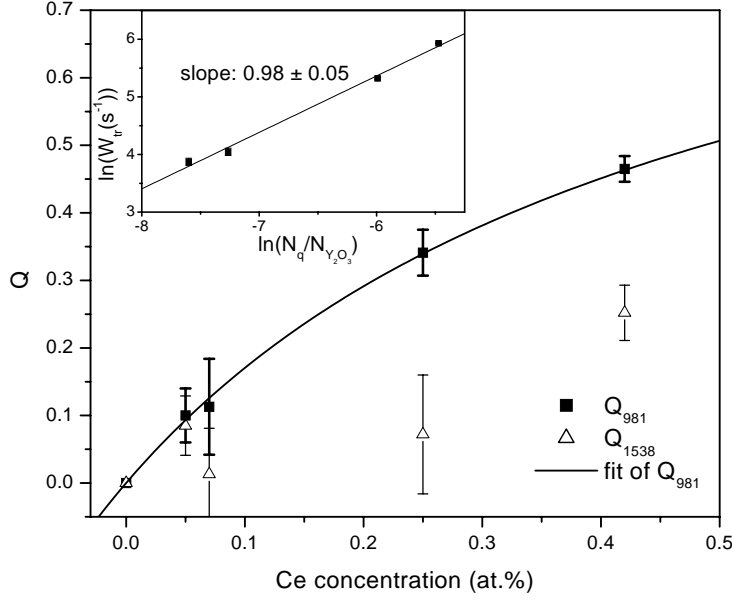


FIGURE 3.2: Efficiency of the $\text{Er}^{3+} ({}^4\text{I}_{11/2} \rightarrow {}^4\text{I}_{13/2})$ to Ce^{3+} energy transfer (Q_{981}) and the fraction of energy lost from the $\text{Er}^{3+} \ ^4\text{I}_{13/2}$ state due to cerium implantation (Q_{1538}). The line is a fit of equation (3.1) to the data for Q_{981} . The inset shows a double logarithmic plot of the transfer rate W_{tr} from the $\text{Er}^{3+} \ ^4\text{I}_{11/2}$ state to cerium versus cerium concentration. The linear dependence justifies the definition of $W_{tr} = C_2 N_q$ in equation (3.1).

times (Fick et al., 2000). Figure 3.3 compares the decay traces of samples doped with zero and 0.25 at.% cerium. While both curves approach the same decay rate at long times, initially there is a clear difference between them. When no codoping with cerium has taken place, the decay is clearly non-exponential at short times. It becomes more single exponential when cerium is introduced as codopant. Solving the rate equations (2.1), we obtain the decay function of the ${}^4\text{I}_{13/2}$ state as

$$N_1(t) = \left(N_1^0 + \frac{W_{21} N_2^0}{W_2 - W_1} \right) e^{-W_1 t} - \frac{W_{21} N_2^0}{W_2 - W_1} e^{-W_2 t} \quad (3.7)$$

where N_1^0 and N_2^0 represent the initial population of the ${}^4\text{I}_{13/2}$ and ${}^4\text{I}_{11/2}$ manifolds.

It is clear that all information on the decay rates of the ${}^4\text{I}_{11/2}$ state is contained in the decay traces of the ${}^4\text{I}_{13/2}$ state. Fitting equation (3.7) to the decay trace without cerium (for data and fit see figure 3.3), we obtain a value of $392 \pm 50 \text{ s}^{-1}$ for W_2 . It is in reasonable agreement with the one measured by direct observation of the decay of the ${}^4\text{I}_{11/2}$ level ($428 \pm 8 \text{ s}^{-1}$). The accuracy is however lower than for the direct measurement, and decreases even further when the decay rate W_2 increases.

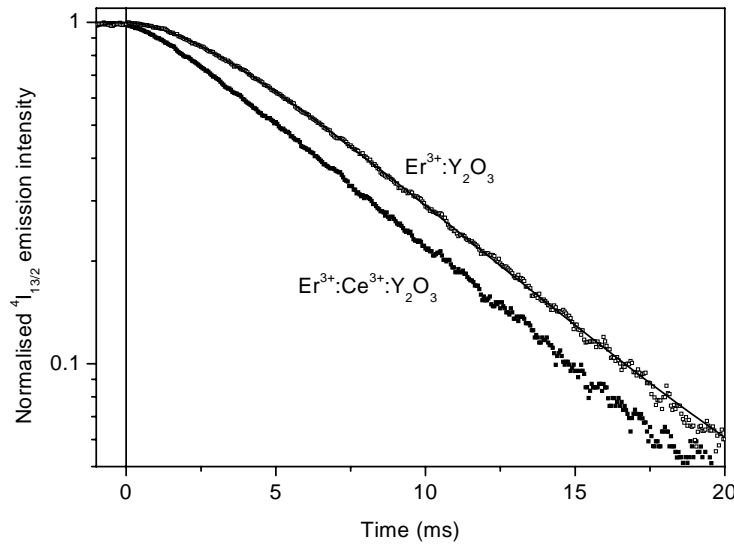


FIGURE 3.3: Decay of the ${}^4I_{13/2}$ emission at 1538 nm for a sample containing only erbium and a sample codoped with 0.25 at.% cerium, excited at 488 nm. The decay at short times is slower than at long times, reflecting the de-excitation of the ${}^4I_{11/2}$ to the ${}^4I_{13/2}$ manifold. The drawn line is a fit of equation (3.7) to the data. Note that the effect decreases with cerium codoping, an indication of the increase in decay rate of the ${}^4I_{11/2}$ state.

Evidence that the population from the ${}^4I_{11/2}$ state of Er^{3+} is indeed transferred to the ${}^4I_{13/2}$ state is provided by measurements of the ratio between the photoluminescence intensities emitted from these two levels. These are plotted in figure 3.4. As expected from considerations of the model outlined in figure 3.1, the data show an increase of the intensity ratio of the ${}^4I_{13/2}$ and ${}^4I_{11/2}$ levels with increasing cerium concentration. This indicates that the population in the first excited state of Er^{3+} is growing with respect to the population in its second excited state. Making use of the values for the Q_i 's obtained from decay rate measurements (cf. figure 3.2), we can calculate the expected behaviour of the ${}^4I_{13/2}/{}^4I_{11/2}$ intensity ratio according to equation (3.3). The only free parameter in the calculation is the radiative decay rate of the ${}^4I_{13/2}$ level. The minimal mean squared deviation between data and calculation is achieved for $W_{1r} = 89 \text{ s}^{-1}$. Note that correspondence between calculation and experiment cannot be obtained assuming direct de-excitation of the ${}^4I_{11/2}$ level to the ground state. In this case the intensity ratio is determined completely by the measured decay rates, without any adjustable parameters. Mathematically this is equivalent to setting $W_{1r} = 0$ in equation (3.3). The values of the intensity ratio under this condition are also shown in figure 3.4.

The observation of the increase in photoluminescence originating from the Er^{3+}

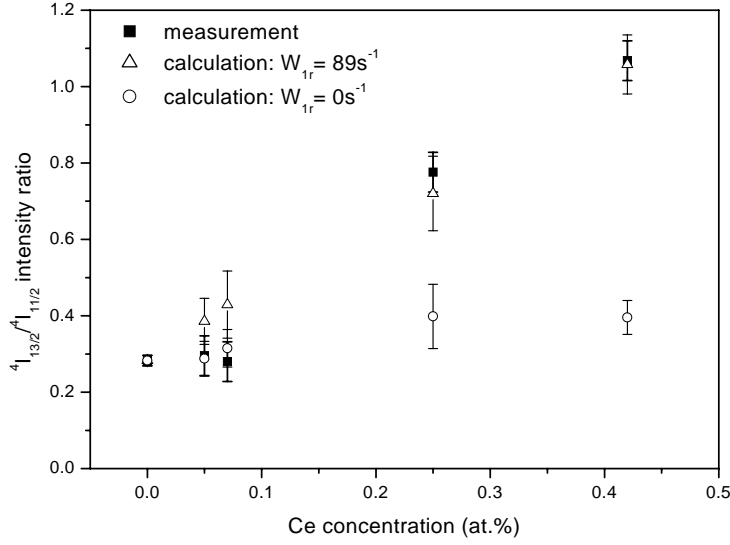


FIGURE 3.4: Ratio of emission intensity from the $\text{Er}^{3+} \ ^4\text{I}_{13/2}$ and $^4\text{I}_{11/2}$ energy levels. Overlaid is a calculation according to equation (3.3) with $W_{1r} = 89 \text{ s}^{-1}$, using the data from figure 3.2. Direct de-excitation of the $\text{Er}^{3+} \ ^4\text{I}_{11/2}$ state to the ground state ($W_{1r} = 0$) does not reproduce the data.

$^4\text{I}_{13/2}$ state under 980 nm excitation is the most direct manner to prove the transfer of population from the $^4\text{I}_{11/2}$ to the $^4\text{I}_{13/2}$ level, yet also the most difficult for our samples. From the measured decay rates ($W_2^0 = 428 \text{ s}^{-1}$ and $W_1^0 = 100 \text{ s}^{-1}$) we can estimate that the enhancement for $Q_2 = 1$ will be below 25 %, a value we do not achieve in the concentration range of cerium we have investigated. Slight variations in chopper speed in conjunction with the lock-in technique will provide errors of the order of 10 %. Therefore the data presented in figure 3.5 should be viewed as qualitative rather than providing exact results. Plotted in the figure is the intensity emitted by the $^4\text{I}_{13/2}$ state of Er^{3+} in samples codoped with different cerium concentrations, normalised by the intensity emitted from their respective undoped reference samples. This measured ratio increases up to a cerium concentration of 0.25 at.%. It is reduced for the sample doped with 0.42 at.% cerium due to the increased value of Q_1 . A calculation according to equation (3.4), using the data from figure 3.2, is overlaid over the data. Although the error bars of both measurement and calculation are large, we are able to determine bounds for the free parameter in this calculation, W_2/W_{21} . This is the inverse of the branching ratio of the $^4\text{I}_{11/2}$ level to the $^4\text{I}_{13/2}$ level in the absence of cerium, and lies in the range $1.4 \lesssim W_2/W_{21} \lesssim 1.75$. This corresponds to a branching ratio between 0.57 and 0.71.

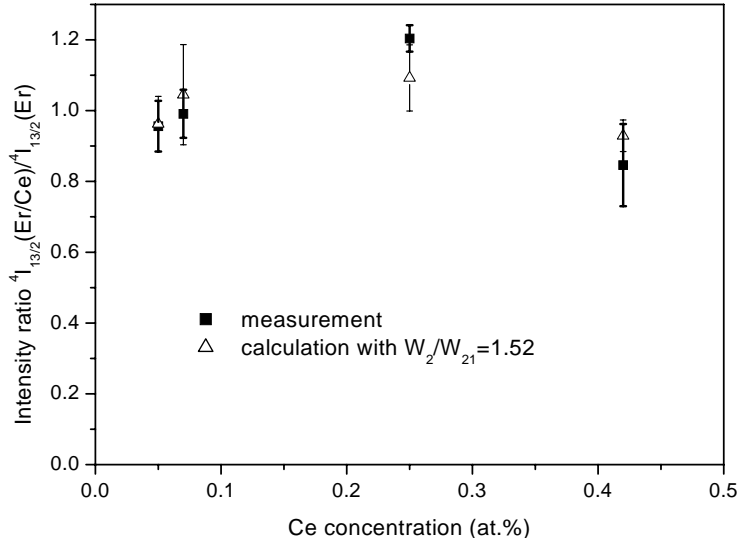


FIGURE 3.5: Ratio of the intensity at 1538 nm emitted by the $\text{Er}^{3+} \ ^4\text{I}_{13/2}$ level in the presence and absence of cerium. Included are calculations according to equation (3.4) using data from figure 3.2 as input.

3.4 Comparison of the effects of cerium and europium codoping

Let us briefly compare three results obtained in this chapter with our previous measurements on Er^{3+} in Y_2O_3 codoped with europium (chapter 2). For the case of codoping with europium we determined the energy transfer coefficient C_2 to be $2.9 \cdot 10^{-18} \text{ cm}^3/\text{s}$, more than a factor of two higher than for codoping with cerium. According to Dexter (1953), multipolar energy transfer depends on the overlap integral between donor emission and acceptor absorption. Comparing the energy level structure of Ce^{3+} and Eu^{3+} in Y_2O_3 (Chang et al., 1982; Chang and Gruber, 1964) shows that the higher transfer efficiency towards Eu^{3+} is due to the better spectral overlap between the $\text{Er}^{3+} \ ^4\text{I}_{11/2} \rightarrow \ ^4\text{I}_{13/2}$ transition and the Eu^{3+} energy levels. Measurements in glasses of different compositions (Meng et al., 2000; Choi et al., 2000b) suggest that energy transfer between Er^{3+} and Ce^{3+} contains a phonon-assisted contribution. A similar process is suggested by decay rate measurements at different temperatures on our samples. These are shown in figure 3.6. Plotted are the decay rates of the $\text{Er}^{3+} \ ^4\text{I}_{11/2}$ state for a sample codoped with 0.25 at.% cerium and a reference without cerium. Both sets of decay rate measurements show an increase with temperature, due to phonon-assisted de-excitation to the $\ ^4\text{I}_{13/2}$ state. The energy transfer rate W_{tr} , also drawn in figure 3.6, increases with temperature as well, by 60% over the temperature range between 13 K and 300 K. Since the energy transfer

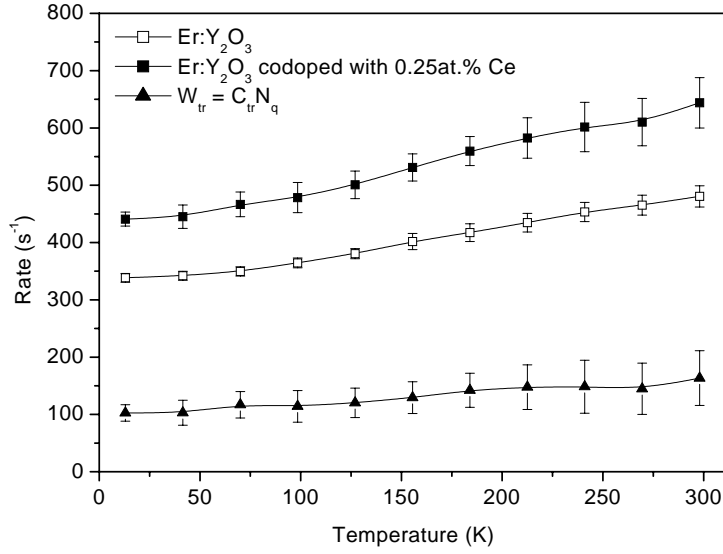


FIGURE 3.6: Measured decay rates of Er^{3+} ($^4\text{I}_{11/2}$ state) in samples with 0 at.% and 0.25 at.% cerium as a function of temperature. The energy transfer rate W_{tr} from Er^{3+} to Ce^{3+} is derived from these measurements. The drawn lines are guides to the eye.

rate does not vanish at 13 K we can conclude that some direct energy transfer from Er^{3+} to Ce^{3+} takes place. Although the accuracy of these measurements is limited, the temperature dependence of W_{tr} suggests a considerable phonon-mediated component at room temperature. The poor overlap together with this phonon-assisted contribution can explain the lower efficiency for energy transfer between Er^{3+} and Ce^{3+} .

It is interesting to note the correspondence of the values for the adjustable parameter (W_{1r}) in the fit of equation 3.3 to the intensity ratio data for experiments involving different acceptor ions. It amounts to 89 s^{-1} for both energy transfer between Er^{3+} and Eu^{3+} presented in chapter 2 and energy transfer between Er^{3+} and Ce^{3+} described in this chapter. This fact supports the claim that all transitions from the $^4\text{I}_{11/2}$ state induced by the codopants have the $^4\text{I}_{13/2}$ level as their final state: if an interaction were present de-exciting part of the population in the $^4\text{I}_{11/2}$ state directly to the ground state, the value for the adjustable parameter obtained from the ratio of the $^4\text{I}_{13/2}/^4\text{I}_{11/2}$ intensities would depend on the strength of this interaction. The interaction strength in turn depends on the energy level structure of the codopant, and treatment conditions. Both are different for the two sample series and should therefore lead to different values of W_{1r} . Since this is not the case, the dominant de-excitation of the $^4\text{I}_{11/2}$ state induced by the codopant must be to the $^4\text{I}_{13/2}$ level.

The similar dependence of Q_{1538} for both series, especially the sudden increase around 0.4 at.% codopant, is clear evidence that its cause are indeed defects induced

by the ion implantation. While energy transfer interactions with the codopant ions proper depend on the respective level structure, the defect spectrum only depends on the energy loss per distance of the implanted ions in the host matrix. The level structure of Eu^{3+} and Ce^{3+} , however, is clearly different, while the energy loss is very similar, due to the similar ion masses and implantation energies used.

3.5 Summary

In this chapter we have shown that in a Y_2O_3 host the ${}^4\text{I}_{11/2} \rightarrow {}^4\text{I}_{13/2}$ transition in Er^{3+} can be accelerated by energy transfer to Ce^{3+} . In the process the population in the first excited state increases at the expense of the population in the second excited state. In this way the population inversion for amplification around 1540 nm is enhanced. This method is especially interesting for host materials with low phonon energies, whose steady state population in the second excited state of Er^{3+} is high when excited with 980 nm radiation. In our experiments, an energy transfer efficiency of 0.47 was measured for a cerium concentration of 0.42 at.%. The energy transfer coefficient was determined to be $1.3 \cdot 10^{-18} \text{ cm}^3/\text{s}$.

The energy transfer between the ${}^4\text{I}_{11/2}$ state of Er^{3+} and Ce^{3+} in Y_2O_3 is less efficient than that between Er^{3+} and Eu^{3+} . This is attributed to the smaller spectral overlap of the $\text{Er}^{3+} {}^4\text{I}_{11/2} \rightarrow {}^4\text{I}_{13/2}$ transition with the absorption of the ${}^2\text{F}_{7/2}$ state of Ce^{3+} .

Chapter FOUR

Absorption and emission spectroscopy in Er^{3+} - Yb^{3+} doped aluminum oxide waveguides

THE SPECTROSCOPIC PROPERTIES OF Al_2O_3 WAVEGUIDES ION-IMPLANTED WITH Er^{3+} AND Yb^{3+} ARE INVESTIGATED IN VIEW OF THEIR APPLICATION IN OPTICAL AMPLIFIERS OPERATING AT 1530 NM. ABSORPTION CROSS SECTIONS ARE OBTAINED BY MEANS OF WAVEGUIDE TRANSMISSION EXPERIMENTS, TAKING INTO ACCOUNT THE OVERLAP BETWEEN OPTICAL MODE AND DOPED REGION OF THE WAVEGUIDE. EMISSION CROSS SECTIONS FOR THE $\text{Er}^{3+} : ^4\text{I}_{13/2}$ AND $\text{Yb}^{3+} : ^2\text{F}_{5/2}$ LEVELS ARE CALCULATED FROM THE ABSORPTION CROSS SECTIONS. THE RATE CONSTANT FOR ENERGY TRANSFER BETWEEN Yb^{3+} AND Er^{3+} UNDER EXCITATION AROUND 980 NM IS ESTIMATED BY EMISSION INTENSITY AND DECAY RATE MEASUREMENTS. IT AMOUNTS TO APPROXIMATELY $3.6 \cdot 10^{-17} \text{ cm}^3/\text{s}$ FOR CONCENTRATIONS OF 0.29 AT.% ERBIUM AND 0.28 AT.% YTTERBIUM.

Erbium-doped amplifiers are by now an indispensable element in optical fibre telecommunications systems. They are able to provide high gain in the spectral region around 1530 nm, where silica fibres have their transmission maximum. In the field of miniature integrated optics, erbium-doped waveguide amplifiers (Kitagawa et al., 1992; Ghosh et al., 1996; van den Hoven et al., 1996a; van Weerden et al., 1997; Yan et al., 1997) have proven their ability to provide optical gain over short distances. The first generation of integrated amplifiers used mainly laser diodes emitting at 1480 nm for optical pumping. Under this excitation scheme, the metastable $^4I_{13/2}$ level of the erbium ions is excited directly into its high-lying Stark states. The ions act as a quasi three-level laser system, which limits the population inversion with respect to the ground state to roughly 40 % (corresponding to a population in the first excited state of 70 %) because of stimulated emission by pump radiation. On the other hand, when pumping into the second excited state $^4I_{11/2}$ using 980 nm radiation, a population inversion between metastable level and ground state of close to 100 % can be obtained.

This second excitation scheme of Er^{3+} in waveguide amplifiers requires considerably higher intensities, since the absorption cross section of the $^4I_{11/2}$ state is small. The excitation cross section of Er^{3+} around 980 nm can however be increased by codoping with ytterbium (cf. figure 4.1 for a schematic of the process). The absorption cross section of Yb^{3+} at 980 nm is about an order of magnitude larger than that of Er^{3+} , and its absorption band extends over a wider wavelength region, between 850 nm and 1000 nm. From Yb^{3+} the energy is then transferred resonantly to the $^4I_{11/2}$ state of Er^{3+} . This energy transfer has been investigated in a wide range of materials, both glassy and crystalline (see e.g. Artem'ev et al. (1981); Zandi et al. (1994); Simondi-Teisseire et al. (1996); Hehlen et al. (1997); Cantelar et al. (1998)). Based on this excitation scheme, an integrated amplifier in phosphate glass has been reported (Delavaux et al., 1997).

Important characteristics of amplifier materials are the optical absorption and emission cross sections of the dopants. They determine, in conjunction with the efficiency of the energy transfer between Yb^{3+} and Er^{3+} , the maximum gain and pumping efficiency of an amplifier. The cross sections of rare earth ions are too small to be easily obtained by standard normal-incidence spectroscopy in thin film structures. Transmission experiments through waveguides increase the interaction length of the light with the dopant ions, and therefore the total absorbance. For samples where only the guiding region is doped, several research groups have shown that absorbance spectra of the dopants can be obtained in this way (Lázaro et al., 1998; Orignac et al., 1999), yet the results are all of a qualitative nature.

In this chapter, we will investigate the absorption and emission properties of Er^{3+} and Yb^{3+} in Al_2O_3 . Aluminum oxide has already been reported as a suitable host medium for Er^{3+} -doped optical waveguide amplifiers (van den Hoven et al., 1996a). It has also been shown that in this material energy transfer between Yb^{3+} and Er^{3+} (Chryssou et al., 1998) takes place. We need to obtain, however, quantitative data that will allow us to estimate whether ytterbium codoping will lead to an

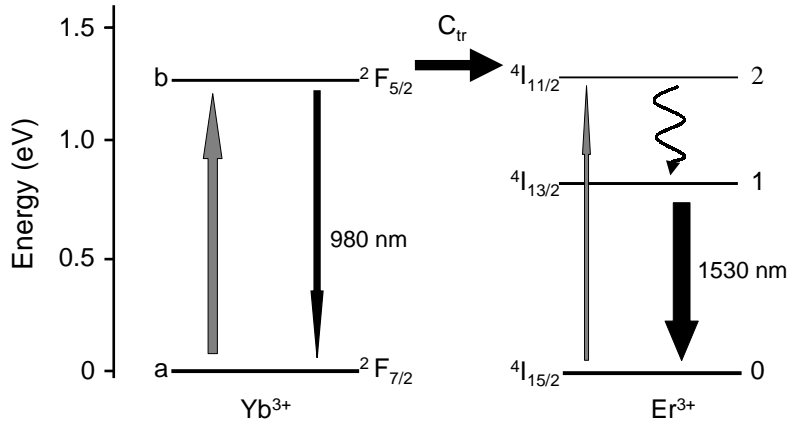


FIGURE 4.1: Schematic of the energy transfer process between Yb^{3+} and Er^{3+} . Excitation takes place around 980 nm and can excite both erbium and ytterbium. Yb^{3+} either decays to its ground state or transfers its energy to the Er^{3+} $^4\text{I}_{11/2}$ level. Within the erbium, decay of the $^4\text{I}_{11/2}$ state to the $^4\text{I}_{13/2}$ state leads to a build-up of population in the metastable $^4\text{I}_{13/2}$ level.

improvement in amplifier performance. To this end we will address two types of questions associated with a waveguide amplifier codoped with Er^{3+} and Yb^{3+} : in section 4.2 we will obtain absolute values for the absorption cross sections from waveguide transmission measurements and calculate the relevant emission cross sections. In section 4.3 we will determine the efficiency of the energy transfer between Yb^{3+} and Er^{3+} from measurements of emitted intensities from the Er^{3+} $^4\text{I}_{13/2}$ state, and independently from measurements of Yb^{3+} decay rates.

4.1 Sample preparation and characterisation techniques

Aluminum oxide films were deposited on thermally oxidized silicon wafers by RF-sputtering (Smit et al., 1986; Smit, 1991). The thickness of the Al_2O_3 and SiO_2 layers was 500 nm and $5\ \mu\text{m}$ respectively. Erbium and ytterbium were introduced into the Al_2O_3 film by ion implantation at energies ranging from 1800 keV to 200 keV, creating a flat dopant profile throughout most of the film. The dopant concentrations were determined by Rutherford Backscattering Spectrometry (RBS) and amount to $3.35 \cdot 10^{20}\ \text{Er}/\text{cm}^3$ (0.29 at.%) and $3.28 \cdot 10^{20}\ \text{Yb}/\text{cm}^3$ (0.28 at.%). Besides the sample doped with erbium and ytterbium, samples containing only erbium or ytterbium were

prepared. For reference purposes, a piece was kept unimplanted.

Straight waveguides of widths ranging from $1\ \mu\text{m}$ to $3.5\ \mu\text{m}$ were defined by standard photolithographic techniques. Ridges were etched to a depth of approximately $200\ \text{nm}$ with an argon atom beam. Subsequently a cover layer of $1.35\ \mu\text{m}$ SiO_2 was sputtered onto the waveguides. The samples were cut to a length of $8\ \text{mm}$ and the cleaved edges were mechanically polished. Finally they were annealed in vacuum for an hour at $775\ ^\circ\text{C}$.

The exact shape of the waveguides was determined using Scanning Electron Microscopy on typical waveguide samples before the deposition of the cover layer. The acceleration voltage for these measurements was $15\ \text{kV}$.

Waveguide transmission measurements were performed by coupling white light from a halogen lamp into one facet of a waveguide with the help of a lensed fibre. The transmitted signal was collected at the output facet with a $40\times$ microscope objective and imaged onto the tip of a fibre with a core diameter of $600\ \mu\text{m}$. The collected light was dispersed in a $96\ \text{cm}$ monochromator and detected with a thermoelectrically cooled AgOCs photomultiplier tube in the spectral region between $400\ \text{nm}$ and $1100\ \text{nm}$, and with a liquid nitrogen cooled germanium detector in the region from $1100\ \text{nm}$ to $1700\ \text{nm}$. Standard lock-in techniques were used to decrease the noise level. The wavelength resolution of these measurements was approximately $3\ \text{nm}$.

To obtain photoluminescence spectra and decay curves of Er^{3+} and Yb^{3+} , the ions were excited with a continuous wave titanium sapphire laser, tunable in the range from $890\ \text{nm}$ to $1030\ \text{nm}$. The pump radiation was mechanically chopped and coupled into the waveguide from an optical fibre. The photoluminescence signal was detected perpendicular to the waveguide through the top cladding using a fibre with an $600\ \mu\text{m}$ core. The detection system was the same as described above. The AgOCs photomultiplier tube was used to measure the Yb^{3+} emission at wavelengths around $1000\ \text{nm}$, and the germanium detector to measure the photoluminescence of Er^{3+} around $1530\ \text{nm}$. Decay curves for the Er^{3+} emission were recorded using a digital oscilloscope, for the Yb^{3+} emission using a photon counting system. The time response of the detection set-up was $40\ \mu\text{s}$. Special care has been taken to ensure that all measurements were performed at excitation densities where both the Yb^{3+} and Er^{3+} emission intensities are directly proportional to pump power.

To obtain a calibration of the photoluminescence intensity at $1530\ \text{nm}$ of erbium-only and erbium-ytterbium doped Al_2O_3 relative to each other under $980\ \text{nm}$ excitation, spectra of the $^4\text{I}_{13/2}$ emission were taken in standard photoluminescence geometry: the excitation beam was incident onto the sample surface under an angle of 30° , and the emitted light was focussed onto the entrance slit of the monochromator.

4.2 Waveguide transmission measurements

The transmission of a $3.5\ \mu\text{m}$ wide waveguide doped with Er^{3+} and a $2.5\ \mu\text{m}$ wide waveguide doped with Yb^{3+} was measured as a function of wavelength. As reference served the spectrum of transmitted intensity through an undoped waveguide. In this

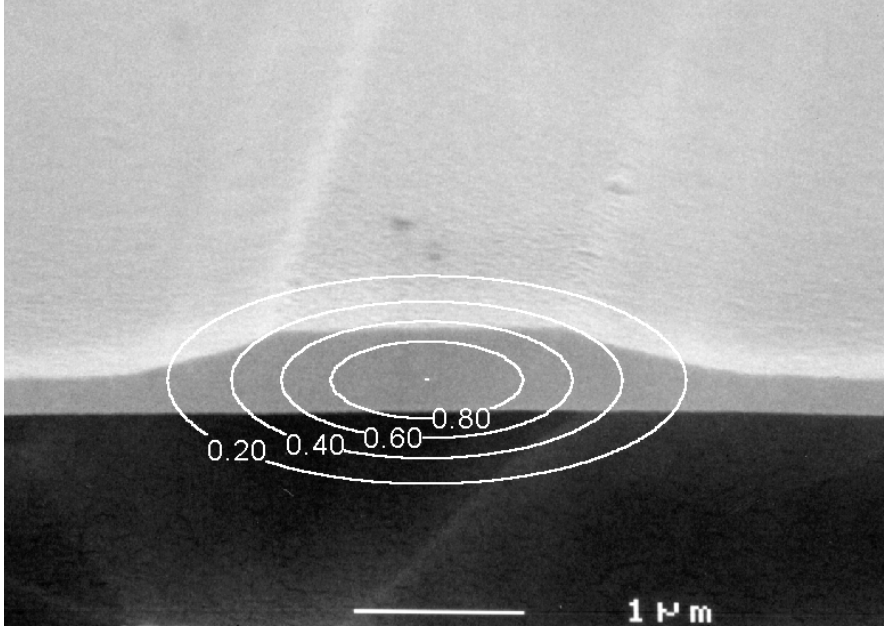


FIGURE 4.2: Scanning Electron Microscopy image of the cross section of an Al_2O_3 ridge waveguide with nominal width $2\ \mu\text{m}$. The image was taken before the deposition of the SiO_2 cover layer. The SiO_2 buffer layer underneath the Al_2O_3 waveguide appears black. Included is the intensity contour plot of the fundamental mode at 980 nm for the complete waveguide structure, calculated by a finite difference method. The overlap between mode and doped region of the waveguide has to be taken into account to obtain absolute cross section values from waveguide transmission measurements.

way the effects of absorption by the rare earths can be extracted from a signal which also contains the effects of the waveguiding properties of the structure itself. Since scattering effects can be excluded in this way, the transmission data is converted to absorbance assuming a Lambert-Beer dependency. The absorption cross section is related to the absorbance through

$$\sigma_{abs}(\lambda) = \frac{A(\lambda)}{\eta_{\text{overlap}}(\lambda) \cdot N_{abs} \cdot l} \quad (4.1)$$

where σ_{abs} is the absorption cross section, A the absorbance, η_{overlap} the overlap between waveguide mode and doped region, and N_{abs} and l the concentration of the dopant and the length of the waveguide respectively.

To obtain absolute values for the absorption cross section in waveguide transmission measurements, it is important to know the exact cross section of the waveguide and the development of the mode shape with wavelength over the range investigated. Figure 4.2 shows a Scanning Electron Microscope image of the cross section of a nomi-

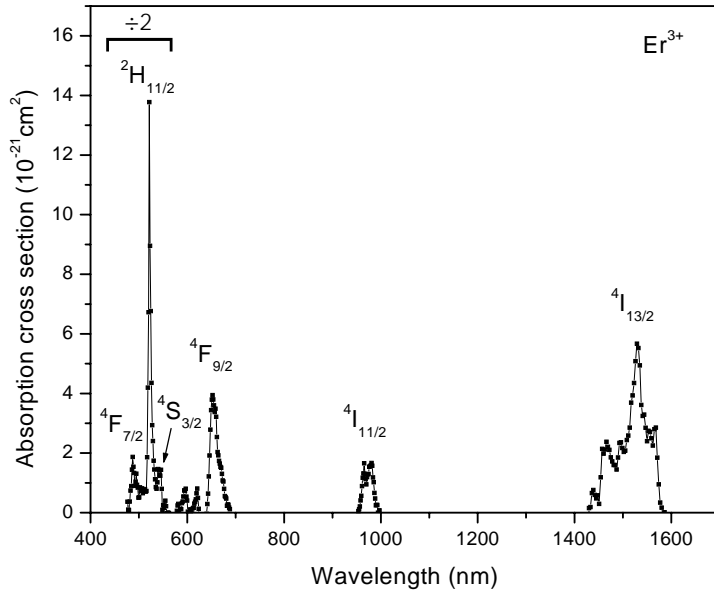


FIGURE 4.3: Absorption cross section of Er^{3+} obtained from waveguide transmission experiments. Transitions are from the ground state to the indicated excited states. The absorption of the ${}^4\text{I}_{9/2}$ level was below the sensitivity of our measurement. Note that the absorption cross section in the wavelength range 475 nm to 560 nm has been reduced by a factor of two.

nally $2\ \mu\text{m}$ wide waveguide. Included is a contour profile of the fundamental mode for 980 nm radiation calculated numerically using a finite difference algorithm. Although the image shows a waveguide without the SiO_2 cover layer for better contrast, the calculation has been performed taking account of the final geometry including the cover layer. For all waveguide widths used in the transmission measurements, mode profiles were calculated for several wavelengths, taking into consideration the dispersion of SiO_2 and Al_2O_3 . The calculated profiles were approximated by two-dimensional Gaussian functions, and integrated over the dopant profile, measured by Rutherford Backscattering Spectrometry, and the waveguide profile to obtain the overlap η_{overlap} . A second order polynomial was used to phenomenologically describe the functional dependence of η_{overlap} with wavelength.

Although great care was taken to ensure that only the fundamental mode was present, it is possible that higher order modes propagate in the waveguide during measurement. These higher order modes have a smaller overlap with the doped core of the waveguide than the fundamental mode, reducing their modal absorption. Therefore, for accuracy, the values we calculate from the transmission data have to be seen as lower limits to the real absorption cross sections.

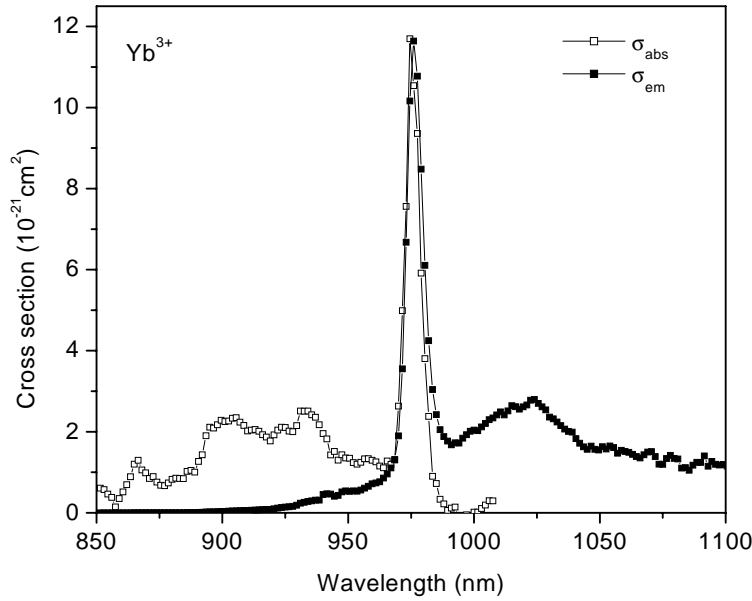


FIGURE 4.4: Absorption and emission cross section of the ${}^2F_{5/2}$ level of Yb^{3+} . The absorption cross section was obtained from waveguide transmission measurements, the emission cross section calculated using absorption and photoluminescence data.

Figure 4.3 shows the absorption cross section of Er^{3+} in the Al_2O_3 waveguides determined as described above. All energy levels up to ${}^4F_{7/2}$ are given, and marked in the figure, except the ${}^4I_{9/2}$ level, expected around 800 nm, whose absorbance was below the accuracy of our measurement. The highest absorption cross section occurs at 521 nm, belonging to the ${}^2H_{11/2}$ level. The error on the peak cross section in this case amounts to $1 \cdot 10^{-20} \text{ cm}^2$, considerably larger than the error on the other absorption cross sections, since the intensity of the transmitted light is close to zero at that wavelength. The peaks around 600 nm are caused by noise in the measurement and can serve as an indication for the accuracy of the cross section values. Note that in figure 4.3 the absorption cross sections in the wavelength range 475 nm to 560 nm have been reduced by a factor of two. The peak cross sections for the individual energy levels are listed in table 4.1.

The measured absorption cross section of the $\text{Yb}^{3+} {}^2F_{5/2}$ level is depicted in figure 4.4. At its peak, the ytterbium absorption cross section is seven times larger than the absorption cross section of the $\text{Er}^{3+} {}^4I_{11/2}$ level. In the following section we will show that this high cross section can be used to advantage to increase the excitation rate of Er^{3+} by energy transfer from Yb^{3+} . The determination of the cross sections from these waveguide transmission measurements is validated by the close correspondence between the absorption cross section values of the $\text{Er}^{3+} {}^4I_{13/2}$ level

TABLE 4.1: Peak absorption and emission cross sections in Al_2O_3 for Er^{3+} and Yb^{3+} energy levels. Absorption of the given levels originates from a ground state transition of the ion, emission involves a transition to the ground state.

| Ion | Energy level | λ_{peak} [nm] | σ_{abs} [10^{-21} cm^2] | σ_{em} [10^{-21} cm^2] |
|------------------|-----------------------|---------------------------------|--|---|
| Er^{3+} | ${}^4\text{I}_{13/2}$ | 1529.0 | 5.7 ± 0.7 | 5.7 |
| | | 1532.0 | | |
| | ${}^4\text{I}_{11/2}$ | 980.5 | 1.7 ± 0.7 | |
| | ${}^4\text{I}_{9/2}$ | | < 0.7 | |
| | ${}^4\text{F}_{9/2}$ | 652.0 | 4.0 ± 0.7 | |
| | ${}^4\text{S}_{3/2}$ | 545.5 | 2.9 ± 0.7 | |
| | ${}^2\text{H}_{11/2}$ | 521.5 | 27.6 ± 10 | |
| | ${}^4\text{F}_{7/2}$ | 487.0 | 3.7 ± 0.7 | |
| Yb^{3+} | ${}^2\text{F}_{5/2}$ | 974.5 | 11.7 ± 1.0 | 11.6 |

obtained here and previously by prism coupling (van den Hoven et al., 1997).

Using the measured absorption cross sections, emission cross sections from the Er^{3+} ${}^4\text{I}_{13/2}$ and Yb^{3+} ${}^2\text{F}_{5/2}$ levels to the corresponding ground states were calculated using the theory developed by McCumber (1964) as applied to rare earth ions by Miniscalco and Quimby (1991). Since in both cases the measured cross sections in the wings of the absorption lines are not sufficiently accurate to calculate the emission cross sections, we scaled the photoluminescence emission spectra of the relevant transitions to the value of the cross section calculated at their peak. As an example the emission cross section of Yb^{3+} is included in figure 4.4. Numerical values of the cross section maxima are given in table 4.1.

4.3 Energy transfer

The effect of ytterbium codoping on the photoluminescence of Er^{3+} is depicted in figure 4.5. Two spectra of the emission from the ${}^4\text{I}_{13/2}$ level of Er^{3+} are shown. The more intense one originates from the sample doped with erbium and ytterbium, the weaker one from the sample doped only with erbium. The photoluminescence was excited under identical conditions using radiation at 975 nm. On ytterbium codoping, the photoluminescence is increased sixfold. The lineshape of the emission remains unchanged by the introduction of ytterbium into the sample, as does the decay rate of the ${}^4\text{I}_{13/2}$ level, measured at 1533 nm to be 625 s^{-1} .

To obtain a qualitative impression of the excitation mechanism, we have monitored the photoluminescence from the Er^{3+} ${}^4\text{I}_{13/2}$ line as a function of excitation wave-

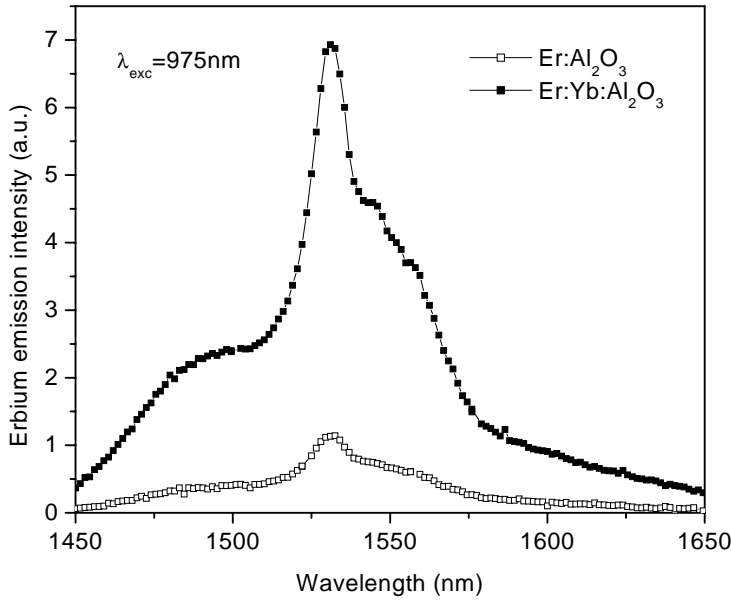


FIGURE 4.5: Comparison of photoluminescence emission spectra of the $\text{Er}^{3+} \ ^4I_{13/2}$ level in samples doped with erbium and with ytterbium and erbium. The emission is enhanced by a factor of six on ytterbium codoping under identical excitation conditions ($\lambda_{\text{excitation}} = 975 \text{ nm}$, $I_{\text{excitation}} = 0.5 \text{ W/cm}^2$).

length between 890 nm and 1030 nm. Care was taken to optimize the coupling of the excitation light into the waveguide for all wavelengths used. The excitation spectra of samples doped with erbium and erbium-ytterbium are shown in figure 4.6. In the sample without ytterbium, erbium can only be excited in a narrow band centred at 975 nm and extending from 955 nm to 1000 nm. This band resembles the erbium absorption cross section shown in figure 4.3. In contrast, when the sample is codoped with ytterbium, an identical emission at 1532 nm can be excited over a much wider wavelength range, with a sharp peak at 975 nm. This peak is a characteristic of the $\text{Yb}^{3+} \ ^2F_{5/2}$ absorption. The excitation spectrum of the erbium emission from the ytterbium codoped sample is replotted in figure 4.7, to compare it with the absorption cross section from figure 4.4. From the fact that both spectra show the same features, we can conclude that the pump radiation is mainly absorbed by Yb^{3+} . Energy transfer from Yb^{3+} to Er^{3+} then takes place as depicted in figure 4.1. Since the absorption line of Yb^{3+} extends even to shorter wavelengths than were accessible in our experiment, excitation of Er^{3+} emission is not limited to the wavelengths shown in the plot. Chrissy et al. (1998) have measured the excitation spectrum of Er^{3+} in erbium-ytterbium codoped Al_2O_3 between 760 nm and 850 nm, which we extend here to longer wavelengths. The fact that excitation of the Er^{3+} is possible even when ex-

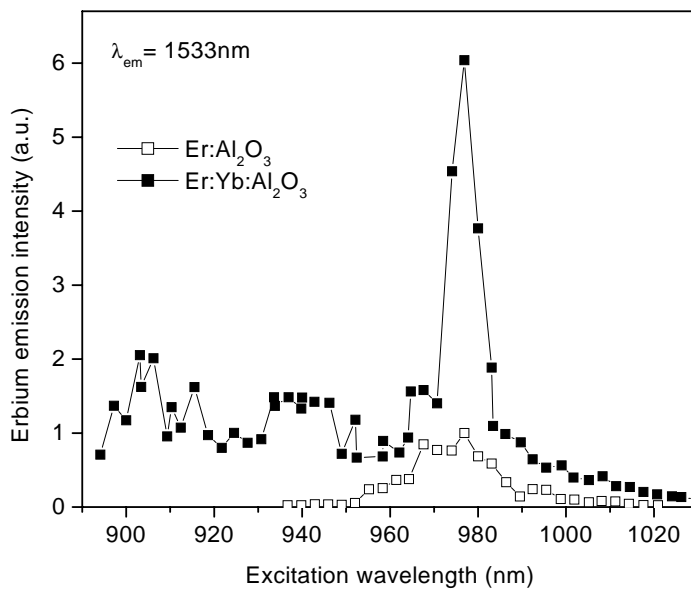


FIGURE 4.6: Excitation spectra of the $\text{Er}^{3+} \ ^4I_{13/2}$ emission from erbium doped Al_2O_3 and erbium-ytterbium codoped Al_2O_3 .

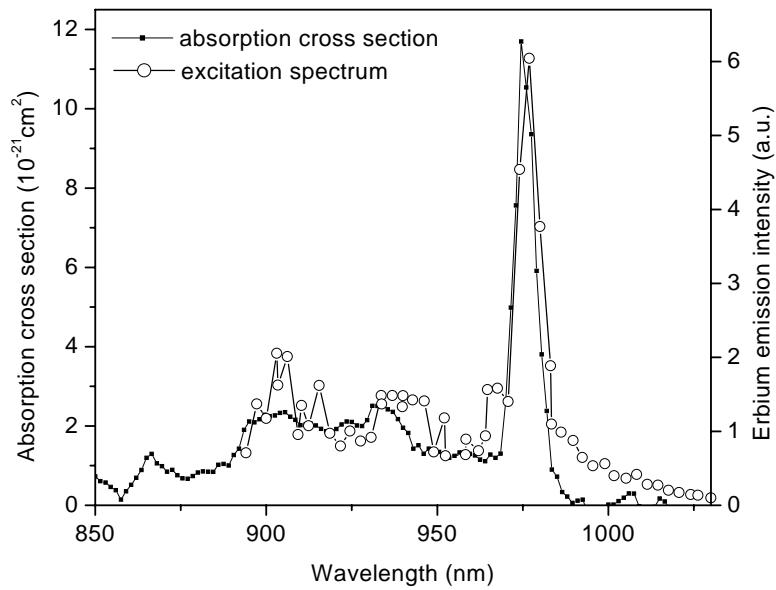


FIGURE 4.7: Comparison of the excitation spectrum of the erbium emission at 1530 nm and the absorption cross section of Yb^{3+} obtained by waveguide transmission experiments.

citing outside the $\text{Er}^{3+} {}^4\text{I}_{11/2}$ absorption band is evidence for a thermalisation process within the ytterbium system, possibly involving migration of excitation.

The ratio of the Er^{3+} emission intensity in the Er-doped and Er/Yb-codoped samples (compare figure 4.6) contains information about the efficiency of the energy transfer process. The rate equations in the limit of low excitation density according to the schematic figure 4.1 are:

$$\begin{aligned}\frac{dN_b}{dt} &= \sigma_{ab}\Phi_p N_{Yb} - W_b N_b - C_{tr} N_b N_{Er} \\ \frac{dN_2}{dt} &= \sigma_{02}\Phi_p N_{Er} + C_{tr} N_b N_{Er} - W_2 N_2 \\ \frac{dN_1}{dt} &= W_{21} N_2 - W_1 N_1\end{aligned}\quad (4.2)$$

In these equations N_1 and N_2 represent the population densities of the first and second excited states of Er^{3+} , and N_b the population density in the excited state of Yb^{3+} (cf. the labels in figure 4.1), while N_{Er} and N_{Yb} are the total erbium and ytterbium concentrations. σ_{ab} and σ_{02} signify the absorption cross sections of Yb^{3+} and Er^{3+} at the excitation wavelength, respectively. W_1 , W_2 , and W_b represent the total decay rates of the corresponding levels in the absence of energy transfer, W_{21} is the transition rate from the ${}^4\text{I}_{11/2}$ to ${}^4\text{I}_{13/2}$ level in Er^{3+} , and C_{tr} the energy transfer coefficient. Φ_p is the photon flux density of the exciting radiation. The rate equations in absence of ytterbium are easily obtained by setting N_{Yb} and N_b zero.

C_{tr} is an effective energy transfer coefficient including forward and back energy transfer. As long as the populations of the $\text{Yb}^{3+} {}^2\text{F}_{5/2}$ and $\text{Er}^{3+} {}^4\text{I}_{11/2}$ levels are linear functions of excitation power, C_{tr} is independent of pump photon flux.

In steady state, the populations of the $\text{Er}^{3+} {}^4\text{I}_{13/2}$ level are given by

$$\begin{aligned}N_1^{ErYb} &= \frac{W_{21}}{W_2} \frac{1}{W_1} \left(\sigma_{02} N_{Er} + \frac{C_{tr} N_{Er}}{W_b + C_{tr} N_{Er}} \sigma_{ab} N_{Yb} \right) \Phi_p \\ N_1^{Er} &= \frac{W_{21}}{W_2} \frac{1}{W_1} \sigma_{02} N_{Er} \Phi_p\end{aligned}\quad (4.3)$$

following rate equations (4.2). Here the superscripts $ErYb$ and Er denote the cases with ytterbium codoping and without, respectively. Assuming the radiative decay rate of the $\text{Er}^{3+} {}^4\text{I}_{13/2}$ level is not changed on codoping with Yb^{3+} , which is reasonable considering that the decay rate of the erbium emission does not change, the ratio R of the erbium emission intensity is given by the ratio of populations in the first excited state.

$$R = \frac{N_1^{ErYb}}{N_1^{Er}} = 1 + \frac{C_{tr} N_{Er}}{W_b + C_{tr} N_{Er}} \frac{\sigma_{ab}}{\sigma_{02}} \frac{N_{Yb}}{N_{Er}}\quad (4.4)$$

The term $(C_{tr} N_{Er}) / (W_b + C_{tr} N_{Er})$ is the transfer efficiency, which can be obtained from equation (4.4) since all other parameters are known (R from figure 4.6, σ_{ab} and

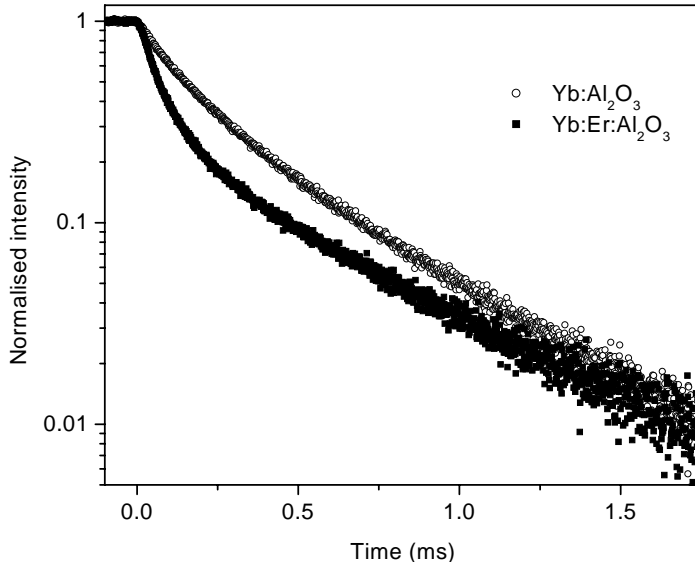


FIGURE 4.8: Decay traces of the Yb^{3+} emission at 976 nm in ytterbium-doped and erbium/ytterbium-codoped Al_2O_3 , excited with 921 nm radiation. The increase in decay rate on codoping with erbium reflects the energy transfer from Yb^{3+} to Er^{3+} .

σ_{02} from figures 4.3 and 4.4, N_{Yb} and N_{Er} from RBS measurements). At an excitation wavelength of 975 nm the energy transfer efficiency amounts to 0.62. This also means that 38% of the power absorbed by Yb^{3+} is lost via radiative or nonradiative processes, and not via an energy transfer to Er^{3+} . The corresponding energy transfer coefficient C_{tr} is $3.3 \cdot 10^{-17} \text{ cm}^3/\text{s}$.

The energy transfer efficiency can be estimated independently from the $\text{Yb}^{3+} \ ^4\text{F}_{5/2}$ decay rate. Figure 4.8 shows the Yb^{3+} decay traces of a reference sample doped only with ytterbium and of the codoped sample. For these measurements, the photoluminescence was excited at 921 nm and monitored at 976 nm. The faster decay of the codoped sample is caused by the fact that the energy transfer towards Er^{3+} constitutes an additional decay channel for the excited state of Yb^{3+} . The absence of a detector response time-limited step in the decay traces at $t = 0$ shows that decay components faster than the detector response are negligible. For single exponential decays, the energy transfer rate is simply given by

$$W_{tr} = C_{tr} N_{\text{Er}} = W^{\text{YbEr}} - W^{\text{Yb}} \quad (4.5)$$

Here W_{tr} represents the transfer rate from Yb^{3+} to Er^{3+} , and W^{YbEr} and W^{Yb} the measured $\text{Yb}^{3+} \ ^2\text{F}_{5/2}$ decay rates in the codoped and Yb-doped samples, respectively. Both decay traces in figure 4.8, however, are multi-exponential, which has to be taken into account when calculating the transfer rates by using correct weights for

the contributions to intensity of ions with different photoluminescence properties. A transfer efficiency of 0.68 ($C_{tr} = 4 \cdot 10^{-17} \text{ cm}^3/\text{s}$) is obtained, in close correspondence to the value calculated from equation (4.4).

4.4 Summary

In this article we have studied the spectroscopic properties of Al_2O_3 waveguides doped with Er^{3+} and Yb^{3+} . The important parameters for application of these waveguides as optical amplifiers in the spectral region around 1530 nm are the absorption and emission cross sections of Er^{3+} and Yb^{3+} , and the rate of the energy transfer between Yb^{3+} and Er^{3+} .

By measuring the transmission through waveguides doped with Er^{3+} and Yb^{3+} we have been able to obtain absorption cross section data for most of the absorption lines of the two dopant ions in the spectral region between 400 nm and 1700 nm. Important for our procedure are an exact knowledge of the waveguiding structure and the development of the optical mode size with wavelength. From the absorption cross section of the $\text{Er}^{3+} \ ^4\text{I}_{13/2}$ and $\text{Yb}^{3+} \ ^2\text{F}_{5/2}$ states, the emission cross sections of these energy levels were obtained by application of McCumber theory.

The energy transfer was investigated by both photoluminescence intensity measurements of the $\ ^4\text{I}_{13/2}$ level of Er^{3+} and by decay rate measurements of the $\ ^2\text{F}_{5/2}$ level of Yb^{3+} . The photoluminescence excitation spectrum of the $\text{Er}^{3+} \ ^4\text{I}_{13/2}$ emission around 1530 nm of erbium-ytterbium codoped Al_2O_3 resembles the $\text{Yb}^{3+} \ ^2\text{F}_{5/2}$ absorption line under excitation in the wavelength range between 890 nm and 1030 nm. This is clear evidence of energy transfer from Yb^{3+} to Er^{3+} . By ytterbium codoping, the $\text{Er}^{3+} \ ^4\text{I}_{13/2}$ emission intensity is enhanced by a factor of six when excited at 975 nm. The rate coefficient for energy transfer between the $\text{Yb}^{3+} \ ^2\text{F}_{5/2}$ and the $\text{Er}^{3+} \ ^4\text{I}_{11/2}$ states amounts to approximately $3.6 \cdot 10^{-17} \text{ cm}^3/\text{s}$.

Chapter FIVE

Relationship between gain and Yb^{3+} concentration in Er^{3+} - Yb^{3+} doped waveguide amplifiers

WE HAVE INVESTIGATED THE DEPENDENCE OF GAIN ON YB^{3+} CONCENTRATION USING A RATE EQUATION PROPAGATION MODEL OF AN $\text{ER}^{3+}/\text{YB}^{3+}$ DOPED AL_2O_3 WAVEGUIDE AMPLIFIER. THE MODEL INCLUDES EXCITED STATE ABSORPTION AND ENERGY TRANSFER UPCONVERSION PROCESSES WITHIN THE ER^{3+} AS WELL AS THE RELEVANT ENERGY TRANSFER PROCESSES BETWEEN YB^{3+} AND ER^{3+} . THE RESULTS OF THE CALCULATIONS INDICATE A CLOSE RELATIONSHIP OF THE PARAMETERS GAIN, LAUNCHED PUMP POWER, WAVEGUIDE LENGTH, AND YB^{3+} CONCENTRATION. CODOPING WITH A WELL-CHOSEN YB^{3+} CONCENTRATION IS SHOWN TO INCREASE THE GAIN AROUND 1530 NM FOR ALL COMBINATIONS OF THESE PARAMETERS. THE GAIN IS IMPROVED MOST BY YB^{3+} CODOPING AT PUMP POWERS AROUND THE AMPLIFIER THRESHOLD. AT HIGH PUMP POWERS THE INCREASE IN GAIN OF AN $\text{ER}^{3+}/\text{YB}^{3+}$ DOPED WAVEGUIDE IS INSIGNIFICANT COMPARED TO THAT OF ITS ER^{3+} DOPED COUNTERPART. FURTHERMORE, FOR EACH PUMP POWER A NONZERO YB^{3+} CONCENTRATION CAN BE DETERMINED, THAT MAXIMIZES THE GAIN.

The triply charged ytterbium ion's strong absorption around 980 nm has made it an obvious candidate for use as a sensitizer for other luminescing ions. Codoping with Yb^{3+} has been shown to increase the photoluminescence or upconversion fluorescence emitted by the rare earth ions Pr^{3+} , Eu^{3+} , Tb^{3+} , Er^{3+} , and Tm^{3+} (Auzel, 1973; Hehlen et al., 1997; Cantelar et al., 1998; Page et al., 1998; Tanabe et al., 1999; Mita et al., 1999; Qiu et al., 2000; Hwang et al., 2000). Even Cr^{4+} can be sensitized via Yb^{3+} (Choi et al., 2000a). The greater part of these studies has been made on codoping materials with Er^{3+} and Yb^{3+} , due to the Er^{3+} ion's relevance in optical amplifiers for communication networks operating around 1550 nm. Sensitization in this case relies on the fact that the ${}^2\text{F}_{5/2}$ level of Yb^{3+} and the ${}^4\text{I}_{11/2}$ level of Er^{3+} are nearly resonant in energy. Due to its high absorption cross section, Yb^{3+} absorbs the pump radiation at 980 nm efficiently and can transfer this absorbed energy to Er^{3+} (see chapter 4). This process is more power efficient than direct excitation of Er^{3+} in many materials, i.e. per incoming photon more Er^{3+} is excited.

This excitation scheme has been put to many different uses. Lasers operating in the wavelength window from 1530 nm to 1560 nm have been demonstrated (Taccheo et al., 1996; Alouini et al., 1998; Veasey et al., 2000). In the area of optical communications, fibre amplifiers and integrated optical amplifiers codoped with Er^{3+} and Yb^{3+} show gain around 1530 nm (Townsend et al., 1991; Wysocki et al., 1996; Barbier et al., 1997).

Naturally, with the technology developed to this extent, great effort has gone into modelling $\text{Er}^{3+}/\text{Yb}^{3+}$ doped amplifiers (Nilsson et al., 1994; Federighi and Di Pasquale, 1995; Lester et al., 1995; Karásek, 1997; Cantelar et al., 2000; Chryssou et al., 2001). In this way performance of a waveguide amplifier can be predicted based on the material it consists of and the waveguide configuration used. Obtaining accurate values for the relevant parameters of Er^{3+} and Yb^{3+} remains the central problem, and few results of the model calculations in the literature can be compared because of differing waveguide geometries.

Our purpose is to reach a qualitative understanding of the physics behind the dependence of the amplification on Yb^{3+} concentration in $\text{Er}^{3+}/\text{Yb}^{3+}$ doped waveguide amplifiers. Part of this problem was already addressed by Nilsson et al. (1994) for short fibres. We have chosen to investigate Al_2O_3 waveguides mainly for two reasons: first, gain has been reported in an Er^{3+} doped Al_2O_3 waveguide (van den Hoven et al., 1996a), and we can use the respective waveguide cross section. Second, Al_2O_3 has been investigated in great detail with respect to Er^{3+} and Yb^{3+} doping (van den Hoven et al., 1997, 1996b; Strohhöfer and Polman, 2001, see chapter 4), so most – but not all – of the cross sections, decay rates, and energy transfer rates necessary as input to the model are known. For the purpose of this chapter, the unknown parameters have been filled in by comparison with similar materials.

This work is not aimed at making accurate predictions of the gain in the structure we have modelled. This would be impossible in view of the uncertainty in some of the material constants. We have therefore, for simplicity, also chosen to ignore amplified spontaneous emission (ASE). From the point of view of systems engineering

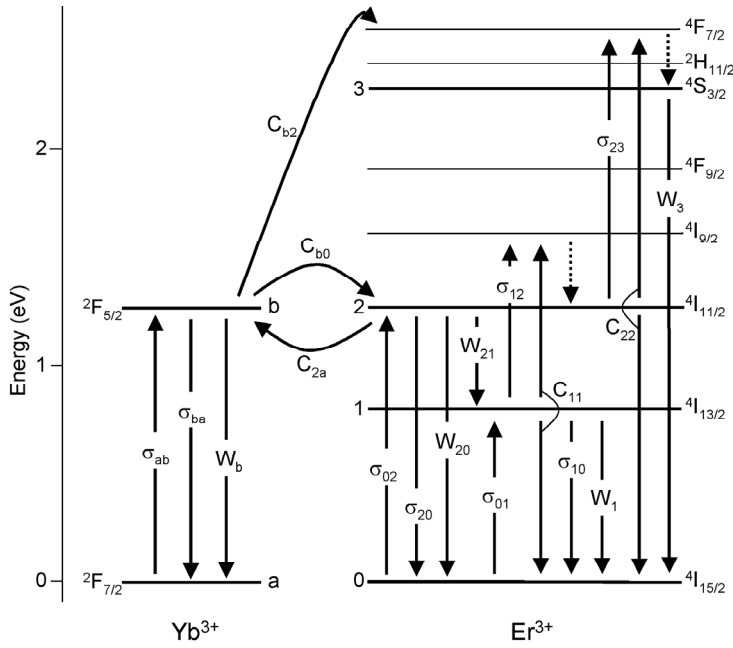


FIGURE 5.1: Energy level diagram of Er^{3+} and Yb^{3+} . The arrows represent the processes included in the rate equation model used for the calculations. Included are absorption and stimulated emission processes (σ_{ij}), spontaneous decays (W_{ij}) and energy transfer processes (C_{ij}). Dashed arrows represent spontaneous processes considered as instantaneous.

this is of course a faux pas, since ASE is one of the major factors limiting amplifier performance. It leads to a reduction of the gain proportional to the average inversion in the waveguide and is therefore proportional to the gain itself (Shaklee et al., 1973). However it does not influence the dependence of the gain features on Yb^{3+} concentration.

In the following we will briefly introduce the rate equations and the propagation model we have utilised to describe the $\text{Er}^{3+}/\text{Yb}^{3+}$ doped waveguide amplifier. Subsequently, we will describe the results of our calculations and discuss their implications for the design of waveguide amplifiers.

5.1 The model

We calculate the gain with a rate equation propagation model. The processes included in the model are depicted in figure 5.1. Absorption and stimulated processes are characterised by their respective cross sections σ_{if} , where i and f indicate the initial and final energy levels of the process. Spontaneous decay is identified by its rate W_{if} .

If no final level f is given, the corresponding decay rate W_i signifies the sum of all individual decay rates from level i to lower lying states.

A third kind of process included in the model is energy transfer between Yb^{3+} and Er^{3+} or between two excited Er^{3+} ions. These processes are characterized by their energy transfer rate constants C_{ij} . Here the subscripts i and j denote the energy levels populated prior to energy transfer. Furthermore all transitions indicated by dashed arrows in figure 5.1 are considered to be instantaneous.

The underlying assumption for this rate equation model to be valid is that excitation redistributes freely within both the Er^{3+} and the Yb^{3+} subsystems. This is the case when the concentration of the two ions is high enough to allow for energy migration.

The complete set of equations determining the population of the energy levels for this system is:

$$\frac{dN_b}{dt} = \sigma_{ab}\Phi_p N_a - \sigma_{ba}\Phi_p N_b - W_b N_b - C_{b0}N_b N_0 + C_{2a}N_a N_2 - C_{b2}N_b N_2, \quad (5.1)$$

$$N_{Yb} = N_a + N_b, \quad (5.2)$$

$$\frac{dN_1}{dt} = \sigma_{01}\Phi_s N_0 - \sigma_{10}\Phi_s N_1 - \sigma_{12}\Phi_s N_1 + W_{21}N_2 - W_1 N_1 - 2C_{11}N_1^2, \quad (5.3)$$

$$\begin{aligned} \frac{dN_2}{dt} = & \sigma_{02}\Phi_p N_0 - \sigma_{20}\Phi_p N_2 + \sigma_{12}\Phi_s N_1 - \sigma_{23}\Phi_p N_2 - W_2 N_2 \\ & + C_{11}N_1^2 - 2C_{22}N_2^2 + C_{b0}N_b N_0 - C_{2a}N_a N_2 - C_{b2}N_b N_2, \end{aligned} \quad (5.4)$$

$$\frac{dN_3}{dt} = \sigma_{23}\Phi_p N_2 - W_3 N_3 + C_{22}N_2^2 + C_{b2}N_b N_2, \quad (5.5)$$

$$N_{Er} = N_0 + N_1 + N_2 + N_3. \quad (5.6)$$

In these equations, N_i represents the population density of the energy level marked i in figure 5.1, with $i \in \{a, b, 0, 1, 2, 3\}$. Φ_p and Φ_s are the photon flux densities of the pump and signal radiation, respectively. The equations are solved for steady state at a given pump photon flux and for negligible signal photon flux (the so-called small-signal limit).

Figure 5.2 shows the cross section of the ridge waveguide we have assumed in these calculations. It is patterned after the waveguides fabricated by van den Hoven et al. (1996a,b). It consists of an Al_2O_3 core, considered homogeneously doped with Er^{3+} and Yb^{3+} (indices of refraction $n(\lambda = 1530 \text{ nm}) = 1.65$ and $n(\lambda = 980 \text{ nm}) = 1.74$) surrounded by a thick cladding of SiO_2 (indices of refraction $n(\lambda = 1530 \text{ nm}) = 1.445$ and $n(\lambda = 980 \text{ nm}) = 1.451$). The thick part of the waveguide has a width of $2 \mu\text{m}$ and a thickness of 500 nm . Outside this central region, an Al_2O_3 film of 250 nm remains. The optical modes supported by this structure were calculated with a finite difference mode solver and approximated by two-dimensional Gaussian functions. Note that waveguides of this shape and size are single mode at 1530 nm but not at 980 nm . We have calculated the gain assuming that only the fundamental mode at 980 nm is present in the waveguide. Including higher order modes at the pump wavelength will lead to a reduction of the gain of the system (Vermelho et al., 2000).

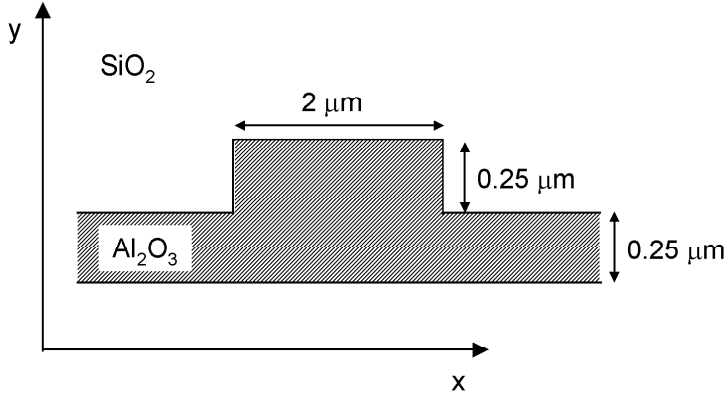


FIGURE 5.2: Schematic cross section of the waveguide used for the calculations. A ridge structure of Al_2O_3 is embedded in SiO_2 . The complete Al_2O_3 core is doped homogeneously with Er^{3+} , and with Yb^{3+} if applicable. The narrow part of the Al_2O_3 structure extends to infinity in $+x$ and $-x$ direction. Note that the x - and y -axes have different scales.

We calculate the development of the power in pump and signal mode over the length of the waveguides. Pump and signal are copropagating. The optical power contained in the pump and signal modes is governed by

$$\begin{aligned}
 \frac{dP_p(z)}{dz} &= \frac{d}{dz} \iint_{\text{core}} \Phi_p(x, y, z) \cdot h\nu_p \, dx \, dy \\
 &= \iint_{\text{core}} \Phi_p(x, y, z) \cdot h\nu_p \\
 &\quad \left(-\sigma_{ab}N_a(x, y, z) + \sigma_{ba}N_b(x, y, z) - \sigma_{02}N_0(x, y, z) \right. \\
 &\quad \left. + \sigma_{20}N_2(x, y, z) - \sigma_{23}N_2(x, y, z) - \alpha_p \right) dx \, dy \quad (5.7)
 \end{aligned}$$

$$\begin{aligned}
 \frac{dP_s(z)}{dz} &= \frac{d}{dz} \iint_{\text{core}} \Phi_s(x, y, z) \cdot h\nu_s \, dx \, dy \\
 &= \iint_{\text{core}} \Phi_s(x, y, z) \cdot h\nu_s \\
 &\quad \left(-\sigma_{01}N_0(x, y, z) + \sigma_{10}N_1(x, y, z) - \sigma_{12}N_1(x, y, z) - \alpha_s \right) dx \, dy \quad (5.8)
 \end{aligned}$$

In these relations, $h\nu_p$ and $h\nu_s$ are the energies of a pump and signal photon, respectively. α_p describes the waveguide scattering loss at the pump wavelength, and α_s at the signal wavelength. The position dependence of the population of the different energy levels is a consequence of its dependence on pump photon flux density, $N_i(x, y, z) = N_i(\Phi_p(x, y, z))$. The integral has to be evaluated in the Al_2O_3 part of the structure, since only this region is assumed to be doped with Er^{3+} and Yb^{3+} .

Table 5.1: Parameters used for the numerical calculations

| Parameter | Symbol | Value | Source |
|--|---------------|--------------------------------------|---|
| Signal wavelength | λ_s | 1530 nm | |
| Pump wavelength | λ_p | 975 nm | |
| Er concentration | N_{Er} | $3.35 \cdot 10^{20} \text{ cm}^{-3}$ | van den Hoven et al. (1996b) |
| Decay rate of $\text{Yb}^{3+} \ ^2\text{F}_{5/2}$ | W_6 | 1000 s^{-1} | unpublished measurement |
| Decay rate of $\text{Er}^{3+} \ ^4\text{I}_{13/2}$ | W_1 | 200 s^{-1} | van den Hoven et al. (1996a) |
| Decay rate of $\text{Er}^{3+} \ ^4\text{I}_{11/2}$ | W_2 | 30000 s^{-1} | van den Hoven et al. (1996a) |
| Transition rate $\text{Er}^{3+} \ ^4\text{I}_{11/2} \rightarrow \ ^4\text{I}_{13/2}$ | W_{21} | 28000 s^{-1} | cf. section 5.2 |
| Decay rate of $\text{Er}^{3+} \ ^4\text{S}_{3/2}$ | W_3 | 100000 s^{-1} | cf. section 5.2 |
| Absorption cross section $\text{Yb}^{3+} \ ^2\text{F}_{5/2}$ at λ_p | σ_{ab} | $1.2 \cdot 10^{-20} \text{ cm}^2$ | Strohhöfer and Polman (2001) |
| Emission cross section $\text{Yb}^{3+} \ ^2\text{F}_{5/2}$ at λ_p | σ_{ba} | $1.2 \cdot 10^{-20} \text{ cm}^2$ | Strohhöfer and Polman (2001) |
| Absorption cross section $\text{Er}^{3+} \ ^4\text{I}_{11/2}$ at λ_p | σ_{02} | $2 \cdot 10^{-21} \text{ cm}^2$ | Strohhöfer and Polman (2001) |
| Emission cross section $\text{Er}^{3+} \ ^4\text{I}_{11/2}$ at λ_p | σ_{20} | $2 \cdot 10^{-21} \text{ cm}^2$ | Strohhöfer and Polman (2001) |
| Absorption cross section $\text{Er}^{3+} \ ^4\text{I}_{13/2}$ at λ_s | σ_{01} | $6 \cdot 10^{-21} \text{ cm}^2$ | van den Hoven et al. (1997); Strohhöfer and Polman (2001) |
| Emission cross section $\text{Er}^{3+} \ ^4\text{I}_{13/2}$ at λ_s | σ_{10} | $6 \cdot 10^{-21} \text{ cm}^2$ | van den Hoven et al. (1997); Strohhöfer and Polman (2001) |
| ESA cross section $\text{Er}^{3+} \ ^4\text{I}_{13/2}$ at λ_s | σ_{12} | $1 \cdot 10^{-21} \text{ cm}^2$ | van den Hoven et al. (1996b), cf. section 5.2 |
| ESA cross section $\text{Er}^{3+} \ ^4\text{I}_{11/2}$ at λ_p | σ_{23} | $0 \cdot 10^{-21} \text{ cm}^2$ | Labbé et al. (2000); Danger et al. (1994), cf. section 5.2 |

Table 5.1: (continued)

| Parameter | Symbol | Value | Source |
|--|------------|--|--|
| Energy transfer rate constant $\text{Yb}^{3+} \rightarrow \text{Er}^{3+}$ (${}^2\text{F}_{5/2} + {}^4\text{I}_{15/2} \rightarrow {}^2\text{F}_{7/2} + {}^4\text{I}_{11/2}$) | C_{b2} | $4 \cdot 10^{-17} \text{ cm}^3/\text{s}$ | Strohhofer and Polman (2001) |
| Energy transfer rate constant $\text{Er}^{3+} \rightarrow \text{Yb}^{3+}$ (${}^4\text{I}_{11/2} + {}^2\text{F}_{7/2} \rightarrow {}^4\text{I}_{15/2} + {}^2\text{F}_{5/2}$) | C_{2b} | $4 \cdot 10^{-17} \text{ cm}^3/\text{s}$ | cf. section 5.2 |
| Energy transfer rate constant $\text{Yb}^{3+} \rightarrow \text{Er}^{3+}$ (${}^2\text{F}_{5/2} + {}^4\text{I}_{11/2} \rightarrow {}^2\text{F}_{7/2} + {}^4\text{F}_{7/2}$) | C_{b3} | $4 \cdot 10^{-17} \text{ cm}^3/\text{s}$ | cf. section 5.2 |
| Cooperative upconversion coefficient Er^{3+} (${}^4\text{I}_{13/2} + {}^4\text{I}_{13/2} \rightarrow {}^4\text{I}_{9/2} + {}^4\text{I}_{15/2}$) | C_{11} | $4 \cdot 10^{-18} \text{ cm}^3/\text{s}$ | van den Hoven et al. (1996b) |
| Cooperative upconversion coefficient | C_{22} | $2 \cdot 10^{-18} \text{ cm}^3/\text{s}$ | Peters et al. (1999), cf. section 5.2 |
| Er^{3+} (${}^4\text{I}_{11/2} + {}^4\text{I}_{11/2} \rightarrow {}^4\text{F}_{7/2} + {}^4\text{I}_{15/2}$) | | | |
| Waveguide loss at λ_s | α_s | 0.07 cm^{-1} | Smit (1991) |
| Waveguide loss at λ_p | α_p | 0.09 cm^{-1} | Smit (1991) |

5.2 The choice of the parameters

The decay rates, absorption and emission cross sections, and energy transfer rate constants used as input in our calculations are based on measurements in Al_2O_3 , as far as available. Many parameters, especially cross sections and ytterbium–erbium energy transfer rate constant, have become available only recently (Strohhöfer and Polman, 2001, chapter 4). All parameters are listed in table 5.1. We will here comment on some of these parameters and make plausible our choice for those that have not yet been determined experimentally.

The energy transfer coefficient from Yb^{3+} to Er^{3+} is known to depend on ytterbium concentration for low concentrations, but is constant at high concentrations. Concentration dependent determination of C_{b0} in glasses (Gapontsev and Platonov, 1989) has shown that C_{b0} does not vary a lot for ytterbium concentrations higher than the minimum value we have used in the calculations ($N_{\text{Yb}} = 3.35 \cdot 10^{20} \text{ cm}^{-3}$). It therefore seems reasonable to assume C_{b0} constant in our calculations. The energy back transfer rate coefficient C_{2a} is very similar to C_{b0} in many materials (Cantelar et al., 1998; Wyss et al., 1997). We take $C_{2a} = C_{b0}$. The exact value of C_{2a} however has little influence on the numerical result because the population in the second excited state of Er^{3+} remains low even at high pump powers and therefore energy back transfer is not important. We also assume that $C_{b2} = C_{b0}$, since the broad emission spectrum of Yb^{3+} ensures a spectral overlap with the ${}^4\text{F}_{7/2}$ state comparable to that with the ${}^4\text{I}_{11/2}$ state. The assumption that the transition matrix elements involved in the energy transfer processes are equal is also reasonable. The transfer rate constant for cooperative upconversion processes from the Er^{3+} ${}^4\text{I}_{11/2}$ level, C_{22} , is unknown in Al_2O_3 . Published data for this parameter in different materials show, however, that this coefficient is often close to $2 \cdot 10^{-18} \text{ cm}^3/\text{s}$ (Peters et al., 1999). Therefore we have assumed this value to approximate C_{22} in Al_2O_3 .

The excited state absorption cross section from the ${}^4\text{I}_{13/2}$ state for radiation at 1530 nm, σ_{12} , is also not known. We use the cross section for 1480 nm radiation instead (van den Hoven et al., 1996b). Furthermore, there are no data on excited state absorption originating from the ${}^4\text{I}_{11/2}$ level of Er^{3+} in Al_2O_3 . In other crystalline materials such as YAG or LiYF_4 the relevant cross section σ_{23} at 980 nm is negligible (Danger et al., 1994; Labbé et al., 2000). A nonzero cross section will of course affect the population inversion between ${}^4\text{I}_{13/2}$ state and ground state, however its influence is limited by the low population in the ${}^4\text{I}_{11/2}$ level and will become significant only for extremely high pump powers.

The branching ratio of the Er^{3+} ${}^4\text{I}_{11/2}$ state, which determines the rate W_{21} , is not known. However, it is known that the emission from the ${}^4\text{I}_{11/2}$ state to the ground state around 980 nm is very weak compared to the transition originating from the ${}^4\text{I}_{13/2}$ level at 1530 nm. This fact has been taken into account through the choice of the value for W_{21} (28000 s^{-1}). Finally there is no measured value available for the decay rate of the Er^{3+} ${}^4\text{S}_{3/2}$ state W_3 in Al_2O_3 . It is generally fast compared to the decay rates of both the ${}^4\text{I}_{11/2}$ and ${}^4\text{I}_{13/2}$ states (Kabro et al., 1997; Tsuda et al., 2000). We choose $W_3 = 10^5 \text{ s}^{-1}$. As the branching ratio toward the ground state is

high, most of the energy upconverted to this level is lost.

5.3 The simulations

In the following paragraphs we will discuss the signal output from Er^{3+} doped ridge waveguides codoped with various concentrations of Yb^{3+} . We will try and elucidate the physical mechanisms behind these data. However we have to bear in mind that our model, with the peculiar cross section of the waveguide that has an $\text{Er}^{3+}/\text{Yb}^{3+}$ doped region even at a large distance from the waveguide core (cf. figure 5.2), is not the simplest one possible to extract the physical principles from. It is rather based on a structure realised experimentally, which has been reported to show gain under excitation at 1480 nm (van den Hoven et al., 1996a). The optimal Er^{3+} concentration determined in the same series of work (van den Hoven et al., 1996a,b) ($3.35 \cdot 10^{20} \text{ cm}^{-3}$) has been used as the starting point in our calculations.

5.3.1 Gain at a fixed waveguide length

Figure 5.3 (a) shows the small-signal gain as a function of launched pump power at 980 nm for a fixed waveguide length of 8 cm. Plotted are results for several Yb^{3+} concentrations between $3.35 \cdot 10^{20} \text{ cm}^{-3}$ and $26.8 \cdot 10^{20} \text{ cm}^{-3}$, as well as for a waveguide doped only with Er^{3+} .

At low pump powers, the Er^{3+} is not inverted and most of the signal is absorbed. Increasing the pump power we first notice an effect on the signal output of the waveguide containing no Yb^{3+} . As the Yb^{3+} concentration is increased, the curves in figure 5.3 (a) show a smaller initial increase with pump power. This behaviour is caused by the higher absorption cross section of Yb^{3+} with respect to Er^{3+} , which limits the propagation of the pump through the waveguide and therefore the length over which the Er^{3+} is inverted. The gain at 1530 nm is determined by the difference in populations of the Er^{3+} ${}^4\text{I}_{13/2}$ and ${}^4\text{I}_{15/2}$ energy manifolds averaged over the waveguide length.

Increasing the pump power further will eventually enhance the signal leaving the $\text{Er}^{3+}/\text{Yb}^{3+}$ doped waveguide over the signal leaving the Er^{3+} doped waveguide. This enhancement will take place at higher and higher pump powers as the Yb^{3+} concentration is increased. For very high pump powers, however, the signal output from all waveguides only depends on the Er^{3+} concentration and reaches the same value for all Yb^{3+} concentration. This is the limit of full inversion of all Er^{3+} ions in the waveguide.

Figure 5.3 (b) shows the corresponding data for a waveguide of 4 cm length. The details of this graph are the same as described for figure 5.3 (a), although shifted to lower pump power. This is to be expected as the total depletion of the pump is less in the shorter waveguide, resulting in a greater fraction of the Er^{3+} that is excited. However, the figure better illustrates the behaviour at high pump powers, namely the output signal approaching its high pump power limit for all Yb^{3+} concentrations (the

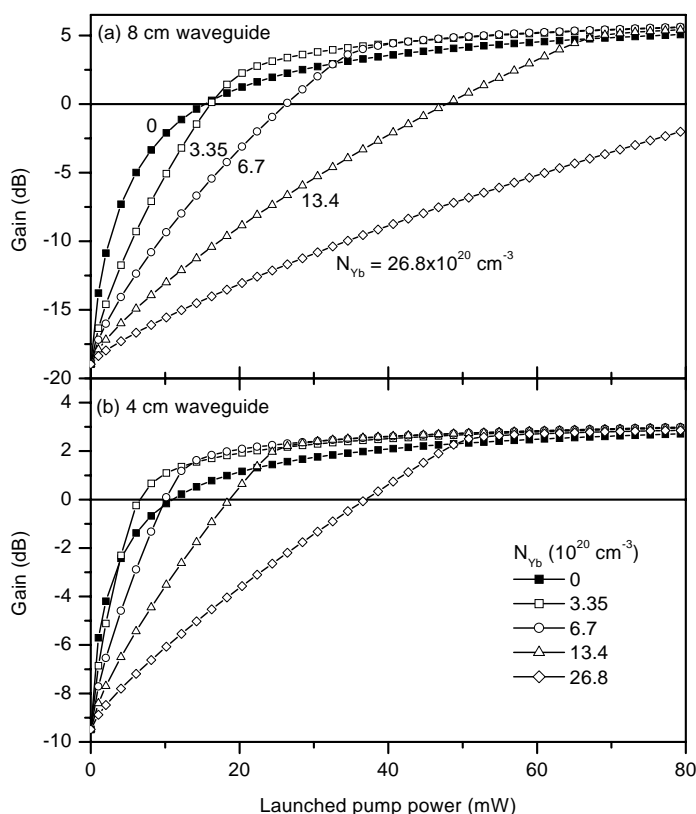


FIGURE 5.3: Calculations of signal output from a waveguide of fixed length doped with $3.35 \cdot 10^{20} \text{ cm}^{-3} \text{ Er}^{3+}$ as a function of launched pump power. Different symbols represent different Yb^{3+} concentrations. Waveguide length: (a) 8 cm, (b) 4 cm.

slight variations in gain at high pump powers reflect the differences in inversion of Er^{3+} in the tails of the signal mode).

The saturation at high pump power naturally follows from the energy transfer mechanism between Yb^{3+} and Er^{3+} . Considering the model depicted in figure 5.1 it is clear that the efficiency of the energy transfer from Yb^{3+} to Er^{3+} is limited by the transfer rate constant C_{2a} and the population in the Er^{3+} ground state (assuming for simplicity that W_2 is high, i.e. the population of the $\text{Er}^{3+} \text{ } ^4\text{I}_{11/2}$ state is negligible, we can neglect energy back transfer and energy transfer to higher lying states). This means that by increasing the launched pump power we will eventually reach a regime in which the excitation of Er^{3+} via Yb^{3+} can be neglected against its direct excitation. This is due both to the depletion of the ground state population of Er^{3+} and to the limitation on the energy transfer provided by the finite energy transfer rate constant, which is independent of pump power. If the amplifier is operated at such pump

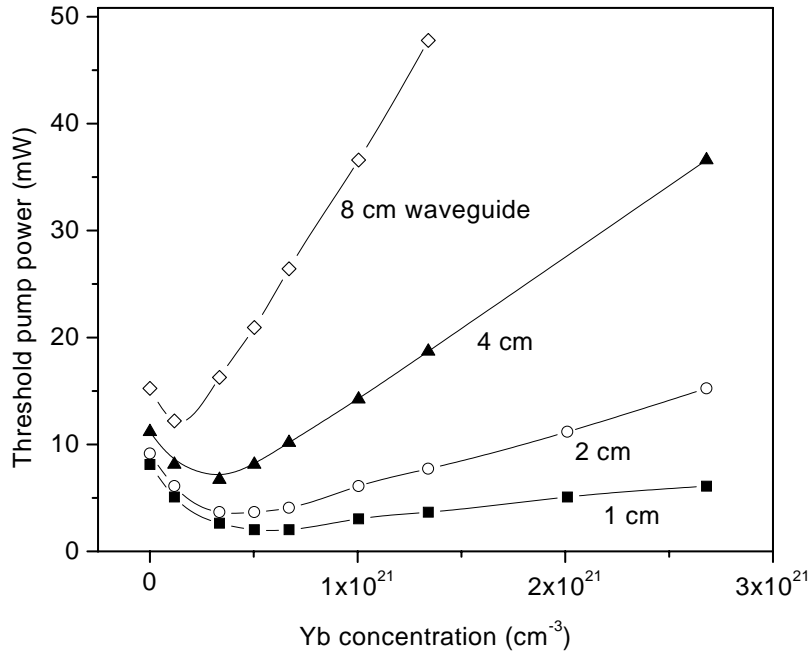


FIGURE 5.4: The pump power threshold for net gain as a function of Yb^{3+} concentration for waveguides of different lengths. The drawn lines are guides to the eye. For increasing waveguide length, the minimum threshold power is achieved at decreasing Yb^{3+} concentration.

powers, Yb^{3+} codoping will only have a marginal effect (in our case only seen in the tails of the mode) and will be unnecessary.

On the other end of the power scale, there is however a rather clear correlation between gain threshold, length of the waveguide, and Yb^{3+} concentration. While for the 8 cm waveguide (figure 5.3 (a)) the gain threshold for $N_{\text{Yb}} = 0$ and $N_{\text{Yb}} = 3.35 \cdot 10^{20} \text{ cm}^{-3}$ nearly coincides, we see that for waveguides of 4 cm length concentrations of $N_{\text{Yb}} = 3.35 \cdot 10^{20} \text{ cm}^{-3}$ and $N_{\text{Yb}} = 6.7 \cdot 10^{20} \text{ cm}^{-3}$ have a lower gain threshold than the waveguide with no Yb^{3+} . For any length of the waveguide there is thus a corresponding Yb^{3+} concentration, which will decrease the threshold pump power to a minimum. This is shown in figure 5.4, which depicts the threshold pump power as a function of Yb^{3+} concentration for waveguides of different lengths. The minimum of the threshold power shifts to smaller and smaller Yb^{3+} concentrations for increasing waveguide length. This results from a tradeoff between the higher excitation efficiency of the Er^{3+} via Yb^{3+} and the depletion of the pump due to the high Yb^{3+} absorption cross section when propagating along the waveguide. When too much Yb^{3+} is added to the waveguide, the threshold for signal gain increases, the more rapidly, the longer the waveguide. Here we have chosen the gain threshold to demonstrate the depen-

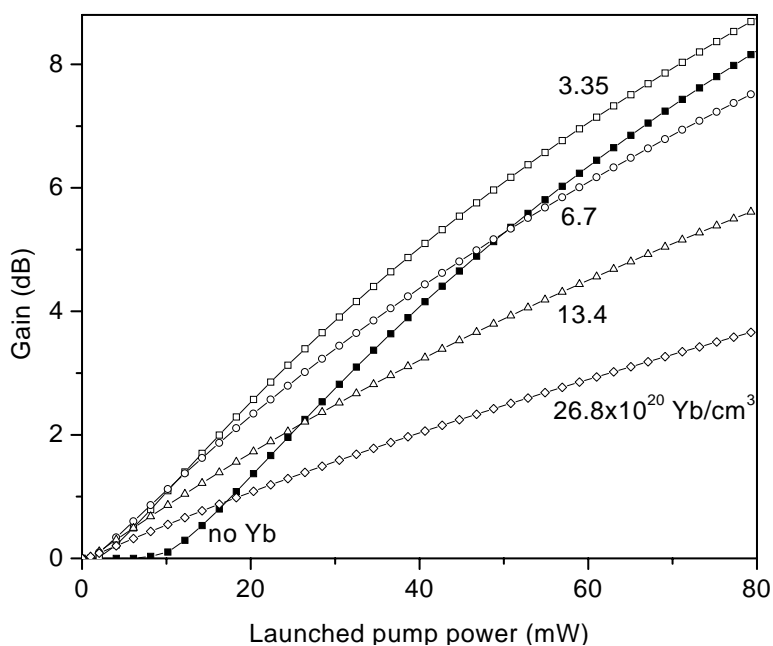


FIGURE 5.5: Calculation of the maximum possible signal output from a waveguide doped with $3.35 \cdot 10^{20} \text{ cm}^{-3} \text{ Er}^{3+}$ as a function of launched pump power. Different symbols represent different concentrations of Yb^{3+} . The length of the waveguides has been adjusted for maximum gain for each Yb^{3+} concentration and each launched pump power.

dence of pump power necessary to reach a certain gain level on Yb^{3+} concentration. Similar curves are obtained for any given signal output.

Returning to figure 5.3 we can see that the gain of an Er^{3+} doped waveguide amplifier is improved significantly by Yb^{3+} codoping only if it is operated at a pump power around its threshold, under the condition that the Yb^{3+} concentration is not too high. A high Yb^{3+} concentration therefore not only causes a high gain threshold, but also produces very little improvement in gain over the case with no Yb^{3+} . The effect of the large absorption of Yb^{3+} on the gain has to be taken into account when designing Er/Yb-doped waveguide amplifiers.

5.3.2 Maximum gain

In figure 5.5 we have plotted the results of calculations of the maximum gain as a function of launched pump power for several Yb^{3+} concentrations between $3.35 \cdot 10^{20} \text{ cm}^{-3}$ and $26.8 \cdot 10^{20} \text{ cm}^{-3}$. In addition, the calculated gain in a waveguide doped exclusively with Er^{3+} is depicted.

Each point in the plot represents a waveguide whose length is optimised for maximum gain at a given pump power. This means that the length of the waveguide is chosen such that at its end the transparency condition, an average inversion of zero over the cross section of the waveguide, is fulfilled. Consequently, the length of the waveguide differs for each of the points in the plot, both as a function of pump power for a given Yb^{3+} concentration, and as a function of Yb^{3+} concentration itself. Over the pump power range represented, the length of the waveguide without Yb^{3+} varies between 0 and 18 cm, and that of the waveguide doped with $26.8 \cdot 10^{20} \text{ Yb}^{3+} / \text{cm}^3$ between 0 and 5.5 cm, to give an impression of the values involved.

There are several noteworthy points about this plot. First, the threshold injected pump power for gain decreases with increasing Yb^{3+} concentration. This is a consequence of the higher excitation probability of Er^{3+} via Yb^{3+} at low pump powers, which is caused by the high absorption cross section of Yb^{3+} and efficient energy transfer toward Er^{3+} .

Second, the slope of the curves, once the gain threshold is reached, decreases with increasing Yb^{3+} concentration. This is a signature of the higher conversion efficiency of absorbed pump photons for waveguides with smaller Yb^{3+} concentration. The lower the concentration of Yb^{3+} , the smaller the losses of pump energy caused by spontaneous decay of the Yb^{3+} ion. This feature becomes especially important for high inversion of the Er^{3+} , since in this case the probability is small that an excited Yb^{3+} ion can transfer its energy to an Er^{3+} ion in its ground state.

This also means that with increasing launched pump power, waveguides with higher Yb^{3+} concentration will eventually have less gain than waveguides with lower Yb^{3+} concentration. As a consequence, the maximum gain curves of waveguides with different Yb^{3+} concentrations will cross at a certain pump power. Several of these crossings can be seen in figure 5.5. Incidentally, the launched pump power at which these crossings occur should be independent of the inclusion of amplified spontaneous emission in the calculations, since ASE depends – to first order – on the total inversion in the waveguide. For equal gain, this total inversion has to be equal for the two waveguides involved.

It is clear from figure 5.5 that for any given launched pump power, a properly chosen nonzero Yb^{3+} concentration will increase the maximum gain achievable in the waveguide over the one without inclusion of Yb^{3+} . Although the curve given for an Yb^{3+} concentration of $3.35 \cdot 10^{20} \text{ cm}^{-3}$ (open squares) will eventually run below the curve for zero Yb^{3+} concentration (solid squares) for launched pump powers of above 200 mW, decreasing the Yb^{3+} concentration further will shift the crossing towards even higher pump powers. Only in the academic case of infinite pump power/infinite waveguide length, the maximum gain cannot be increased by Yb^{3+} codoping. However, attention must be given to the fact that the energy transfer coefficients C_{ij} generally depend on concentration in this regime, and simple extrapolation cannot be applied. For all practical purposes, the launched pump power is limited to values of below 1 W, and Yb^{3+} codoping will always increase the maximum gain that can be achieved in a given waveguide. However, at high pump power this increase will be

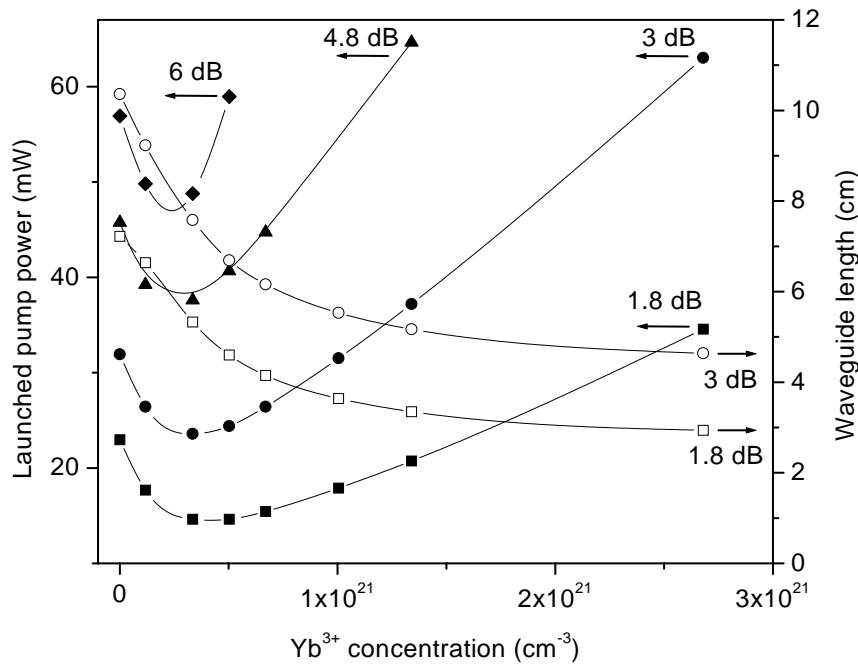


FIGURE 5.6: Calculation of the pump power that has to be launched into the waveguide to reach a gain of 1.8 dB, 3 dB, 4.8 dB, and 6 dB in a waveguide whose length has been optimised, as a function of Yb^{3+} concentration. Also plotted is the dependence of the waveguide length (optimised for maximum gain) on Yb^{3+} concentration for gains of 1.8 dB and 3 dB. The drawn lines are guides to the eye.

small.

Finally we would like to address the relation between Yb^{3+} concentration and launched pump power necessary to achieve a fixed gain (again for optimised length). This corresponds to a horizontal cut through figure 5.5 and has been plotted in figure 5.6 for clarity. The solid symbols give the pump power that has to be launched into the waveguide to reach a certain gain, as a function of the Yb^{3+} concentration in the waveguide. It can be discerned that the launched pump power is minimal for a finite Yb^{3+} concentration. This minimum moves to lower values of the Yb^{3+} concentration as the gain augments. This behaviour follows directly from the argument made above about the concentration dependence of the maximum gain. It is once again a consequence of the tradeoff between excitation efficiency of the Er^{3+} via Yb^{3+} and the increased absorption in the waveguide caused by Yb^{3+} . If too high an Yb^{3+} concentration is chosen, the pump power needed to achieve a certain gain level rapidly increases.

Included in figure 5.6 are two curves that show the development of waveguide length, at which a gain of 1.8 dB and 3 dB is achieved, as a function of Yb^{3+} concentration

(open symbols). The waveguide length is a decreasing function of Yb^{3+} concentration, which reflects the increased absorption in the waveguide due to Yb^{3+} . Reducing the length of a waveguide amplifier by Yb^{3+} codoping may hold interest from a device design point of view, but it is clear that the penalty paid in pump power for a small reduction of waveguide length is large beyond the Yb^{3+} concentration at which the required pump power has its minimum (cf. figure 5.6). This is because the shorter waveguide length has to be offset by gain in the tails of the mode, and therefore an oversupply of power in the central part of the waveguide. In materials in which excited state absorption of the pump radiation plays a role, this might actually have deleterious effects.

5.4 Summary

We have calculated the signal output from Al_2O_3 waveguides doped with Er^{3+} and Yb^{3+} with a rate equation propagation model. The behaviour of the signal gain at 1530 nm was studied for an Er^{3+} concentration of $3.35 \cdot 10^{20} \text{ cm}^{-3}$ and various Yb^{3+} concentrations between $3.35 \cdot 10^{20} \text{ cm}^{-3}$ and $26.8 \cdot 10^{20} \text{ cm}^{-3}$, and compared to that of a waveguide without Yb^{3+} .

We have investigated the relationship between gain and Yb^{3+} concentration, launched pump power, and waveguide length. In waveguides of fixed length, Yb^{3+} codoping can lower the gain threshold and increase the gain for launched pump powers around the threshold pump power. For pump powers above the point at which the direct excitation of Er^{3+} becomes as probable as its excitation via Yb^{3+} , the increase in gain over a waveguide doped only with Er^{3+} is small. The maximum gain that can be achieved in a waveguide amplifier for a fixed pump power can be increased by codoping with Yb^{3+} , if the concentration is chosen correctly. For each launched pump power, an optimised Yb^{3+} concentration can be determined. In the case where a certain gain has to be achieved, codoping with the right amount of Yb^{3+} substantially reduces the necessary pump power. However, we have found that doping the waveguides with high concentrations of Yb^{3+} always has detrimental effects on gain or pump power necessary to achieve a certain gain. This is due to an increased absorption of the pump and decreased absorbed photon conversion efficiency at high Yb^{3+} concentration. Where these effects set in depends on the exact values of the material parameters and the waveguide geometry.

In conclusion, our simulations have shown the need for careful optimisation of the Yb^{3+} concentration in $\text{Er}^{3+}/\text{Yb}^{3+}$ codoped waveguide amplifiers where pump and signal are copropagating. In applications using very high launched pump powers, it might be of advantage to grade the Yb^{3+} concentration along the length of the waveguide, or to only include Yb^{3+} at the end of the waveguide, where the pump power is low enough so that Yb^{3+} increases the population inversion substantially.

Chapter **SIX**

Energy transfer to Er^{3+} in Ag ion-exchanged glass

THE PHOTOLUMINESCENCE OF Er^{3+} IN BOROSILICATE GLASS IS STRONGLY ENHANCED BY THE PRESENCE OF SILVER. SAMPLES PREPARED BY A COMBINATION OF ERBIUM ION IMPLANTATION AND $\text{Na}^+ \longleftrightarrow \text{Ag}^+$ ION EXCHANGE SHOW AN INCREASE OF THE Er^{3+} EXCITATION EFFICIENCY OF UP TO A FACTOR 70 WHEN EXCITED AT 488 nm. EXCITATION OF Er^{3+} IS POSSIBLE OVER A BROAD WAVELENGTH RANGE IN THE NEAR ULTRAVIOLET AND VISIBLE. OUR DATA SUGGEST THAT ABSORPTION OF LIGHT OCCURS AT A SILVER ION/ATOM PAIR OR SIMILAR DEFECT, FOLLOWED BY ENERGY TRANSFER TO Er^{3+} . WE CAN EXCLUDE THAT SILVER NANOCRYSTALS ARE PART OF THE DOMINANT EXCITATION MECHANISM, NEITHER VIA LOCAL FIELD ENHANCEMENT EFFECTS DUE TO THEIR SURFACE PLASMON RESONANCE NOR VIA ABSORPTION AND SUBSEQUENT ENERGY TRANSFER TO Er^{3+} .

The small absorption cross sections of rare earth ions such as erbium or neodymium have spawned numerous attempts to increase the ions' excitation efficiency. Most concepts rely on energy transfer from a species with a large absorption cross section to the rare earth ion in question. In the specific case of erbium, codoping with ytterbium (although itself a rare earth ion, it has a reasonably high absorption cross section at 980 nm) has found its way into application in lasers and optical amplifiers for 1540 nm light (Laporta et al., 1991; Barbier et al., 1997), and broad-band sensitisation in the visible via organic complexes (Slooff et al., 1998) and silicon nanocrystals (Fujii et al., 1997) has been demonstrated.

In the framework of this research we have turned our attention to photoluminescence enhancement effects that silver might have on Er^{3+} in oxide glass. Silver can be introduced easily to concentrations of several atomic percent into glasses via an ion exchange process (Ramaswamy and Srivastava, 1988), interchanging network modifiers of the glass like sodium or potassium and silver ions. This is a standard process to fabricate waveguides for integrated optics. Several absorption and emission bands in the visible and near ultraviolet related to silver have been observed in glasses (Messaoui et al., 1992; Meijerink et al., 1993), opening the possibility of energy transfer towards Er^{3+} .

Doping glasses with silver however gains an additional dimension from the fact that nanometer-sized crystals can be precipitated. Besides other interesting optical properties, such glass/metal nanocrystal composites exhibit large optical nonlinearities caused by enhanced local electric fields around the nanocrystals (Flytzanis et al., 1991). Some evidence for the effect of this local field on the emission of Eu^{3+} ions has also been reported (Hayakawa et al., 1999a,b).

In the following we will present investigations of borosilicate glass doped with erbium by ion implantation and with silver by ion exchange in the light of the above issues. By adjusting the doping procedure we are able to fabricate samples with a high concentration of dissolved silver and little to no silver nanocrystals, and samples where a considerable amount (but not all) of the silver aggregates into crystallites. We observe a broad excitation band of the photoluminescence of Er^{3+} in the visible and near ultraviolet, with luminescence enhancements up to a factor of 70 at a pump wavelength of 488 nm. From the spectral dependence and a reduced excitation efficiency in the presence of silver nanocrystals we conclude that the excitation efficiency of Er^{3+} is increased by an energy transfer from Ag^+ related centres rather than under the influence of silver nanocrystals.

6.1 Sample preparation and characterisation techniques

The borosilicate glass substrates used for these experiments were 1 mm thick Schott BK7 wafers. Silver was introduced into the samples by a $\text{Na}^+ \longleftrightarrow \text{Ag}^+$ ion exchange in a salt melt containing 5 mol% AgNO_3 and 95 mol% NaNO_3 . The samples were left

in the melt for 7 min at 310°C . Erbium was implanted at an energy of 925 keV to a fluence of $3.1 \cdot 10^{15} \text{ cm}^{-2}$ into the glass, which was kept at liquid nitrogen temperature. Two samples were prepared combining these two doping techniques. One was first implanted with erbium and subsequently ion-exchanged, while the other underwent the ion exchange first, and the resulting Ag^+ doped glass was then implanted with erbium. The bombardment of Ag^+ doped glass with heavy ions, as in the latter case, has been shown to lead to the formation of silver nanocrystals (Peters et al., 2000, see chapter 7). For reference purposes, another glass sample was implanted with erbium under the same conditions, but did not undergo ion exchange. All samples were annealed in vacuum for 30 min at 350°C .

Normal-incidence transmission spectra were measured on a dual beam photospectrometer in the wavelength range between 300 nm and 2000 nm. An untreated glass slide was placed in the reference beam to only measure changes in the transmission spectrum caused by the various treatments of the samples. The Er^{3+} ions were excited with the lines of an Ar^+ laser, their photoluminescence collected, dispersed with a 96 cm monochromator, and detected with a liquid nitrogen-cooled germanium detector. Photoluminescence excitation spectra were measured using a xenon lamp as excitation source in combination with a monochromator with 20 nm spectral resolution for wavelength selection.

6.2 Photoluminescence enhancement

The main difference between the samples prepared by ion exchange and ion implantation is the presence or absence of silver in ionic or metallic form. From Rutherford Backscattering Spectrometry we obtain a silver concentration of 2.2 at.% in the sample first ion-exchanged then erbium implanted, and around 3 at.% for the sample implanted with erbium before the ion exchange. These values are approximately constant up to a depth of around 600 nm. For comparison, the erbium range for our implantations amounts to 250 nm. We attribute the difference in Ag concentration between the two samples to variations in the diffusivity of Ag^+ ions caused by damage from the ion irradiation in the glass. While silver is present predominantly as Ag^+ ions in the glass implanted with erbium before ion exchange, irradiation with heavy ions after ion exchange leads to the agglomeration of a considerable amount of the silver ions in metallic nanocrystals (Peters et al., 2000, see chapter 7). Figure 6.1 compares the absorbance induced by the preparation of the two samples doped with silver and erbium. The distinctive band peaking at 420 nm observed for the sample ion-implanted after ion exchange is caused by the surface plasmon resonance in the silver nanocrystals. The fraction of silver agglomerated in nanocrystals estimated from the strength of the absorption is around 30%. The sample that was ion-exchanged after erbium implantation shows an increased absorbance, rising towards shorter wavelengths, whose origin might be related to the ion exchange. A similarly shaped, yet slightly lower, structure underlies the surface plasmon band.

In figure 6.2 we have plotted the emission spectra of the three samples (including

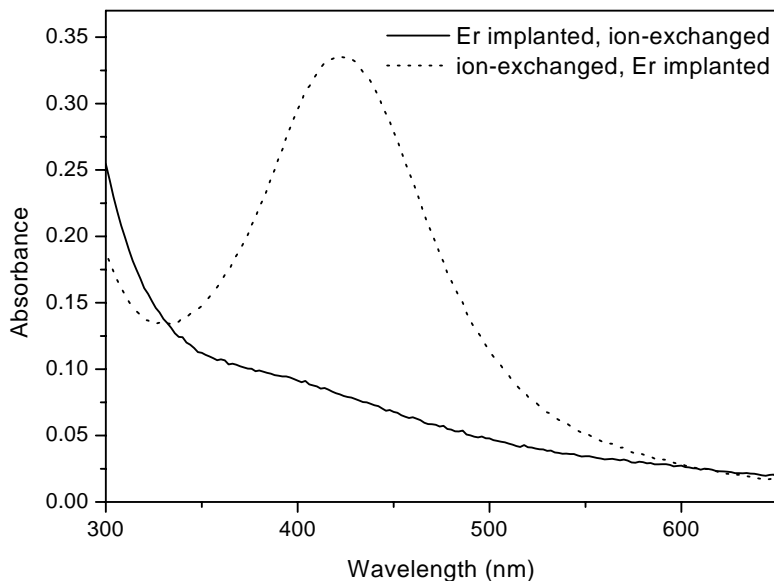


FIGURE 6.1: Absorbance of the samples doped with erbium and silver. The band around 420 nm is caused by the plasmon resonance of silver nanocrystals formed during erbium implantation into silver-containing glass. The data were measured relative to an untreated reference glass slide.

the reference sample containing no Ag) between 1400 nm and 1700 nm. The emission lines are caused by transitions between the first excited state and the ground state of Er^{3+} . They are identical for the three samples. While the luminescence of the sample without silver has been excited with 488 nm radiation into the $^4\text{F}_{7/2}$ state of Er^{3+} , the samples containing silver show strong photoluminescence even when excited with 476 nm light, a wavelength at which Er^{3+} does not absorb. This is illustrated by the excitation spectrum for the sample doped with only erbium in figure 6.3 (a), measured using the lines from the Ar^+ laser. Only when excited at 515 nm, 488 nm and 360 nm, significant emission from Er^{3+} around 1540 nm is observed. In contrast, Er^{3+} can be excited over a wide spectral range in both samples containing silver, extending from the near ultraviolet to the red, as is evident from figure 6.3 (b). Note the difference in the intensity scale between figures 6.3 (a) and (b), calibrated by photoluminescence intensity measurements excited with the 488 nm line of the Ar^+ laser. The photoluminescence lifetime measured at 1538 nm is 2.5 ms for the sample doped only with erbium, and 1.0 ms for the samples doped with erbium and silver.

The shape of the excitation spectrum is identical for both the sample that was ion-exchanged after erbium implantation and the sample implanted with erbium after ion exchange. The intensity of the Er^{3+} emission is however higher for the sample

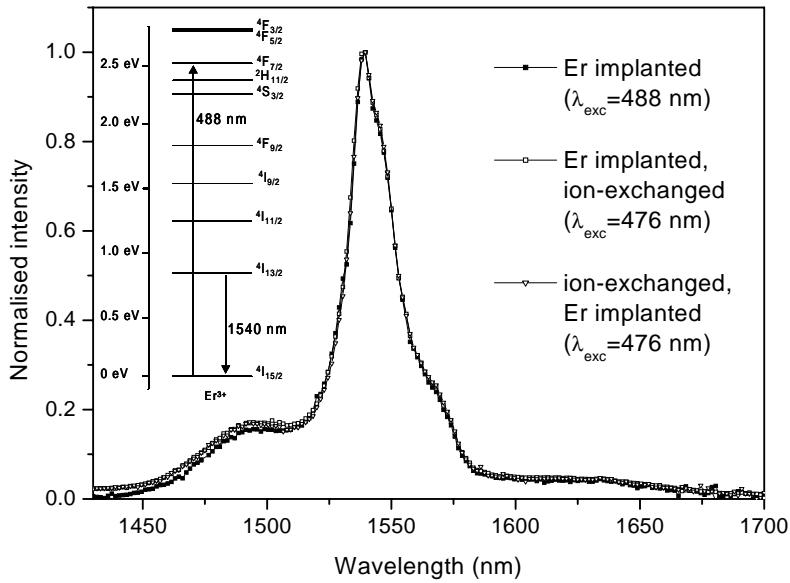


FIGURE 6.2: Spectra of Er^{3+} emission in borosilicate glass doped with silver by an ion exchange process (open symbols). Note that the photoluminescence was excited at a wavelength which cannot be absorbed directly by Er^{3+} . The emission spectra are identical to the one obtained for Er^{3+} in glass without silver when excited to its ${}^4\text{F}_{7/2}$ state (solid squares). The inset shows the energy level spectrum of Er^{3+} .

that underwent the ion exchange after implantation of erbium. This is the sample with both a higher silver concentration and more silver dispersed in ionic form in the glass matrix, i.e. not aggregated to form silver nanocrystals. Since the nanocrystals form predominantly in the region of the glass around the range of the implanted erbium ions, the concentration of silver ions in the vicinity of erbium is reduced by their precipitation. The emission intensity at 1540 nm is enhanced by a factor of 20 and 70 for the samples ion-exchanged before and after implantation of erbium, respectively, when they are excited with 488 nm radiation. Another four-fold increase of the Er^{3+} luminescence is achieved by reducing the pump wavelength from 488 nm to 360 nm.

The origin of the increase in emission intensity may be inferred from the excitation spectra and the absorbance induced by the processing of the different samples, figures 6.3 and 6.1. Several conclusions can be drawn from these plots: in contrast to the work by Hayakawa and coworkers (Hayakawa et al., 1999a,b), who investigated the luminescence enhancement of Eu^{3+} in glasses containing silver nanoparticles, we can exclude field enhancement effects due to the surface plasmon resonance of silver nanoparticles as the dominant mechanism responsible for the increased luminescence from our samples. Such a process does not change the position of the energy levels and

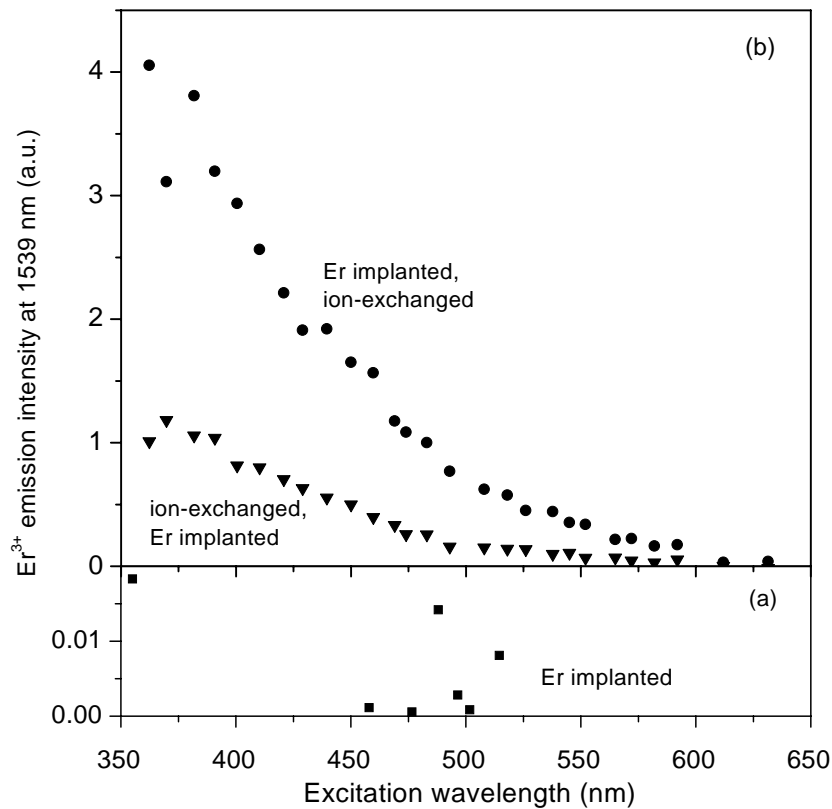


FIGURE 6.3: Photoluminescence intensity at 1539 nm as a function of excitation wavelength for three different samples: (a) borosilicate glass doped with erbium only; (b) erbium and silver doped borosilicate glass.

therefore the shape of the excitation spectrum of Er^{3+} , as the local field only changes the absorption probability at wavelengths where there is a nonzero absorption cross section. This stands in clear contrast to the observations presented in figure 6.3. Furthermore we can also exclude energy transfer from silver nanoparticles to erbium ions. The excitation spectrum does not overlay the surface plasmon absorption, which therefore cannot be the initial step in the excitation of Er^{3+} . Also the fact that the sample containing silver nanocrystals exhibits a lower excitation efficiency of Er^{3+} luminescence than the one containing no nanocrystals, points in this direction.

The spectral shape of the excitation spectra of the samples doped with silver does not match the spectrum of the absorption we believe to be induced by the ion exchange shown in figure 6.1. The absorbance spectrum does not approach zero at 600 nm, as is clear from figure 6.1, while Er^{3+} can hardly be excited at that wavelength (cf.

figure 6.3). However, it can be argued that a much weaker absorption than the one observed in the sample ion-exchanged after erbium implantation is sufficient to obtain the photoluminescence enhancement seen for that sample. From considerations of the detection efficiency of the photoluminescence measurement system, an absorbance lower by five orders of magnitude would explain the results reported in figure 6.3 for a conversion efficiency from absorbed pump photon to emitted photoluminescence photon of 1. Even for quantum efficiencies down to 10^{-4} , the necessary absorbance would be invisible in normal-incidence transmission measurements on ion-exchanged waveguides. It therefore seems likely that the absorption that constitutes the initial step in the excitation of Er^{3+} is completely hidden in figure 6.1 by a second, stronger absorption not linked to Er^{3+} excitation. A similar argument can be given comparing the absorbances due to Er^{3+} at 488 nm and the absorbance shown in figure 6.1. With an estimate of the former from the absorption cross section obtained for Er^{3+} in Al_2O_3 in chapter 4 we arrive at a ratio of $2.5 \cdot 10^{-4}$. An increase in photoluminescence output of two orders of magnitude as observed (cf. figure 6.3) can then be explained by an absorbance amounting to only 10% of the one observed, when assuming an energy transfer efficiency of the order of 10%.

The shape of the silver-related band, from where energy transfer towards Er^{3+} originates, can only be deduced from the excitation spectra. Several authors (Mesnaoui et al., 1992; Villegas et al., 1996) have observed an absorption band in the spectral region between 300 nm and 450 nm in glasses containing high concentrations of silver, and attributed it to pairs of silver ions/atoms. Similar centres might be at the origin of the energy transfer to Er^{3+} . Assuming a concentration of ion pairs of 0.1 at.% as the absorbing species (as obtained from a statistical formation process with the concentration of ion pairs proportional to the square of the concentration of the solitary ions), we estimate the absorption cross section of the pairs to have a value between 10^{-20} cm^2 and 10^{-16} cm^2 , depending on the quantum efficiency assumed. These numbers are not unreasonable for metal ions.

The absorption of Ag^+ ions in glasses is generally found at wavelengths much shorter than the range covered by our measurements, and Ag^+ is therefore unlikely to take part in the excitation mechanism of Er^{3+} reported here. Unlikely for similar reasons is that the excitation takes place via the glass band edge, shifted to longer wavelengths owing to the introduction of Ag^+ into the glass. This displacement is usually small for silver concentrations comparable to the ones in our samples (Mesnaoui et al., 1992; Borsella et al., 2000).

Finally, let us mention that the enhancement of Er^{3+} emission by codoping with silver is not restricted to doping by ion exchange. Samples into which silver was introduced by ion implantation also showed the broad excitation band for the photoluminescence of Er^{3+} .

6.3 Summary

The photoluminescence from Er^{3+} around 1540 nm is strongly enhanced in borosilicate glass codoped with silver. An excitation efficiency as high as 70 times the one of Er^{3+} in the same glass without silver has been obtained under excitation at 488 nm. By exciting at 360 nm, another factor of 4 in photoluminescence intensity is gained. The excitation spectrum in the visible is broad-band and does not reproduce the erbium intra-4f absorption lines. There are indications that the excitation takes place via absorption at a defect related to a pair of silver ions/atoms and energy transfer towards Er^{3+} . Furthermore we can conclude that silver nanocrystals do not play a role in the enhancement of the Er^{3+} photoluminescence in our samples, neither as origin of an enhanced local field nor as absorption centres for a subsequent energy transfer.

Part II

Silver nanocrystals in silicate glass

Chapter SEVEN

Formation mechanism of silver nanocrystals made by ion irradiation of $\text{Na}^+ \longleftrightarrow \text{Ag}^+$ ion-exchanged sodalime glass

SODALIME SILICATE GLASS SURFACE LAYERS WERE DOPED WITH UP TO 7.0 AT.% Ag^+ IONS BY ION EXCHANGE IN AN $\text{AgNO}_3/\text{NaNO}_3$ SOLUTION AT 330 – 355 °C. ION IRRADIATION WITH EITHER 400 OR 500 KEV HE, 1 MEV NE, OR 2 MEV XE WAS THEN USED TO INDUCE THE GROWTH OF METALLIC NANOCRYSTALS IN THE ION-EXCHANGED REGION. THE ION FLUENCES RANGED FROM $1.3 \cdot 10^{14}$ IONS/ cm^2 TO $1.1 \cdot 10^{17}$ IONS/ cm^2 . AFTER IRRADIATION, X-RAY AND ELECTRON DIFFRACTION SHOW SMALL AG NANOCRYSTALS WITH A BROAD SIZE DISTRIBUTION, UP TO A DIAMETER OF 10 – 15 NM. OPTICAL TRANSMISSION MEASUREMENTS SHOW THE CHARACTERISTIC SURFACE PLASMON RESONANCE OF METALLIC AG NANOCRYSTALS AROUND 420 NM. THE ABSORPTION RESONANCE SHARPENS AND INTENSIFIES WITH INCREASING ION IRRADIATION FLUENCE, INDICATING THAT BOTH NANOCRYSTAL SIZE AND VOLUME FRACTION INCREASE WITH IRRADIATION FLUENCE. DEPENDING ON ION FLUENCE, UP TO $\sim 10\%$ OF THE ION-EXCHANGED Ag^+ IONS IS INCORPORATED IN NANOCRYSTALS. FROM A SYSTEMATIC COMPARISON OF THE DEGREE OF NANOCRYSTAL FORMATION AS A FUNCTION OF ION SPECIES, FLUENCE AND ENERGY, IT IS CONCLUDED THAT NANOCRYSTAL FORMATION IS MAINLY CAUSED BY THE ATOMIC DISPLACEMENT ENERGY LOSS COMPONENT OF THE INCOMING BEAM; THE ELECTRONIC ENERGY DEPOSITION COMPONENT IS LESS EFFICIENT.

The $\text{Na}^+ \longleftrightarrow \text{Ag}^+$ ion exchange technique is a well-established method to dope surface layers of sodalime glass with Ag^+ ions (Ramaswamy and Srivastava, 1988). Depending on exchange time and temperature, Ag^+ concentrations of several atomic percent, extending to a depth of several microns, can be achieved. Such Ag^+ doped layers can be used as low-loss planar optical waveguides. It has been shown before that ion irradiation of these ion-exchanged waveguides with He ions causes the formation and growth of silver nanocrystals (Caccavale et al., 1995; De Marchi et al., 1996). Metallic nanocrystals display strong nonlinear optical properties (Hache et al., 1986; Arnold et al., 1996), and therefore nanocrystal doped waveguides have potential for application in all optical switching components. As ion irradiation is a technique that can be applied locally, e.g. on a small lithographically defined area, the combination of ion exchange to fabricate waveguides, and ion irradiation to locally fabricate a nonlinear region, seems promising for the fabrication of a planar waveguide switch.

Before pursuing such applications, it is first necessary to understand and control the details of the nanocrystal formation process, and to answer questions such as: how does the nanocrystal growth depend on ion irradiation conditions like ion energy, ion species, atomic displacement energy loss or electronic energy loss; what is the nanocrystal size distribution, and what determines the nucleation and growth kinetics?

In this chapter we use 400 and 500 keV He, 1 MeV Ne, and 2 MeV Xe ion irradiation of $\text{Na}^+ \longleftrightarrow \text{Ag}^+$ ion-exchanged sodalime glass at various fluences, in combination with X-ray diffraction (XRD), electron microscopy, and optical extinction measurements to answer some of these questions. It is found that both the Ag nanocrystal size and volume fraction increase with irradiation fluence. For the fluence range studied, up to $\sim 10\%$ of the ion-exchanged Ag is incorporated in nanocrystals. Characteristic differences are found between the effect of atomic displacement energy loss on the one hand, and electronic energy loss on the other hand, on the growth of Ag nanocrystals.

7.1 Sample preparation and characterisation techniques

Sodalime silicate glass samples of 0.6 mm thickness were ultrasonically cleaned using trichloroethylene, acetone, and propanol. Next, the samples were preheated and immersed in a molten solution of 5 mol% AgNO_3 in NaNO_3 to induce $\text{Na}^+ \longleftrightarrow \text{Ag}^+$ ion exchange. Temperatures between 330 °C and 355 °C and exchange times between 10 and 20 min were used. After ion exchange a slight yellow discoloration was observed.

The ion-exchanged samples were mounted on a copper block using vacuum grease to provide good thermal contact, and irradiated with either 400 keV or 500 keV He, 1 MeV Ne, or 2 MeV Xe ions. Irradiation was performed at room temperature at a base pressure of $6 \cdot 10^{-7}$ mbar. The implantation ranges were all between 1 and 2 μm , as calculated with TRIM, a Monte Carlo simulation programme (Ziegler et al., 1985). The fluences were varied between $1.3 \cdot 10^{14}$ ions/cm² and $1.1 \cdot 10^{17}$ ions/cm². The

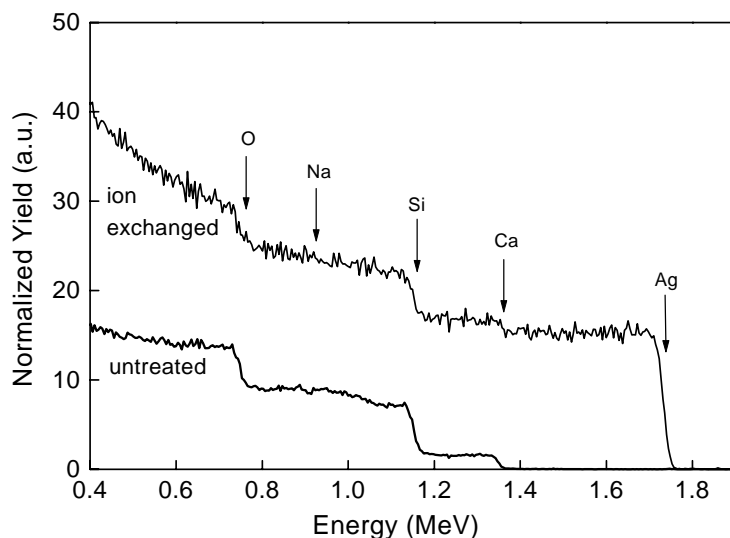


FIGURE 7.1: RBS spectrum of an ion-exchanged sample and an untreated reference sample taken with a 2.0 MeV He beam at a scattering angle of 165° . The ion-exchanged sample was treated in a 5 mol% AgNO_3 solution in NaNO_3 for 20 min at 355°C . The surface energies for the constituents of the glass are indicated.

irradiation flux was kept below $7 \cdot 10^{12}$ ions/cm²/s in order to prevent beam heating effects.

Rutherford Backscattering Spectrometry (RBS) was performed using a 2 MeV He beam and a scattering angle of 165° , in order to determine the composition of the sodalime glass before and after the ion exchange. XRD spectra were taken with a Cu $K\alpha_1$ beam ($\lambda = 0.154$ nm) using a PDS 120 Enraf-Nonius X-ray diffractometer set in powder diffraction geometry. Cross-sectional transmission electron microscopy (TEM) images were taken using a 300 keV electron beam from a Philips CM 30T electron microscope. Electron diffraction micrographs were also obtained. Optical transmission measurements were performed using the transmission setting of a spectroscopic ellipsometer with the incident beam perpendicular to the sample surface. The wavelength was scanned from 250 nm to 1100 nm in 2 nm steps.

7.2 Nanocrystal characterisation

Figure 7.1 shows RBS spectra of an untreated sodalime glass sample and an ion-exchanged sample (355°C , 20 min). The spectrum of the untreated sample shows the leading edges of O, Na, Si, and Ca. The glass composition derived from the spectrum is: 25 at.% Si, 60 at.% O, 12 at.% Na, 3 at.% Ca, and possibly small concentrations

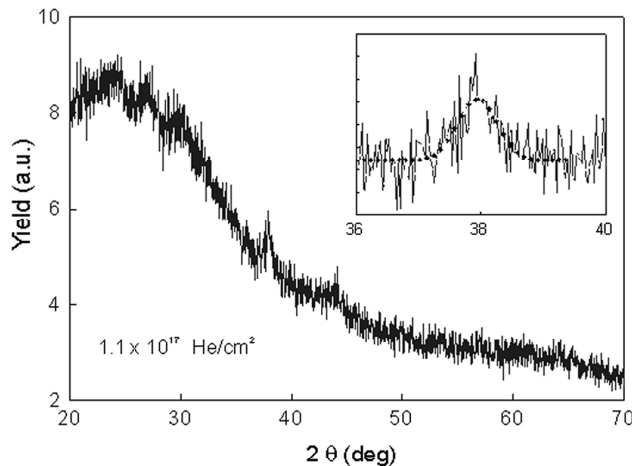


FIGURE 7.2: X-ray diffraction spectrum of an ion-exchanged sample, irradiated with $1.1 \cdot 10^{17} \text{ He/cm}^2$ at 500 keV. Ion exchange parameters were identical to those for the sample of figure 7.1. The spectrum was taken with a beam of $\text{Cu K}\alpha_1$ radiation ($\lambda = 0.154 \text{ nm}$). The inset shows an enlargement of the Ag (111) peak after background subtraction, together with a fit from which an average nanocrystal size of $\sim 13 \text{ nm}$ was estimated.

of other constituents that are below the detection limit of RBS. The spectrum of the ion-exchanged sample shows a large Ag contribution. The Ag concentration at the surface derived from this spectrum is $4.1 \cdot 10^{21} \text{ Ag/cm}^3$, corresponding to 7.0 at.%. Taking into account the variation in energy loss and scattering cross section with depth for RBS, it is concluded that the Ag concentration gradually decreases with depth. The maximum Ag diffusion depth is estimated to be well beyond $4 \mu\text{m}$.

Fig 7.2 shows the XRD spectrum of an ion-exchanged sample irradiated with 500 keV He to a fluence of $1.1 \cdot 10^{17} \text{ ions/cm}^2$. The broad band peaked around $20 - 25^\circ$ is typical for sodalime glass. The peak at $2\theta = 38^\circ$ is not observed in the spectrum of an ion-exchanged, non-irradiated sample (not shown). The inset in figure 7.2 shows an enlargement of this peak after a linear background subtraction. A Gaussian fit through the data is also shown. It peaks at $2\theta = 37.9^\circ$ and has a full-width at half maximum of 0.64° . This peak can be attributed to diffraction from Ag (111) planes, with a lattice spacing of 2.36 \AA . From the width, a Ag nanocrystal diameter can be estimated: it amounts to $\sim 13 \text{ nm}$. Note that a small peak is also observed in the spectrum at $2\theta = 44^\circ$, which can be attributed to scattering from Ag (200) planes.

Figure 7.3 shows a cross-sectional dark-field TEM image of the same sample as in figure 7.2. The image was taken at a depth of $\sim 1 \mu\text{m}$ using diffraction from the Ag (111) planes. The inset in figure 7.3 shows an electron diffraction pattern taken from

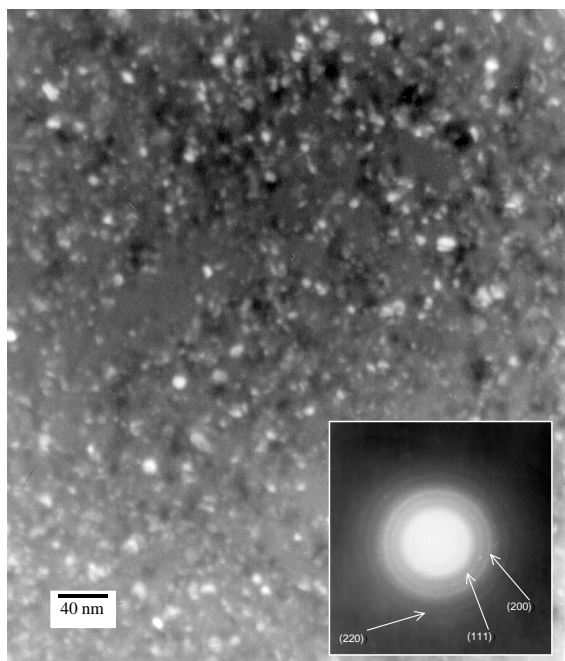


FIGURE 7.3: Cross-sectional TEM dark field image for the Ag (111) orientation, for the same sample as in figure 7.2, taken at a depth of $1\ \mu\text{m}$ from the sample surface. The inset shows the diffraction micrograph in which the rings for Ag (111), (200), and (220) planes are visible.

the same region. The TEM image clearly shows the presence of spherical nanocrystals with a maximum diameter of $\sim 10 - 15\ \text{nm}$. The majority of the nanocrystals have much smaller radii, down to at least $3.5\ \text{nm}$, the image resolution. The diffraction pattern in the inset of figure 7.3 shows three clear rings, which can be assigned to Ag (111), (200), and (220) planes. No texture or preferential orientation of the nanocrystals is observed. From similar cross-sectional TEM images taken at different distances from the sample surface (not shown), one can observe the density of nanocrystals to decrease with depth. No Ag nanocrystals are found at a depth of $4\ \mu\text{m}$, well beyond the range of $500\ \text{keV He}$.

Figure 7.4 (a) shows optical transmission spectra of ion-exchanged samples irradiated with $400\ \text{keV He}$ to fluences of $1.1 \cdot 10^{16}$, $2.6 \cdot 10^{16}$, and $8.1 \cdot 10^{16}\ \text{ions/cm}^2$, as well as the spectra of a sodalime glass reference sample (indicated by 'r') and an ion-exchanged, non-irradiated sample (indicated by '0'). All transmission spectra display a transmission cut-off below $300\ \text{nm}$ due to the absorption of the glass substrate. For the untreated glass sample a transmission of 88% is observed over the full spectral range from $310\ \text{nm}$ to $1100\ \text{nm}$. As can be seen in figure 7.4 (a), ion exchange

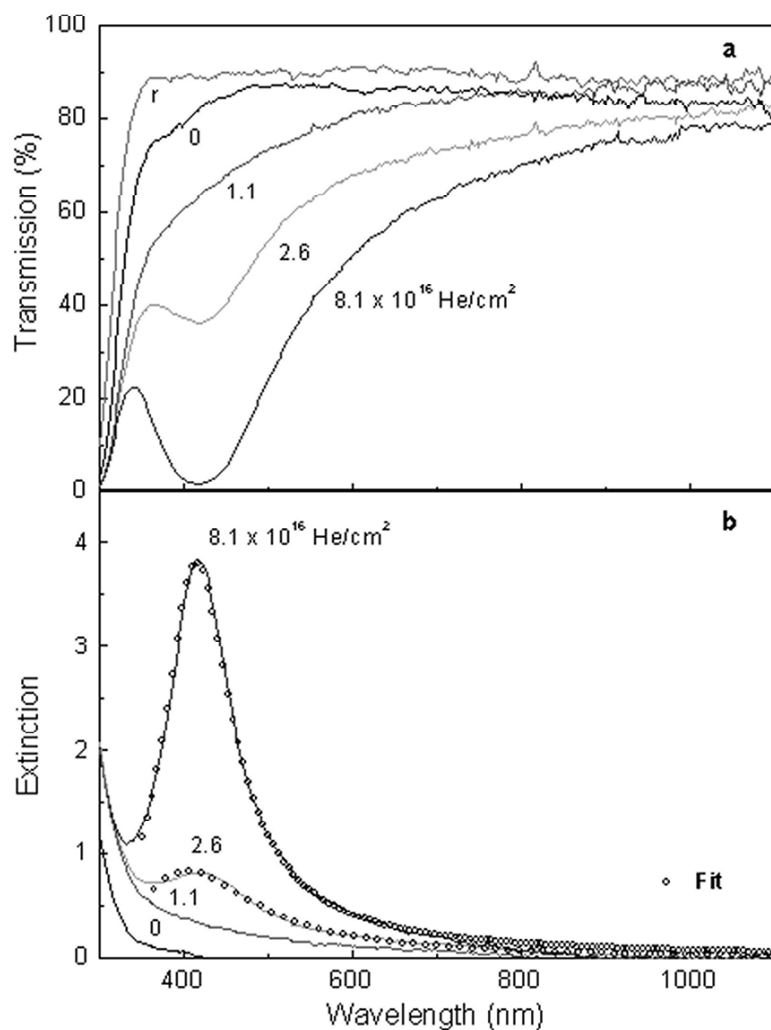


FIGURE 7.4: (a) Optical transmission spectra of ion exchanged samples irradiated with 400 keV He to various fluences. 'r' indicates the spectrum of an untreated reference sample, '0' the spectrum of an ion-exchanged, non-irradiated sample. (b) Absorbance spectra of the samples in (a), obtained from the transmission spectra as explained in the text. The open circles represent fits using Mie theory (equation (7.1)), from which the nanocrystal diameter and volume of metallic Ag per unit area were estimated.

causes a slight decrease in transmission over the entire spectral range. The subsequent ion irradiation causes a further decrease in transmission over the whole wavelength range from 300 nm to 1100 nm. For increasing irradiation fluences, a transmission dip centred at ~ 420 nm evolves. For the highest irradiation fluence the minimum transmission at $\lambda = 418$ nm is only 2%.

Figure 7.4 (b) shows absorbance spectra obtained from the data in figure 7.4 (a), using the transmission of the untreated glass sample at $\lambda = 1000$ nm as a reference. These absorbance spectra $A(\lambda)$ can be compared to the well-known Mie theory for the absorbance caused by metallic nanoparticles embedded in a dielectric medium (Mie, 1908). For nanocrystal sizes below 20 nm, contributions of scattering to the absorbance are negligible for visible light, and only the electric dipole term in the Mie expansion for the absorption has to be taken into account (Arnold and Borders, 1977),

$$A(\lambda) = 9f\epsilon_m^{3/2} \frac{\omega}{c} \frac{\epsilon_2}{\left((\epsilon_1 + 2\epsilon_m)^2 + \epsilon_2^2\right)} \quad (7.1)$$

with

$$\begin{aligned} \epsilon_1(\omega) &= \epsilon'_1(\omega) + 1 - \frac{\omega_p^2}{\omega^2 + \omega_c^2} \\ \epsilon_2(\omega) &= \epsilon'_2(\omega) + \frac{\omega_c}{\omega} \frac{\omega_p^2}{\omega^2 + \omega_c^2} \end{aligned}$$

where

$$\omega_c = \frac{v_f}{l} + \frac{2v_f}{d}.$$

c represents the speed of light in vacuum, ϵ_m the dielectric constant of the (transparent) matrix in which the Ag clusters are embedded, and f the volume of metallic Ag in the dielectric/metal composite per unit area¹. ϵ_1 and ϵ_2 are the real and imaginary parts of the dielectric function of the nanocrystal, respectively, and ϵ'_1 and ϵ'_2 the real and imaginary parts of the dielectric function of bulk Ag due to interband transitions (using data from Johnson and Christy (1972)). ω_p is the plasma frequency of silver, v_f the Fermi velocity of electrons in bulk Ag, l the electron mean free path in bulk silver and d the diameter of the Ag nanocrystals.

Fitting equation (7.1) to the data for the two highest fluences in figure 7.4 (b), using literature values (Ashcroft and Mermin, 1976) of $v_f = 1.38 \cdot 10^6$ m/s, $l = 5.7 \cdot 10^{-8}$ m, and $\omega_p = 1.37 \cdot 10^{16}$ s⁻¹, and taking f , d , and ϵ_m as adjustable parameters, yields the open circle curves in figure 7.4 (b): the fits show excellent agreement with the experimental data. Note that we used a single nanocrystal diameter d in the fitting procedure. Fits obtained using a discrete nanocrystal size distribution indicate that the nanocrystal diameter d is peaked around its mean value, with a standard deviation of around 1 nm. Taking a larger standard deviation in d increases the error of the fit considerably. Therefore we believe the use of a single nanocrystal diameter to be

¹In accounts of Mie theory, usually a similar expression as equation (7.1) is given for the absorption coefficient, with f representing the volume fraction of metal in the composite.

TABLE 7.1: Nanocrystal diameter d , volume of metallic Ag per unit area f , and fraction of metallic Ag, obtained from fits to the absorbance data for 400 keV He, 1 MeV Ne, and 2 MeV Xe irradiation using equation (7.1). The values between brackets were obtained from fits after a smooth background subtraction from the absorbance curves had been performed.

| Implanted ion | Irradiation fluence (ions/cm ²) | Diameter d (nm) | f (nm) | Fraction of metallic Ag (at.%) |
|---------------|--|----------------------|-------------|-----------------------------------|
| 400 keV He | $2.6 \cdot 10^{16}$ | 1.3 (1.6) | 6.0 (3.4) | 0.31 (0.18) |
| | $8.1 \cdot 10^{16}$ | 2.2 (2.6) | 17.1 (13.5) | 0.90 (0.72) |
| 1 MeV Ne | $1.7 \cdot 10^{15}$ | 1.3 (-) | 3.7 (-) | 0.28 (-) |
| | $3.9 \cdot 10^{15}$ | 1.4 (2.1) | 4.8 (1.4) | 0.35 (0.09) |
| | $5.4 \cdot 10^{15}$ | 1.4 (2.3) | 5.2 (1.4) | 0.38 (0.09) |
| 2 MeV Xe | $5.0 \cdot 10^{14}$ | 1.3 (2.0) | 5.0 (0.9) | 0.21 (0.09) |
| | $1.1 \cdot 10^{15}$ | 1.6 (2.2) | 4.3 (1.2) | 0.41 (0.10) |
| | $2.0 \cdot 10^{15}$ | 1.8 (2.2) | 5.6 (3.6) | 0.54 (0.35) |

justified.

Comparing the data for the different fluences in figure 7.4 (b), it can be seen that the absorption resonance sharpens and intensifies with increasing irradiation fluence. This implies that the nanocrystal size and volume fraction increase with fluence. Table 7.1 shows the values of d and f as extracted from the fits shown in figure 7.4 (b). Also shown is the fraction of metallic Ag obtained by dividing f by the ion range and taking into account the density of Ag and the surrounding matrix. Data are also shown for ion-exchanged samples irradiated with 1 MeV Ne and 2 MeV Xe at various fluences. For these irradiations too, the nanocrystal size and volume fraction increase with fluence. Comparing the calculated fraction of metallic Ag in table 7.1 with the Ag concentration in the ion-irradiated region (7.0 at.% at the surface, gradually decreasing with depth), the fraction of ion-exchanged Ag⁺ that is incorporated into silver nanocrystals can be estimated. For the highest fluence irradiation (400 keV He, $8.1 \cdot 10^{16}$ ions/cm²), it amounts to roughly 12%.

It should be noted that the spectrum for the lowest irradiation fluence in figure 7.4 (b) does not show a characteristic resonance peak. This may indicate that the sample contains a large density of very small nanocrystals. Alternatively, it could be that the measured absorbance for low fluence irradiation is due to other sources than nanocrystals, e.g. ion irradiation-induced defects. In the latter case the absorbance data for the two highest irradiation fluences in figure 7.4 (b) after subtraction of a smooth background yields different values for the fit parameters, as shown between brackets in table 7.1.

Comparing the data from the XRD, TEM, and absorbance measurements for the high fluence He irradiation, it can be seen that two different typical nanocrystal diameters have been measured. The nanocrystals recorded using XRD (figure 7.2) have a diameter of ~ 13 nm, which is in agreement with the TEM data (figure 7.3), from which a maximum diameter around 10 – 15 nm is found. Note that mainly large nanocrystals contribute to peaks in the X-ray spectrum, as smaller species yield flat, broad peaks that cannot be detected. The TEM image also clearly shows that the majority of nanocrystals have radii of ~ 5 nm and smaller. This is in good agreement with the absorbance spectrum (figure 7.4 (b)), which yields an average nanocrystal diameter of 2.2 nm. Note for reference that a Ag nanocrystal of this size contains roughly 600 Ag atoms.

Measurements of the nonlinear properties of these ion irradiation-induced Ag nanocrystals have been performed using the Z-scan technique. Preliminary data show that the index of refraction shows a large negative electronic nonlinearity and a positive thermal contribution (Peters, 1998). In addition, a nonlinear absorption is found. These data indicate that the irradiation-induced Ag nanocrystals may indeed be used in all-optical switching applications, if the nonlinear absorption can be overcome.

7.3 Nanocrystal formation mechanism: electronic versus atomic displacement energy loss

Figure 7.5 shows the measured absorbance at $\lambda = 418$ nm as a function of the irradiation fluence for 400 keV He, 1 MeV Ne, and 2 MeV Xe irradiated samples. For all three irradiation conditions the absorbance increases with fluence. However, the fluence to reach a particular absorbance depends on the ion/energy condition used: the absorbance per Xe ion is larger than for Ne, which in turn causes more absorbance than He. The inset shows the integrated energy deposition in electronic excitations and in atomic displacements for the three irradiation conditions, calculated using TRIM. As can be seen, for all three ion species the largest fraction of the ion energy is deposited in electronic interactions. For the three ion/energy conditions used, the integrated electronic energy loss varies by less than a factor 3, while the energy lost in atomic displacements varies by more than a factor 50. Comparing the trends in the inset with the data for the three different ions, it appears that the nanocrystal formation efficiency trend found in the data is best represented by the trend in the atomic displacement calculation.

To further investigate this, the absorbance data in figure 7.5 were normalised to the integrated amount of energy loss deposited in atomic displacements. These data are shown in figure 7.6. For all ion species, the absorbance shows the same initial increase as a function of deposited energy. For higher energy deposition values, the Ne and Xe data follow the same trend shown by the solid line, while the data for He diverge sharply (dashed line). The difference between the results for He on the one hand and the heavy ions (Ne, Xe) on the other hand may be due to the fact that only a very

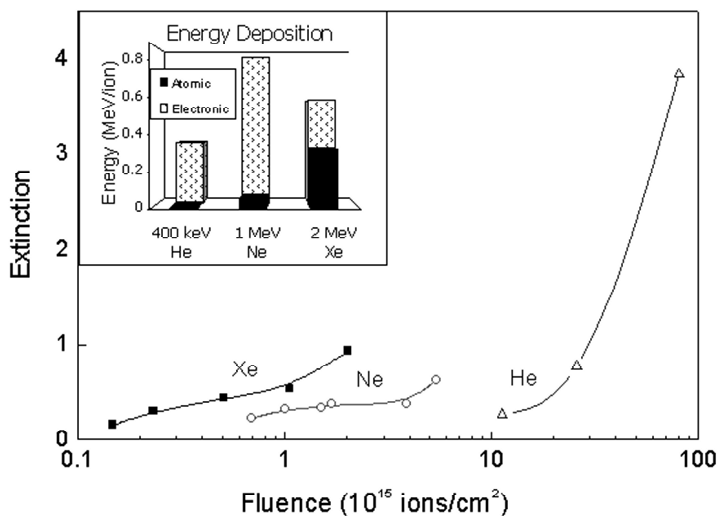


FIGURE 7.5: Absorbance at $\lambda = 418$ nm as a function of irradiation fluence for ion-exchanged samples irradiated with 400 keV He, 1 MeV Ne, and 2 MeV Xe. The inset shows the integrated energy deposited in atomic displacements and electronic excitations, as calculated using TRIM.

small fraction of the stopping for He is due to atomic displacement energy loss. The trends in figure 7.6 may be understood if it is assumed that nanocrystal formation may also be caused by electronic energy loss, though much less efficiently than by atomic displacements and that both of these processes have a different dependence on fluence. Indeed, it may be that both energy loss processes have a distinctly different effect on the nucleation and growth kinetics of nanocrystals. More measurements are needed to investigate this in more detail.

The conclusion that atomic displacement energy loss is the main factor responsible for nanocrystal nucleation seems in contradiction with data on the effect of light ion irradiation on nanocrystal formation by Caccavale et al. (1995). However, in the experiments in that reference, the atomic displacement energy loss component was very small, and therefore the effect of electronic energy loss may have become apparent. Indeed, our data above show that the nanocrystal formation rate during He irradiation is much smaller than during heavy ion irradiation. An article published by Ila et al. (1999) reported that electronic energy loss caused the growth of Au nanocrystals from an irradiated region containing pre-implanted Au ions. It is difficult to compare these data with those in the present article, as beam-induced effects of the Au implantation itself can cause nucleation of (small, possibly undetectable) nanocrystals during ion irradiation. In contrast, in our experiments the incorporation of the Ag ions by ion exchange and the ion irradiation are two independent processes.

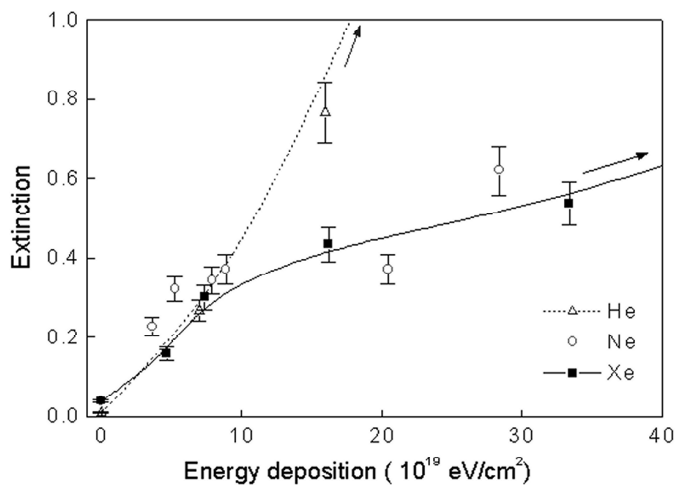


FIGURE 7.6: Absorbance at $\lambda = 418 \text{ nm}$ as a function of irradiation fluence normalised to atomic displacement energy loss for the same samples as in figure 7.5. The lines are a guide to the eye and arrows indicate the positions of additional data points for He and Xe outside the range of the graph.

7.4 Summary

Ag nanocrystals were formed by 400 and 500 keV He, 1 MeV Ne, and 2 MeV Xe irradiation of $\text{Na}^+ \longleftrightarrow \text{Ag}^+$ ion-exchanged sodalime glass. The nanocrystal size and volume fraction increase with ion fluence. For a 500 keV, $1.1 \cdot 10^{17} \text{ ions/cm}^2$ He irradiation, a broad nanocrystal size distribution is found, with diameters up to 10 – 15 nm. Up to $\sim 10\%$ of the ion exchanged Ag ions are incorporated in the nanocrystals. Comparing the extinction spectra for various irradiation conditions it is concluded that for Ne and Xe irradiation nanocrystals are most efficiently formed by the effect of the energy deposited in atomic displacement collisions. For He, an electronic energy deposition component may also play a role. Both kinds of energy deposition may have a different effect on the nucleation and growth of nanocrystals. These Ag nanocrystal doped ion-exchanged layers may serve as nonlinear waveguides for use in planar all optical switching components.

Chapter EIGHT

Silver nanocrystal doped waveguides with controlled transmission

WAVEGUIDES WITH A HIGH AG CONCENTRATION WERE FABRICATED BY MEANS OF AN $\text{Na}^+ \longleftrightarrow \text{Ag}^+$ ION EXCHANGE IN BOROSILICATE GLASS. SUBSEQUENTLY THE WAVEGUIDES WERE PARTLY IRRADIATED WITH XE IONS. THIS IRRADIATION INDUCES AGGREGATION OF SILVER TO FORM CRYSTALS IN THE NANOMETER SIZE RANGE. ION-IRRADIATED PLANAR WAVEGUIDES WERE USED TO ESTIMATE THE COMPLEX INDEX OF REFRACTION OF THE GLASS/AG NANOCRYSTAL COMPOSITE BY REFLECTION AND TRANSMISSION MEASUREMENTS. THE REAL PART OF THE INDEX OF REFRACTION REACHES VALUES OF UP TO 2.8 AT 442NM AND SHOWS A LARGE DISPERSION OVER THE WHOLE VISIBLE SPECTRUM. THE KNOWLEDGE OF THE OPTICAL CONSTANTS IS APPLIED TO THE INTERPRETATION OF TRANSMISSION MEASUREMENTS THROUGH STRAIGHT CHANNEL WAVEGUIDES WHICH WERE ION-IRRADIATED OVER LENGTHS BETWEEN $135 \mu\text{M}$ AND $271 \mu\text{M}$. THE TRANSPARENCY EDGE OF THE WAVEGUIDES SHIFTS TOWARDS LONGER WAVELENGTHS FOR INCREASING IRRADIATED REGIONS. THE RESULTS CAN BE EXPLAINED BY THE PLASMON ABSORPTION OF THE SILVER NANOCRYSTALS. WAVEGUIDES TREATED IN THIS WAY MAY FIND USE AS LONG-WAVELENGTH PASS FILTERS IN INTEGRATED OPTICS.

Glass/metal nanocrystal composites show unique optical properties in the visible. These are caused by collective electron excitations in the metal crystallites (Mie, 1908), and are characterised by a strong band of low optical transmission in the visible. For silver particles in oxide glasses this band is centred around 420 nm (Arnold and Borders, 1977; Hövel et al., 1993). Much effort has gone into understanding both the linear and nonlinear optical properties of such silver/glass composites (Hövel et al., 1993; Hamanaka et al., 1999; Flytzanis et al., 1991; Watanabe et al., 1998). From an applications point of view it is mainly their large nonlinear index of refraction that has drawn attention (Faccio et al., 1998; Osborne et al., 1998; Hamanaka et al., 1999). But also dichroic polarizers working with ellipsoidal silver particles have been demonstrated (Hofmeister et al., 1999).

It is tempting to extend the possibilities provided by glass/silver composites to the realm of integrated optics. This can lead to the development of optical waveguide devices utilising the effects listed above, but also furnish new means to analyse the formation of the nanocrystals and the properties of the composites. The latter has been attempted for float glass implanted with gold, silver, and copper ions in a planar waveguide configuration (Okur et al., 1999).

A straightforward method to form silver nanocrystals in waveguides makes use of the ion exchange technique to introduce Ag into a silicate glass substrate for waveguide definition and subsequent irradiation with ions to induce nanocrystal formation (Caccavale et al., 1995; Peters et al., 2000, see also chapter 7). Both processes allow for selection of the area treated using masking techniques and are possible on an industrial scale.

We have fabricated waveguides containing Ag nanocrystals with both planar and channel geometry by this method. We have used reflection and transmission data from planar waveguides to estimate the complex index of refraction of the glass/Ag nanocrystal composite. The real part of the index of refraction reaches values of up to 2.8 near the plasmon band, with large dispersion over the whole visible spectral region. The imaginary part of the index of refraction is used in the interpretation of transmission measurements through channel waveguides, which were irradiated over a length of several hundred micrometers to form nanocrystals. These waveguides act as long-wavelength pass filters with their transmission edge determined by the length of the region containing Ag nanocrystals.

8.1 Sample preparation and characterisation

Commercial Schott BK7 glass of 1 mm thickness was covered with 200 nm of aluminum by thermal evaporation. The Al layer served as a diffusion mask for the ion exchange process. A set of 4 μm wide openings was patterned into the Al layer by standard photolithographic techniques and etching in a Cl plasma. The samples were ion-exchanged in a 5 mol% AgNO_3 /95 mol% NaNO_3 melt at 350 °C for 60 min. With a similar treatment, the Ag^+ diffusion depth in a planar glass substrate amounts to

about 2500 nm. After the ion exchange, the Al mask was removed with a phosphoric acid etch mixture. The samples were cut with a diamond saw to a length of 1 cm and mechanically polished. The modes supported by the waveguides at 1480 nm were obtained by optical near field measurements. They are close to Gaussian with a full width at half maximum of $5.4 \mu\text{m}$ in the plane of the glass substrate, and $2.7 \mu\text{m}$ in the direction perpendicular to the substrate.

Subsequently, parts of the waveguides were irradiated at room temperature with xenon ions at an energy of 1 MeV to a fluence of $5 \cdot 10^{15} \text{ cm}^{-2}$. Irradiation with heavy as well as with light ions has been shown to lead to formation of Ag nanoclusters in ion-exchanged glasses (Caccavale et al., 1995; Peters et al., 2000). According to Monte Carlo calculations with TRIM (Ziegler et al., 1985), the range of 1 MeV Xe in ion-exchanged BK7 amounts to 430 nm. To control the length over which the individual waveguides were irradiated, we used a second, thick Al mask with a triangular opening. The lengths over which the waveguides were irradiated lie between $135 \mu\text{m}$ and $271 \mu\text{m}$.

Optical transmission spectra through the waveguides were taken both before and after irradiation. To this end, white light from a fibre-coupled halogen lamp was injected into the waveguides by end-fire coupling with a lensed fibre. The light issuing from the output facet of the waveguide was collected by a $40 \times$ microscope objective and imaged onto the entrance facet of a fibre with $600 \mu\text{m}$ core diameter. It was subsequently passed through a monochromator and detected by a thermoelectrically cooled AgOCs photomultiplier tube. The spectral resolution of the monochromator was set to approximately 3 nm. Lock-in techniques were used to decrease the noise level of the measurement.

Reflection and transmission of a planar reference sample irradiated under the same conditions as the channel waveguides were measured with a spectroscopic ellipsometer in the wavelength range from 300 nm to 1700 nm. Note that this sample is doped with Ag by ion exchange on both sides, but ion-irradiated only on one side. Transmission spectra were taken at normal incidence, reflection spectra at an angle of 20° for both s and p polarised light. To obtain an estimate of the normal incidence reflection of the sample, the measurements for the two polarisations were averaged. A calculation of the Fresnel coefficients shows that this method leads to the correct value for the normal incidence reflection to within less than 1%. Separate spectra were taken for the light incident on the ion-irradiated face of the sample and the unimplanted rear face. Corresponding measurements were performed on an ion-exchanged sample that had not undergone ion irradiation.

8.2 Index of refraction of the glass-silver composite

The complex index of refraction of the glass/Ag nanocrystal composite layer comprises all information necessary to evaluate the waveguide transmission experiments. We estimate it by measuring reflection and transmission of a planar, ion-exchanged substrate that has been ion-irradiated under the same conditions as the channel wave-

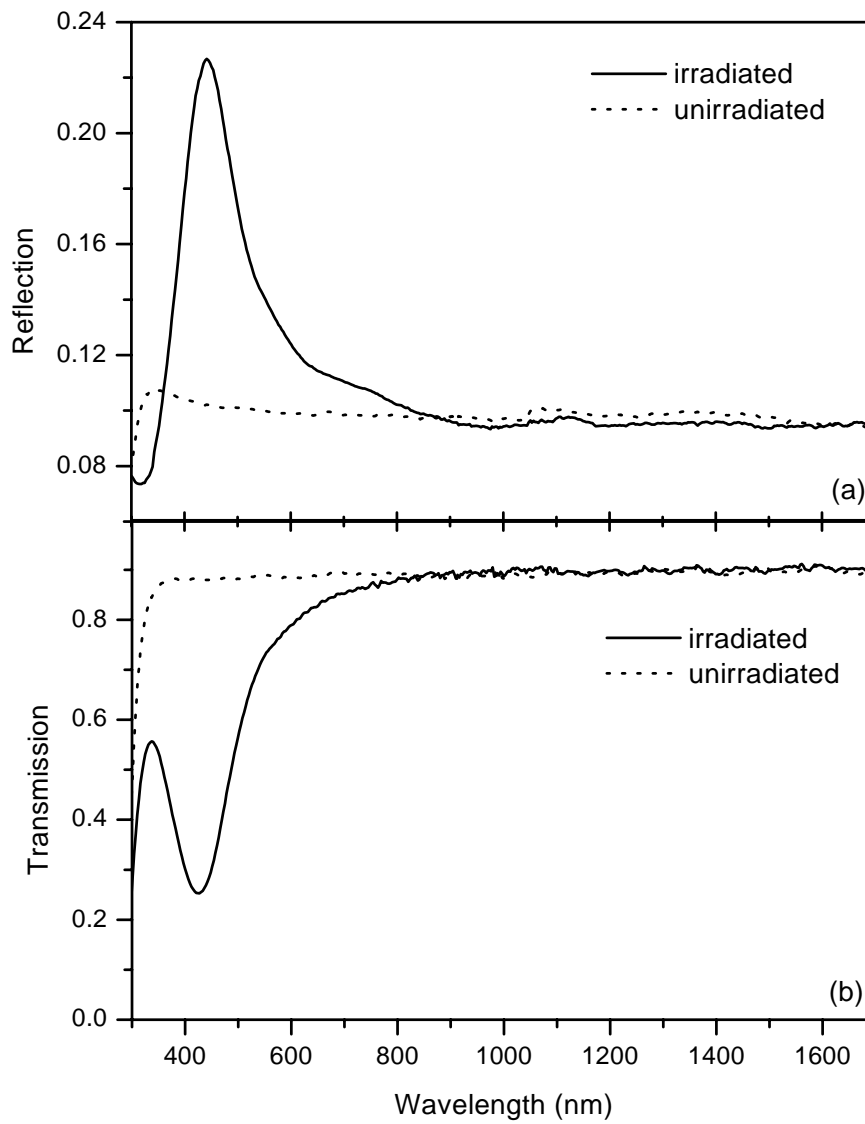


FIGURE 8.1: (a) Reflection and (b) transmission data of ion-exchanged borosilicate glass. The spectra of an unirradiated sample are compared with the ones of a sample irradiated with 1 MeV Xe ions. The resonance around 430 nm is due to the layer of glass/Ag nanocrystal composite formed by ion irradiation.

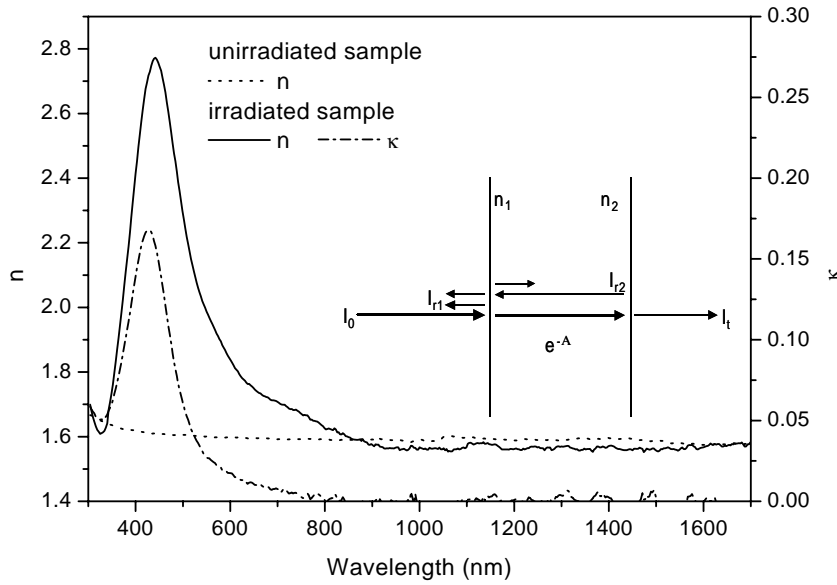


FIGURE 8.2: Optical constants of the glass/Ag nanocrystal composite layer as derived from the reflection and transmission measurements of figure 8.1. Also plotted is the real part of the index of refraction of the sample before irradiation. Its imaginary part κ is too small to be discerned on the scale of the plot. The inset shows a schematic representation of the model used for the derivation of the index of refraction from reflection and transmission measurements.

guides. The structure of the sample is as follows: a borosilicate glass slide, 1 mm thick, with two ion-exchanged surfaces with a graded index profile extending to a depth of approximately 2500 nm. Additionally one surface has been irradiated to form Ag nanocrystals up to a depth of around 430 nm. The size and density distribution of the Ag nanocrystals is determined by the energy loss profile of the implanted Xe ions (Peters et al., 2000, chapter 7 of this thesis). Both distributions are not known exactly. We will therefore estimate the index of refraction of this layer using a simple model.

The transmission and reflection spectra with light incident on the ion-irradiated face of the ion-exchanged and ion-irradiated glass are shown in figure 8.1 and compared to measurements for the unirradiated reference sample. The transmission spectrum shows a pronounced dip at 427 nm not seen in the unirradiated reference, which is generally attributed to the plasmon resonance of small Ag particles (Hövel et al., 1993). The reflection, on the other hand, has a strong peak at 442 nm. This peak is absent in the spectrum of the unirradiated sample. Only in the region with pronounced transmission and reflection features, significant changes in the index of refraction compared to the unirradiated reference sample are expected.

Consider the simple model depicted in the inset of figure 8.2. The glass slide is approximated by two surfaces with indices of refraction $n_1(\lambda)$ and $n_2(\lambda)$. The ambient medium is air with $n(\lambda) = 1$. Reflections inside the glass slide, from boundaries of the different layers present, have been disregarded. This approximation is made in view of the graded nature of the transitions between layers, which will minimize reflections at normal incidence¹. Inside the glass, the absorbance is described by $A(\lambda)$. It is related to the imaginary part of the index of refraction $\kappa(\lambda)$ by

$$A(\lambda) = \frac{2\pi}{\lambda} \kappa(\lambda) d. \quad (8.1)$$

λ is the wavelength in vacuum and d is the distance over which absorption or scattering takes place.

Within the framework of this model we can express transmission and reflection as

$$T = \frac{I_t}{I_0} = (1 - r_1) e^{-A} (1 - r_2) \quad (8.2)$$

$$R = \frac{I_r}{I_0} = r_1 + r_2 (1 - r_1)^2 e^{-2A} = r_1 + T^2 \frac{r_2}{(1 - r_2)^2}. \quad (8.3)$$

r_1 and r_2 are the reflection coefficients from facets 1 and 2, respectively. They are defined for intensities and should not be confused with the Fresnel coefficients, which describe electric fields.

Let us, for our purposes, define face 1 as the ion-irradiated face (and thus the one containing Ag nanocrystals), and face 2 as only ion-exchanged. We need to separate the reflections from the two faces. This can be achieved by means of a reference sample which has not been ion-irradiated. In that case, the two faces have the same reflection coefficients, and equation (8.3) can be solved for r_2 (a third order polynomial equation with only one real solution) using the measured values for R and T . With r_2 as input in equation (8.3) for the irradiated sample, we obtain r_1 . r_1 , the reflection from the sample face containing silver nanocrystals, is in turn related to the index of refraction via

$$r_1 = \frac{(n_1 - 1)^2 + \kappa_1^2}{(n_1 + 1)^2 + \kappa_1^2}. \quad (8.4)$$

The imaginary part of the index of refraction, κ , can be obtained from transmission measurements: by inverting equation (8.2) we obtain the absorbance $A(\lambda)$. The transmission spectrum of the ion-irradiated glass has two regions with low transmission,

¹In the case of a sharp interface between composite layer and substrate glass, the strong plasmon absorption prevents most of the light reflected from this interface from reaching the detector. The total contribution to the reflection caused by this extreme case of a graded profile is less than 1%, considering that the index contrast between composite and base glass decreases as the absorption decreases. The error in the real part of the index of refraction is less than 10%, with considerably higher accuracy ($\sim 3\%$) near the maximum of the absorption. The maximum of the imaginary part of the index of refraction would then be overestimated by also less than 10%. This estimate becomes more accurate the lower the real part of the index of refraction. For a graded index profile, the reflections of the composite-glass interface are weaker and the values of the index of refraction obtained are more accurate.

the dip between 400 nm and 500 nm, which we attribute to the plasmon absorption of the Ag nanocrystals, and the absorption edge at 300 nm, which is a feature of the glass itself. These two mechanisms are associated with different length scales: the glass band edge absorption occurs over the whole thickness of the glass slide (1 mm), whereas the plasmon resonance acts only over the thickness of the irradiated layer (430 nm). So as not to overestimate the absorption due to the plasmon resonance in the region of the glass band edge, we subtract the absorbance $A(\lambda)$ of the unirradiated glass from the one of the irradiated glass to obtain the absorbance due to the glass/silver nanocrystal layer. The imaginary part of the index of refraction of this layer can now be obtained using equation (8.1). The last step is to calculate the real part of the index of refraction via equation (8.4).

Figure 8.2 shows the real and imaginary parts of the index of refraction for the layer containing Ag nanocrystals produced by ion irradiation, and of the unirradiated ion-exchanged glass, both calculated by the method detailed above. The imaginary part of the latter lies below 10^{-4} over the whole wavelength region presented and therefore cannot be discerned on the scale of the plot. Its real part corresponds well with the value estimated from mode line measurements (Hoekstra, 1994) at 633 nm in a planar, ion-exchanged waveguide. Striking is the huge dispersion of the layer containing Ag nanocrystals. The real part of its index of refraction varies from 1.61 at 325 nm to 2.77 at 442 nm, and back to 1.57 in the infrared.

To check the validity of our model, which only takes into account reflections at the sample-to-air interfaces, we have measured reflection and transmission spectra with the light incident on the unirradiated face. While the transmission spectrum does not change significantly (as can be expected according to equation (8.2)), the reflection spectrum, shown in figure 8.3 is altered considerably. The maximum of the reflection decreases by a factor of two with respect to the data shown in figure 8.1 and is shifted towards longer wavelengths, now appearing at 553 nm. With the values of the optical constants derived above, we can calculate the expected reflection spectrum. The result, also plotted in figure 8.3, nicely reproduces the reduced height and shifted reflection peak. Note that the changed peak position is a feature mainly due to the large value of κ in the glass/nanocrystal layer at wavelengths just below the reflection peak. This adds credibility to the model, since apparently the light can be regarded as traversing the layer containing the Ag nanocrystals before it is reflected at the surface.

Incidentally, a similar dependence of the reflection on the direction of incidence has been noted earlier by Stepanov et al. (1999) for samples prepared by Ag ion implantation into sodalime glass. These authors attribute the change in reflectance peak height and position to differing Ag cluster size and density distributions at the two sides of the implanted layer. In our case, however, the main alteration of the reflectance features is a consequence of the optical properties of the glass/nanocrystal composite itself. Only the difference in the measured and calculated spectra of figure 8.3 could be due to changes with depth of the optical properties within the composite layer, or

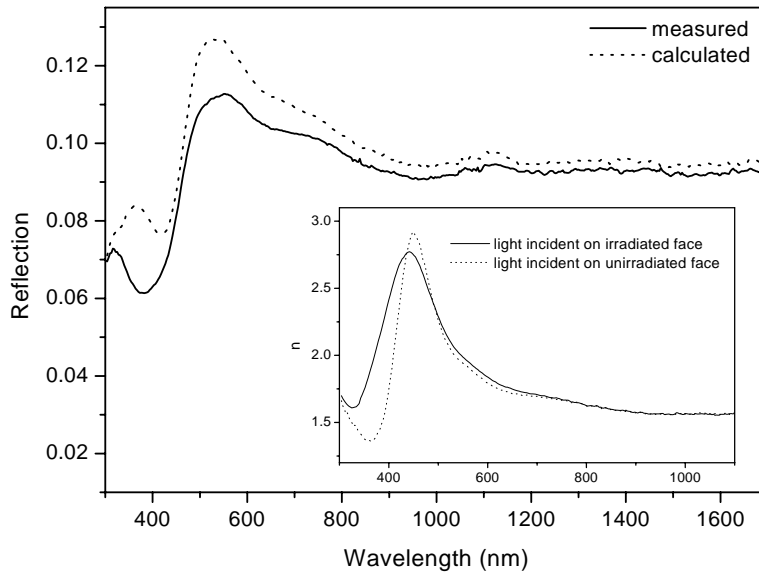


FIGURE 8.3: Reflection spectrum of ion-exchanged and irradiated borosilicate glass with the light incident on the unirradiated face of the sample. A calculation of this reflection using the optical constants given in figure 8.2 is overlaid. The inset compares the real part of the index of refraction obtained from measurements of the reflection from the irradiated and unirradiated face.

possibly to inaccuracies of our model².

It is possible to obtain an independent estimate of the index of refraction of the composite layer from the reflection data taken with the light incident on the unirradiated face of the sample. Its real part is plotted in the inset of figure 8.3 and is compared to the data in figure 8.2 for the real part of the index of refraction obtained from the reflection at the ion-irradiated face. Again, strong dispersion is observed, with the index reaching its maximum value of 2.92 at 451 nm. The difference between the two data sets is attributed to the fact that our simple model assumes homogeneous nanocrystal size and density distributions over depth. In reality, the distributions are graded and different reflection data are obtained when probing from different directions.

It is clear from the above discussion that it is difficult to measure the real part of the index of refraction of a Ag nanocrystal/glass composite fabricated by ion irradiation of an ion-exchanged glass with high accuracy. This is mainly due to its graded nature, which stems from the size and density distribution of the Ag nanocrystals over depth. It is, however, apparent that such a composite material exhibits unique dispersive features that might be put to use in highly dispersive integrated optics. In

²See footnote 1 for a discussion of the errors introduced by the simplifications of the model.

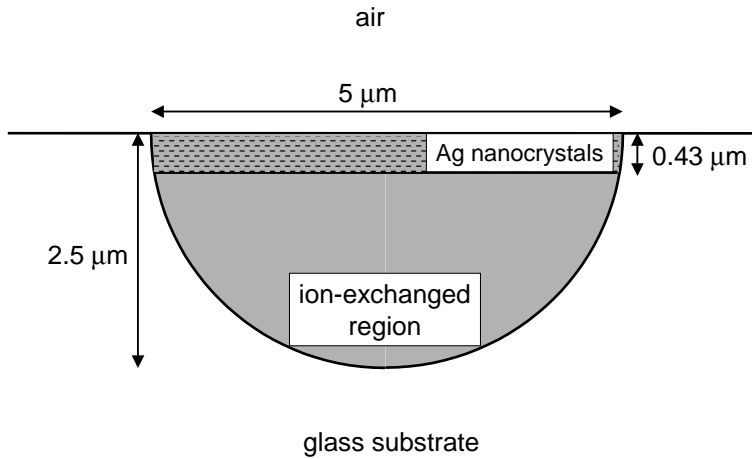


FIGURE 8.4: Schematic cross section of the ion-exchanged channel waveguides after irradiation with 1 MeV Xe ions. The ion-exchanged region has graded Ag^+ and index profiles. The Ag nanocrystals are formed in a surface layer up to the depth of the ion irradiation.

the following section we will apply our knowledge of the imaginary part of the index of refraction to analyze the effects of this composite material on the transmission of optical waveguides.

8.3 Waveguide transmission experiments

A clear change in colour identifies the irradiated regions of the waveguides. Their lengths are therefore easily determined with an optical microscope. They range from $135 \mu\text{m}$ to $271 \mu\text{m}$.

Figure 8.4 shows an impression of the cross section of such an ion-exchanged and subsequently ion-irradiated waveguide. The ion-exchanged region has a graded Ag concentration, decreasing with depth. Its value at the surface is approximately 7.5 at.% as determined by Rutherford Backscattering Spectrometry. The actual width of the waveguide has been inferred from the dimensions of the optical mode at 1480 nm. It is slightly bigger than the width of the channels in the mask ($4 \mu\text{m}$). The waveguide was irradiated with Xe ions to a depth of 430 nm. In this region the greater part of the silver nanocrystals form (De Marchi et al., 1996).

The transmitted intensity through a waveguide irradiated over a length of $201 \mu\text{m}$ is shown in figure 8.5 (a), together with a spectrum of the intensity transmitted by the same waveguide before ion irradiation. The curves have been corrected for the spectral response of the measurement setup without waveguide. The unirradiated

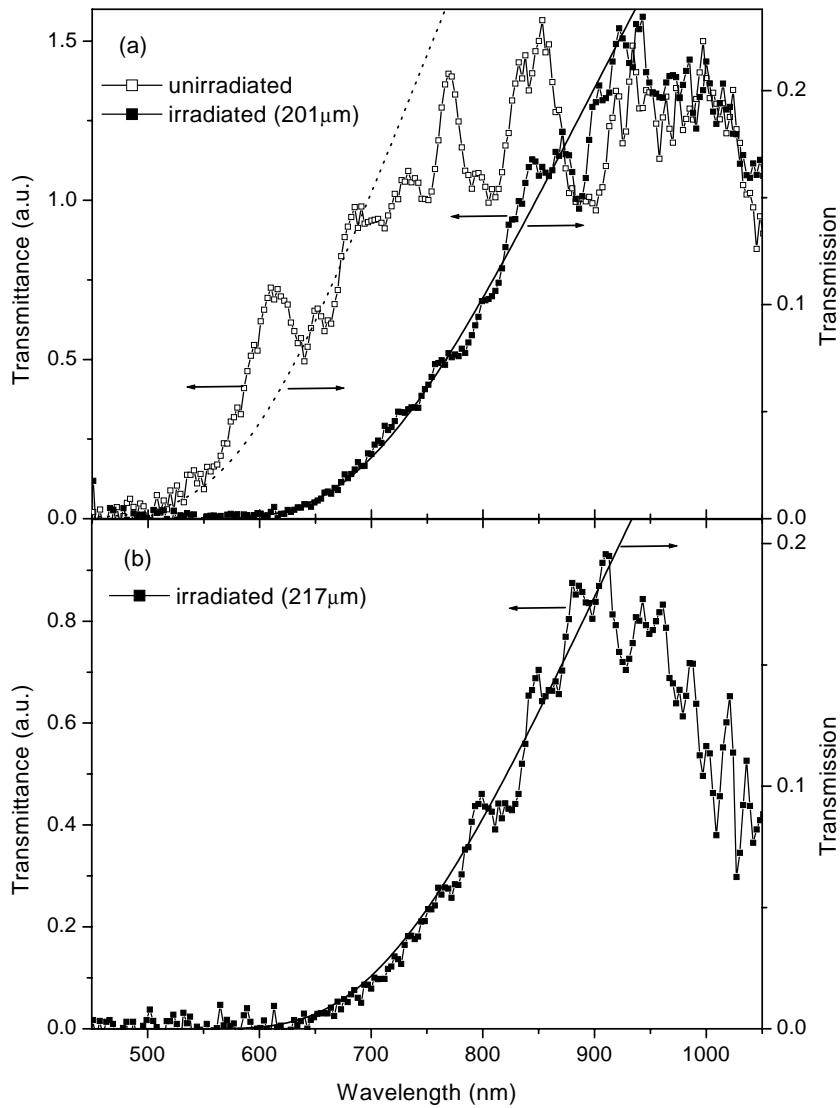


FIGURE 8.5: (a) Transmittance spectra through an ion-exchanged waveguide before and after irradiation of a 201 μm long section with 1 MeV Xe ions. The lines represent calculations according to equation (8.5). (b) Transmittance spectrum for a waveguide irradiated over a length of 217 μm and the corresponding calculation.

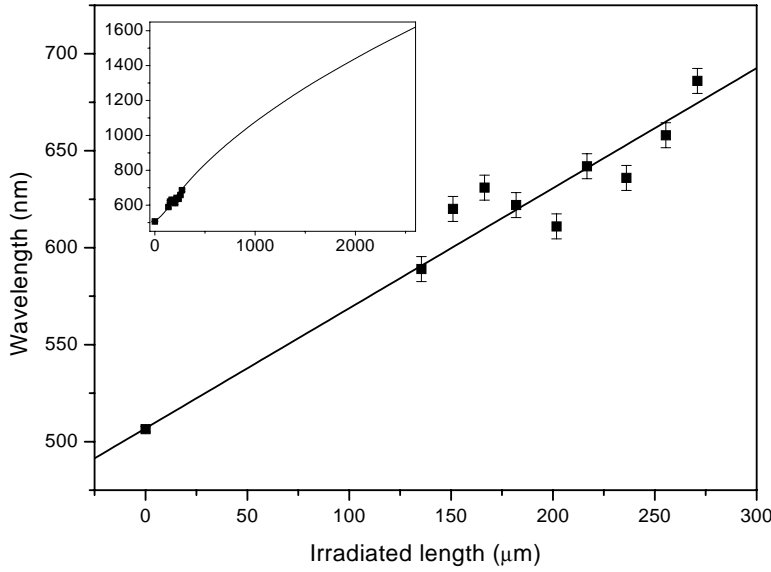


FIGURE 8.6: Plot of the wavelength at which transparency begins for waveguides irradiated over different lengths. The line illustrates the approximately linear dependence over the investigated range of irradiated lengths. The inset shows an extrapolation of the data to longer wavelengths using equation (8.6).

waveguide is transparent at wavelengths longer than about 500 nm. After irradiation, i.e. containing a region where a glass/Ag nanocrystal layer was formed, the waveguide only becomes transparent at 610 nm. We interpret the plateau at long wavelengths as the transmission limit determined by the waveguide properties. The structure in the spectrum is either caused by wavelength-selective scattering in the waveguides, or is a signature of modal dispersion. It is well reproducible for each waveguide, but differs from waveguide to waveguide.

The onset of transparency of the sample waveguides depends on the length of the irradiated region. It is defined as the wavelength at which the transmitted intensity deviates significantly from the noise around zero. The data for our waveguides are plotted in figure 8.6. At zero irradiated length we included the average value obtained for all waveguides before irradiation. It is apparent from figure 8.6 that the absorption edge can be moved through a great part of the visible spectrum by varying the length of the waveguide section doped with silver nanocrystals.

The transmission through waveguides containing metal nanocrystals can be written as

$$T_{wav} = f_{wav} \exp\{-\alpha(\lambda) \eta(\lambda) l_{nc}\} \quad (8.5)$$

with $\alpha(\lambda)$ the absorption of the glass/metal nanocrystal composite (related to the complex index of refraction by $\alpha = 2\pi\kappa/\lambda$), $\eta(\lambda)$ the overlap integral between the

metal nanocrystal-doped region and the waveguide mode, and l_{nc} the length of the ion-irradiated region. f_{wav} is a factor that takes into account the properties of the waveguide itself, such as propagation and coupling losses.

As can be seen from equation (8.5), absorption α , overlap integral η , and the length of the waveguide containing Ag nanocrystals are equivalent in the formula. It is therefore necessary to determine these parameters independently. While the irradiated length can be measured readily by optical microscopy, the only data available for α is by normal incidence transmission measurements (see section 8.2). This method averages the absorption over the depth of the waveguide. Its utilisation for waveguide transmission is only justified when the intensity over the layer containing Ag nanocrystals is approximately constant. This is indeed a reasonable assumption since the thickness of the layer is an order of magnitude smaller than the vertical extent of the waveguide (see figure 8.4). We will therefore make use of the absorption data obtained in section 8.2.

In order to smooth the experimental noise in the absorption data obtained in the previous section, we utilise a fit to these data according to the dipolar approximation of Mie theory (Mie, 1908) for scattering from metal spheres in a dielectric background (see chapter 7 for more details):

$$\alpha(\lambda) = 9f\epsilon_m^{3/2} \frac{\omega}{c} \frac{\epsilon_2(\omega)}{\left((\epsilon_1(\omega) + 2\epsilon_m)^2 + \epsilon_2(\omega)^2\right)} \quad (8.6)$$

with

$$\begin{aligned} \epsilon_1(\omega) &= \epsilon'_1(\omega) + 1 - \frac{\omega_p^2}{\omega^2 + \omega_c^2} \\ \epsilon_2(\omega) &= \epsilon'_2(\omega) + \frac{\omega_c}{\omega} \frac{\omega_p^2}{\omega^2 + \omega_c^2} \end{aligned}$$

where

$$\omega_c = \frac{v_f}{l} + \frac{2v_f}{d}.$$

$\omega = 2\pi c/\lambda$ is the angular frequency, and c the speed of light in vacuum. ϵ_1 and ϵ_2 represent the real and imaginary part of the dielectric constant of the silver nanocrystals, and ϵ'_1 and ϵ'_2 the respective contributions to the dielectric constant of bulk silver due to interband transitions (we have used the dielectric constants determined by Johnson and Christy (1972)). $\omega_p = 1.37 \cdot 10^{16} \text{ s}^{-1}$ is the plasma frequency of bulk silver, $v_f = 1.38 \cdot 10^6 \text{ m/s}$ the Fermi velocity and $l = 5.7 \cdot 10^{-8} \text{ m}$ the electron mean free path of electrons in bulk silver (Ashcroft and Mermin, 1976).

Assuming only one nanocrystal size, we obtain the best fit to the absorption data for the following values of the adjustable parameters: volume fraction of silver in the nanocrystal containing layer $f = 0.013$, average nanocrystal diameter $d = 2.1 \text{ nm}$, dielectric constant of the glass in the composite layer $\epsilon_m = 2.47$ ($n_m = 1.57$). The latter corresponds well to the index of refraction of the ion-exchanged reference sample measured in the previous section, taking into account that some fraction of the Ag

ions has formed nanocrystals and therefore does not contribute to the index of the glass any more.

The overlap integral is adjusted for a good fit to the transmission spectrum of the waveguide irradiated over a length of $201\ \mu\text{m}$. It amounts to $\eta = 0.115$. The calculated curve is shown as the solid line in figure 8.5 (a). The factor f_{wav} has been set to unity.

By assuming α and η as determined above, equation (8.5) reproduces the start of transparency and the flanks of the transmittance spectra through all waveguides when the measured values for the length of the irradiated region are used. This is shown exemplarily for a second waveguide in figure 8.5 (b).

As for the transmittance of the unirradiated waveguide (see figure 8.5 (a)), it is not possible to explain its opacity at wavelengths shorter than $500\ \text{nm}$ with the optical constants of the ion-exchanged glass derived in section 8.2. Induced by the similarity in shape of the transmittance spectra of unirradiated and irradiated waveguides, we have attempted to explain its form by an absorption caused by a very low concentration of silver nanocrystals that might have spontaneously nucleated in the ion-exchanged region. A volume fraction of Ag nanocrystals of below 10^{-4} in the ion-exchanged layer would not be discernible in normal-incidence transmission measurements like the ones shown in figure 8.1. In the waveguide, however, the interaction length – and thus the sensitivity – of a transmission measurement is increased by more than three orders of magnitude.

Adjusting equation (8.5) to the data, with α given by the Mie expression equation (8.6), l_{nc} set to the waveguide length of $10\ \text{mm}$, ϵ_m to 2.56 as obtained in section 8.2, and η estimated as 0.45 , we obtain the dotted line in figure 8.5 (a) when setting $f = 1.75 \cdot 10^{-5}$ and $d = 0.9\ \text{nm}$. The reasonable agreement of this curve with the data suggests that a minute fraction of the Ag^+ ions diffused into the glass nucleates and forms metallic nanocrystals. Note that the actual values for nanocrystal size and volume fraction given here are only rough estimates.

Finally, turning again to figure 8.6, we notice that the wavelength at which the irradiated waveguides become transparent increases roughly linearly with the length of the irradiated part of the waveguides. The exact dependency is determined by $\alpha(\lambda)l_{nc} = \text{const}$, where the constant is related to the precise definition of the onset of transparency. In the range of lengths available in our experiment this relation leads indeed to an approximately linear dependence.

Using the Mie equation (8.6), the length of the region containing silver nanocrystals required for any particular wavelength of the onset of transparency can be calculated. The result is shown in the inset of figure 8.6, together with the measured data from the main plot. It can be seen that the onset of transparency moves to $1550\ \text{nm}$, the standard wavelength for optical fibre communications, when the irradiated region of the waveguide is around $2.4\ \text{mm}$ long. This prediction assumes of course that the absorption in our samples is still well represented by equation (8.6) far from the resonance, which has never been investigated experimentally.

This dependence of transmission on irradiated length opens possibilities for appli-

cations in integrated optics. Long-wavelength pass filters can be directly integrated in ion-exchanged waveguides, where the cutoff wavelength is determined by the length of the region in the waveguide containing Ag nanocrystals. Furthermore, making use of the nonlinear optical properties of glass/Ag nanocrystal composites, in this special case the high nonlinear absorption caused by two-photon interband transitions and hot electron effects (Flytzanis et al., 1991), these filters can potentially be tuned. This is a more general case of the previously suggested application of glass/metal nanoparticle composites as optical limiters (Lepeshkin et al., 1999; Sun et al., 1999).

8.4 Summary

We have fabricated waveguides containing silver by an $\text{Na}^+ \longleftrightarrow \text{Ag}^+$ ion exchange in borosilicate glass. They were subsequently subjected to irradiation with Xe ions to form silver nanocrystals in the waveguides.

On a planar waveguide, we estimated the complex index of refraction of the glass/Ag nanocrystal composite from reflection and transmission measurements. In the spectral range of the plasmon resonance of the silver nanocrystals, its real part reaches values of 2.8. Differences in the reflection spectra taken from the implanted face and the unimplanted face of the sample can be explained to a great extent by the high absorbance of the composite layer.

Channel waveguides were ion-irradiated over lengths ranging from $135 \mu\text{m}$ to $271 \mu\text{m}$. Transmittance measurements through these waveguides evidence a shift in the onset of the transparent region towards longer wavelengths with increasing irradiated length. This dependence can be accounted for by the absorption caused by the plasmon resonance in the silver nanocrystals. The transmittance of unirradiated waveguides indicates the presence of a low density of silver nanocrystals. The waveguides containing silver nanocrystals effectively act as long-wavelength pass filters, where the cutoff wavelength can be adjusted via the length of the region doped with nanocrystals.

Chapter **NINE**

Highly dispersive micropatterns in ion-exchanged glass formed by ion irradiation through a mask of colloidal particles

WE HAVE FABRICATED REFRACTIVE INDEX GRATINGS WITH HEXAGONAL SYMMETRY IN $\text{Na}^+ \longleftrightarrow \text{Ag}^+$ ION-EXCHANGED BOROSILICATE GLASS BY ION IRRADIATION THROUGH A MASK OF SELF-ORGANISED SILICA COLLOIDAL PARTICLES. THE INDEX INCREASE IN THE IRRADIATED REGIONS OF THE GLASS IS CAUSED BY THE FORMATION OF SILVER NANOCRYSTALS UNDER THE INFLUENCE OF THE ION BEAM. LIGHT SCATTERING MEASUREMENTS SHOW DIFFRACTION RINGS AND PEAKS BELONGING TO HEXAGONAL SYMMETRY WITH A LATTICE CONSTANT APPROXIMATELY EQUAL TO THE DIAMETER OF THE PARTICLES IN THE COLLOIDAL MASK.

The optical constants of composite materials formed by metal nanocrystals in an insulating background material are at the bottom of various interesting optical properties of such materials both in the linear (Kreibig, 1974) and nonlinear regime (Flytzanis et al., 1991). As for the linear optical properties, mainly the surface plasmon resonance absorption of such composites has been studied (Kawabata and Kubo, 1966; Tiggesbäumker et al., 1992; Hövel et al., 1993). Paired with this absorption is a considerable variation of the real part of the index of refraction (Kreibig, 1970, see chapter 8 of this thesis). Silver nanocrystals in oxide glass have their plasmon resonance absorption in the violet around 420 nm. The corresponding variation in the real part of the index of refraction of such composites extends from the ultraviolet to the green.

The index of refraction of a glass containing silver ions can thus be changed by nucleating silver nanocrystals. In contrast to many other ions, silver can be introduced into oxide glasses containing network modifiers such as Na^+ or K^+ a posteriori via ion exchange, which allows for the incorporation of silver ion concentrations of several atomic percent. Silver nanocrystals can be formed by ion irradiation of the ion-exchanged glass (Arnold and Borders, 1977; Peters et al., 2000; Valentin et al., 2001, see also chapter 7). This formation process, in contrast to anneals in controlled atmosphere, opens the possibility to nucleate silver nanocrystals in selected regions of a sample only, and thereby change the index of refraction. A regular pattern of index variations can find application as a diffraction grating, waveguide multiplexer or photonic crystal. In this chapter we explore the formation of such regular refractive index variations making use of colloidal silica particles deposited on the ion-exchanged glass as an implantation mask. Colloidal particles self-organise on a flat substrate when the solvent evaporates (Denkov et al., 1992), forming a hexagonal array. Only in the spaces between the particles, formation of silver nanocrystals occurs when the sample is irradiated with an ion beam. The outcome is a highly dispersive hexagonal pattern written directly into the glass substrate.

9.1 Sample preparation and characterisation techniques

Borosilicate glass was ion-exchanged for 5 min at 320 °C in a 8.3 mol% AgNO_3 /91.7 mol% NaNO_3 melt. Such an ion exchange gives rise to a surface layer in the glass with a graded Ag^+ concentration up to a depth of around 1 μm . The silver concentration at the surface amounts to 7.5 at.%, as measured by Rutherford Backscattering Spectrometry. Colloidal silica particles of 1.66 μm diameter were prepared from seeds grown by the usual ammonia-catalyzed Stöber synthesis (Stöber et al., 1968) using a continuous growth set-up as described by Giesche (1994). They were dissolved in ethanol and deposited onto the ion-exchanged glass. The silica particles ordered into a two dimensional hexagonal array during the evaporation of the solvent (Denkov et al., 1992). They served as a mask for ion irradiation of the ion-exchanged glass.

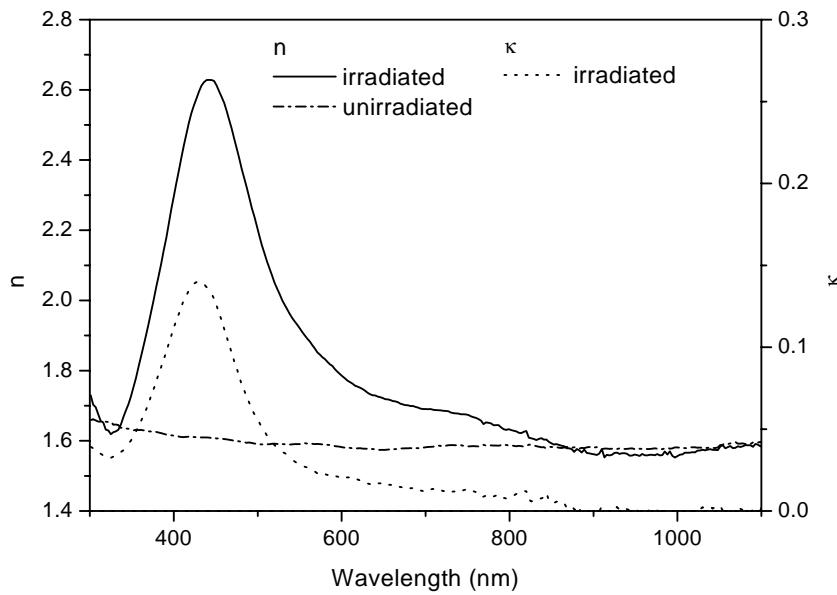


FIGURE 9.1: Real and imaginary parts of the index of refraction of Ag ion-exchanged borosilicate glass before and after ion irradiation. The imaginary part of the glass index of refraction before irradiation does not exceed $2 \cdot 10^{-5}$ over the spectral range plotted and is not visible on the scale of the graph. The peaks in both real and imaginary part of the index of the glass after irradiation are caused by the surface plasmon resonance of small silver particles formed in the irradiated layer. The data was obtained from reflection and transmission measurements of samples prepared without a colloidal mask.

The glass with its mask of colloidal particles was cooled to 77 K and irradiated with Xe ions at an energy of 1 MeV to a fluence of $5 \cdot 10^{15} \text{ cm}^{-2}$. The projected range of the Xe ions in silica is around 450 nm, considerably less than the diameter of the mask particles. During irradiation with heavy ions, silver nanocrystals are formed in the glass (Peters et al., 2000, chapter 7) in a layer determined by the range of the implanted ions. This layer of glass/silver nanocrystal composite has an elevated index of refraction in the blue and green region of the visible spectrum (see chapter 8). After irradiation, the colloidal particles were removed from the surface of the glass.

The index of refraction of the composite layer was estimated by reflection and transmission measurements according to the method described in chapter 8 of this thesis. The samples used for this purpose were prepared under identical conditions, but had been ion-irradiated without mask. Figure 9.1 shows the index of refraction of the planar ion-exchanged and ion-implanted layer estimated from reflection and transmission measurements. The measurements are compared to the index of refraction of the unirradiated glass. The strong features in both the real and imaginary parts of the index of refraction with peaks at 442 nm and 430 nm, respectively, are caused by the

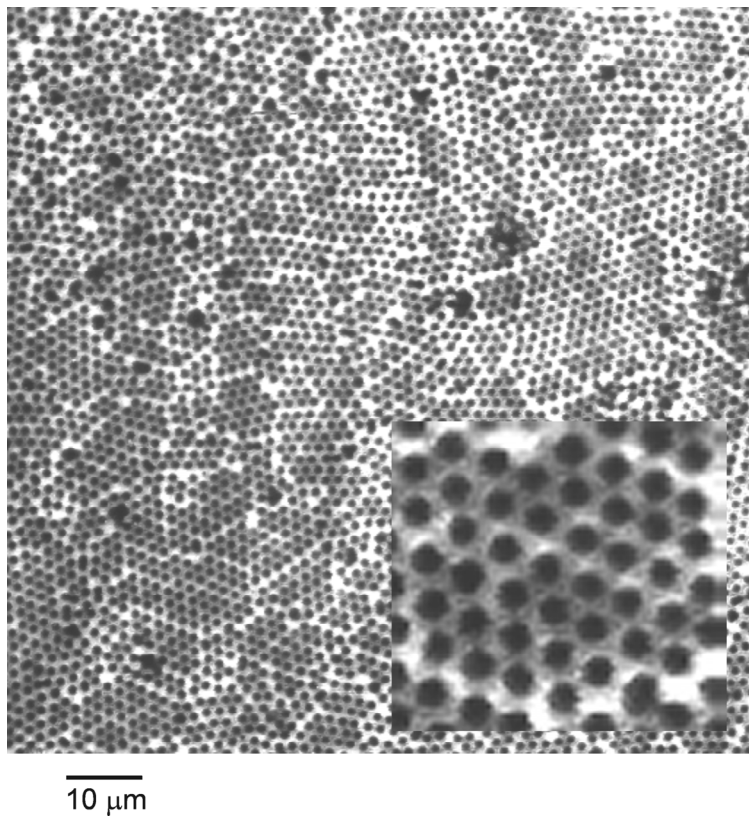


FIGURE 9.2: Reflection image of a region of the sample ion-irradiated through a colloidal mask, taken with a laser scanning confocal microscope at a wavelength of 488 nm, after the colloidal particles were removed. Light regions correspond to areas that reflect the light more strongly than dark regions. A hexagonal pattern of circular regions of low reflectivity is seen. This pattern is attributed to the masking effect of a hexagonal array of colloidal spheres with $1.66 \mu\text{m}$ diameter during ion irradiation. The inset shows a magnified image of a hexagonally ordered domain.

surface plasmon resonance of silver nanocrystals in glass (Kreibig, 1974). The average diameter of the silver nanocrystals is 2 nm (estimated from a fit of Mie theory (Mie, 1908) to the absorbance of the irradiated layer), with interparticle distances of the order of 10 nm. Both these values are very much smaller than the openings in the colloidal mask and than the wavelength of visible light. The glass/Ag nanocrystal composite in the irradiated regions of the masked sample is therefore as homogeneous as the one in the reference sample. This means that the optical constants of the irradiated regions of the masked sample are comparable to the ones determined for the reference sample.

The samples that had been irradiated through a mask of colloidal particles were analysed in a confocal laser scanning microscope in reflection mode at a wavelength of 488 nm after removal of the colloidal particles. We used a $100\times$ objective lens with a numerical aperture of 1.4. Light scattering experiments were performed with a He-Cd laser operating at 442 nm in transmission geometry. The footprint of the laser on the sample was around $300\ \mu\text{m}$. The light scattered by the sample was projected onto a screen and imaged using a CCD camera.

9.2 Optical microscopy and light scattering

Figure 9.2 shows a laser scanning microscope image of the irradiated sample after removal of the colloidal mask. The image was taken in reflection mode at a wavelength of 488 nm. The light regions in the image correspond to areas that reflect light more strongly than the dark regions. The image consists of dark circular regions forming a polycrystalline hexagonal pattern in a light background. It is evident that this image reproduces the “shadow” of the colloidal mask, with the dark circles marking the positions held by the silica particles during the ion irradiation. The high reflectivity of the area where the glass/Ag nanocrystal composite has formed ($R = 0.16$) is a signature of the elevated index of refraction of these regions compared to the base glass ($R = 0.05$, see figure 9.1). The period of the hexagonal array measured in crystalline domains is $1.68 \pm 0.02\ \mu\text{m}$, in close correspondence to the diameter of the silica particles used as the mask.

Light scattering experiments were performed to further study the structure of the sample. In this type of experiments, the reciprocal lattice of the scattering array is observed directly. A hexagonal array of scatterers also has hexagonal symmetry in reciprocal space. In figure 9.3 we show an image of the scattering pattern in transmission using 442 nm radiation on the same sample as depicted in figure 9.2. The polycrystalline configuration leads to the appearance of diffraction rings. Two rings, a strong inner and a weak outer ring (the latter not shown in figure 9.3), can be discerned. With the modulus of the scattering vector k_{sc} evaluated as

$$k_{sc} = \frac{4\pi}{\lambda} \sin \frac{\theta}{2}, \quad (9.1)$$

with λ the wavelength in vacuum of the scattered light and θ the scattering angle, the

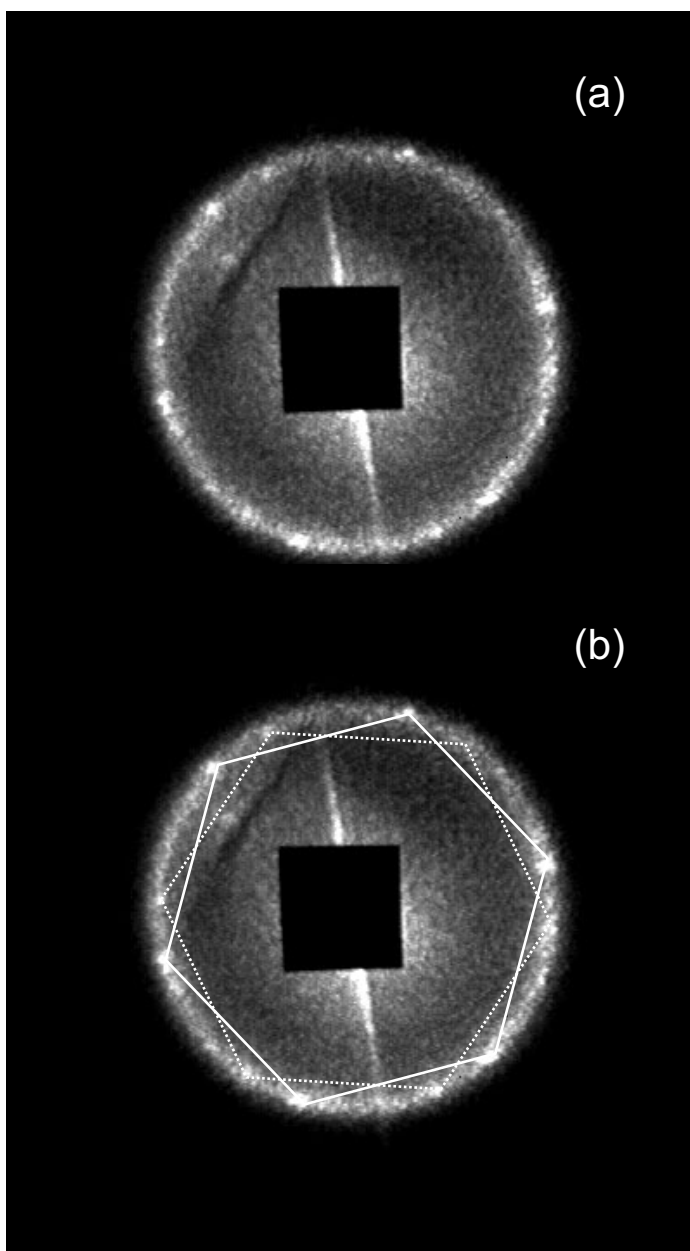


FIGURE 9.3: Diffraction image of an ion-exchanged borosilicate glass irradiated through a mask of colloidal spheres. On top of a diffuse ring, bright spots are observed that indicate the hexagonal symmetry of the arrangement of the scatterers. Part (b) shows the same data, overlaid by two hexagons, corresponding to diffraction from two differently oriented domains. The modulus of the scattering vectors associated with this pattern is approximately $3.9 \cdot 10^6 \text{ m}^{-1}$, which corresponds to a lattice constant of $1.6 \mu\text{m}$.

radii of the two rings correspond to scattering vectors of lengths $3.9 \pm 0.2 \cdot 10^6 \text{ m}^{-1}$ and $7.0 \pm 0.3 \cdot 10^6 \text{ m}^{-1}$. The ratio of these two values is $1/\sqrt{3}$ within our measurement error, which is to be expected for hexagonal symmetry. The values correspond to a lattice constant of $1.6 \pm 0.1 \mu\text{m}$. Identical values for the scattering vectors are obtained when light of different wavelengths in the blue and green is used. The scattering efficiency decreases, however, for longer wavelengths, in correspondence with the decrease of the index contrast (see figure 9.1). For 633 nm light, the scattered intensity was below the sensitivity of our measurement. Note that equation 9.1 describes scattering in vacuum and not in glass. It is valid in our case where the ratio between glass thickness and observation distance is small.

At several places on the sample the extent of the hexagonal domains is of the order of the footprint of the laser. There the light is scattered mainly from only one or two domains. The bright diffraction spots on the diffuse ring in figure 9.3 correspond to diffraction from such an area. These spots lie on the corners of hexagons, as is seen more clearly in figure 9.3 (b). It shows the same data as figure 9.3 (a), now overlaid with two hexagons connecting two sets of diffraction spots. This correlation is further evidence that diffraction takes place from hexagonally ordered scatterers.

From the width of the diffraction ring we can estimate the average size of the crystalline domains. At small angles (the ring in figure 9.3 corresponds to a scattering angle of 17°), the ratio between width and radius of the diffraction ring is approximately equal to the ratio between lattice constant and average domain diameter. This relation yields an average domain size of $17 \mu\text{m}$. This value is in good agreement with the average domain size observed in figure 9.2.

Measurements with an atomic force microscope in contact mode reveal that the irradiation with Xe ions changes the morphology of the surface: irradiated regions are elevated by 30 – 40 nm above the unirradiated areas. However, considering the aforementioned wavelength dependence of the scattering efficiency, this physical grating superposed on the index grating is not the principal mechanism causing the diffraction we observe. The wavelength dependence of the scattering efficiency of such a physical grating is considerably weaker than the one observed.

In the present experiment, the size of the colloidal particles used as the irradiation mask has been chosen such that the structures fabricated in the glass are clearly visible in an optical microscope. However, the technique described here is not limited to this size range. Smaller colloidal silica particles are even easier to fabricate than large ones and self-organise in the same fashion. The lower limit for the period of the grating is the range of the ions used to form silver nanocrystals in the glass. For the conditions used in our experiments, colloidal particles with a diameter of 600 nm are still sufficient to stop 1 MeV Xe ions whose range is around 450 nm in silica. Two possibilities seem viable to further reduce the period of the structure written into the glass: a reduction of the ion energy used for the irradiation would alleviate the requirements on mask thickness and also produce shallower gratings; the use of different mask materials with higher stopping for Xe ions, such as Ag or Au (Graf and van Blaaderen, 2001), or of anisotropically shaped particles (which have to be

made to stand upright) will also lead to a shorter period, at unchanged properties of the glass/Ag nanocrystal layer. Let us also note that techniques have been developed to fabricate two-dimensional single-crystalline domains of colloidal particles on the centimeter scale. Using such domains of a size greater than the dimensions of the incoming light beam allows the diffracted intensity to be localised in the diffraction spots rather than a diffraction ring. Finally, colloidal particles can be deposited in arrays of other symmetries than hexagonal with the help of optical tweezers or a templated substrate (van Blaaderen et al., 2001). In this way a variety of diffraction symmetries become available.

9.3 Summary

In summary, we have fabricated hexagonally ordered arrays of scatterers in ion-exchanged glass by ion irradiation through a hexagonal mask of self-organised colloidal silica particles. The contrast of the refractive index between ion-irradiated and unirradiated regions is caused by the formation of silver nanocrystals under the influence of the ion beam. In light scattering experiments we observed diffraction patterns corresponding to hexagonal symmetry with a period of $1.6 \mu\text{m}$, which correlates well with the diameter of the silica particles used as implantation mask.

Bibliography

- M. Alouini, M. Brunel, F. Bretenaker, M. Vallet, and A. Le Floch. Dual Tunable Wavelength Er:Yb:Glass Laser for Terahertz Beat Frequency Generation. *IEEE Photonics Technology Letters*, Vol. 10, No. 11, pp. 1554–1556, November 1998.
- A. A. Andronov, I. A. Grishin, V. A. Gur'ev, V. V. Orekhovskii, and A. P. Savikin. Enhancement of the luminescence yield of Er^{3+} ions at $\lambda = 1.54 \mu\text{m}$ in ZBLAN glass additionally doped with Eu^{3+} and Tb^{3+} and pumped in the range $\lambda = 0.975 \mu\text{m}$. *Technical Physics Letters*, Vol. 24, No. 5, pp. 365–366, May 1998.
- G. W. Arnold and J. A. Borders. Aggregation and migration of ion-implanted silver in lithia-alumina-silica glass. *Journal of Applied Physics*, Vol. 48, No. 4, pp. 1488–1496, April 1977.
- G. W. Arnold, G. De Marchi, F. Gonella, P. Mazzoldi, A. Quaranta, G. Battaglin, M. Catalano, F. Garrido, and R. F. Haglund Jr. Formation of nonlinear optical waveguides by using ion-exchange and implantation techniques. *Nuclear Instruments and Methods B*, Vol. 116, No. 1–4, pp. 507–510, August 1996.
- E. F. Artem'ev, A. G. Murzin, Yu. K. Fedorov, and V. A. Fromzel. Some characteristics of population inversion of the $^4\text{I}_{13/2}$ level of erbium ions in ytterbium–erbium glasses. *Soviet Journal of Quantum Electronics*, Vol. 11, No. 9, pp. 1266–1268, September 1981.
- R. W. Ashcroft and N. D. Mermin. *Solid State Physics*. Saunders College, Philadelphia, 1976.
- F. E. Auzel. Materials and Devices Using Double-Pumped Phosphors with Energy Transfer. *Proceedings of the IEEE*, Vol. 61, No. 6, pp. 758–786, June 1973.
- D. Barbier, M. Rattay, F. Saint André, G. Clauss, M. Trouillon, A. Kevorkian, J.-M. P. Delavaux, and E. Murphy. Amplifying Four-Wavelength Combiner, Based on Erbium/Ytterbium-Doped Waveguide Amplifiers and Integrated Splitters. *IEEE Photonics Technology Letters*, Vol. 9, No. 3, pp. 315–317, March 1997.

- E. Borsella, G. Battaglin, M. A. Garcia, F. Gonella, P. Mazzoldi, R. Polloni, and A. Quaranta. Structural incorporation of silver in soda-lime glass by the ion-exchange process: a photoluminescence spectroscopy study. *Applied Physics A*, Vol. 71, pp. 125–132, 2000.
- F. Caccavale, G. De Marchi, F. Gonella, P. Mazzoldi, G. Meneghini, A. Quaranta, G. W. Arnold, G. Battaglin, and G. Mattei. Irradiation-induced Ag-colloid formation in ion-exchanged sod-lime glass. *Nuclear Instruments and Methods B*, Vol. 96, No. 1–2, pp. 382–386, March 1995.
- E. Cantelar, J. A. Muñoz, J. A. Sanz-García, and F. Cussó. Yb³⁺ to Er³⁺ energy transfer in LiNbO₃. *Journal of Physics: Condensed Matter*, Vol. 10, pp. 8893–8903, 1998.
- E. Cantelar, R. Nevado, G. Lifante, and F. Cussó. Modelling of optical amplification in Er/Yb co-doped LiNbO₃ waveguides. *Optical and Quantum Electronics*, Vol. 32, pp. 819–827, 2000.
- N. C. Chang and J. B. Gruber. Spectra and Energy Levels of Eu³⁺ in Y₂O₃. *Journal of Chemical Physics*, Vol. 41, No. 10, pp. 3227–3234, 15 November 1964.
- N. C. Chang, J. B. Gruber, R. P. Leavitt, and C. A. Morrison. Optical spectra, energy levels, and crystal-field analysis of tripositive rare earth ions in Y₂O₃. I. Kramers ions in C₂ sites. *Journal of Chemical Physics*, Vol. 76, No. 8, pp. 3877–3889, 15 April 1982.
- Y. G. Choi, K. H. Kim, Y. S. Han, and J. Heo. Sensitizing effect of Yb³⁺ on near-infrared fluorescence emission of Cr⁴⁺-doped calcium aluminate glasses. *Journal of Materials Research*, Vol. 15, No. 2, pp. 278–281, February 2000a.
- Y. G. Choi, K. H. Kim, S. H. Park, and J. Heo. Comparative study of energy transfers from Er³⁺ to Ce³⁺ in tellurite and sulfide glasses under 980 nm excitation. *Journal of Applied Physics*, Vol. 88, No. 7, pp. 3832–3839, 1 October 2000b.
- C. E. Chryssou, F. Di Pasquale, and C. W. Pitt. Improved Gain Performance In Yb³⁺-Sensitized Er³⁺-Doped Alumina (Al₂O₃) Channel Optical Waveguide Amplifier. *Journal of Lightwave Technology*, Vol. 19, No. 3, pp. 345–349, March 2001.
- C. E. Chryssou, C. W. Pitt, P. J. Chandler, and D. E. Hole. Photoluminescence characterisation of Er³⁺/Yb³⁺ co-implanted alumina (Al₂O₃) thin films and sapphire crystals. *IEE Proceedings Optoelectronics*, Vol. 145, No. 6, pp. 325–330, December 1998.
- T. Danger, J. Koetke, R. Brede, E. Heumann, G. Huber, and B. H. T. Chai. Spectroscopy and green up-conversion laser-emission of Er³⁺-doped crystals at room temperature. *Journal of Applied Physics*, Vol. 76, No. 3, pp. 1413–1422, 1 August 1994.

- G. De Marchi, F. Gonella, P. Mazzoldi, G. Battaglin, É. J. Knystautas, and C. Meneghini. Non-linear glasses by metal cluster formation: Synthesis and properties. *Journal of Non-Crystalline Solids*, Vol. 196, pp. 79–83, March 1996.
- J.-M. P. Delavaux, S. Granlund, O. Mizuhara, L. D. Tzeng, D. Barbier, M. Rattay, F. Saint André, and A. Kevorkian. Integrated Optics Erbium–Ytterbium Amplifier System in 10-Gb/s Fiber Transmission Experiment. *IEEE Photonics Technology Letters*, Vol. 9, No. 2, pp. 247–249, February 1997.
- N. D. Denkov, O. D. Velev, P. A. Kralchevsky, I. B. Ivanov, H. Yoshimura, and K. Nagayama. Mechanism of Formation of Two-Dimensional Crystals from Latex Particles on Substrates. *Langmuir*, Vol. 8, pp. 3183–3190, 1992.
- D. L. Dexter. A Theory of Sensitized Luminescence in Solids. *Journal of Chemical Physics*, Vol. 21, No. 5, pp. 836–850, May 1953.
- D. Faccio, P. Di Trapani, W. Borsella, F. Gonella, P. Mazzoldi, and A. M. Malvezzi. Measurement of the third-order nonlinear susceptibility of Ag nanoparticles in a wide spectral range. *Europhysics Letters*, Vol. 43, No. 2, pp. 213–218, 15 July 1998.
- M. Federighi and F. Di Pasquale. The Effect of Pair-Induced Energy Transfer on the Performance of Silica Waveguide Amplifiers with High $\text{Er}^{3+}/\text{Yb}^{3+}$ Concentrations. *IEEE Photonics Technology Letters*, Vol. 7, No. 3, pp. 303–305, March 1995.
- J. Fick, É. J. Knystautas, A. Villeneuve, F. Schiettekatte, S. Roorda, and K. A. Richardson. High photoluminescence in erbium-doped chalcogenide thin films. *Journal of Non-Crystalline Solids*, Vol. 272, pp. 200–208, 2000.
- C. Flytzanis, F. Hache, M. C. Klein, D. Ricard, and Ph. Roussignol. Nonlinear optics in composite materials. In E. Wolf, editor, *Progress in Optics XXIX*. Elsevier Science Publishers B.V., 1991.
- T. Förster. Zwischenmolekulare Energiewanderung und Fluoreszenz. *Zeitschrift für Naturforschung*, Vol. 2, pp. 55–75, 1948.
- M. Fujii, M. Yoshida, Y. Kanzawa, S. Hayashi, and Yamamoto. 1.54 μm photoluminescence of Er^{3+} doped into SiO_2 films containing Si nanocrystals: Evidence for energy transfer from Si nanocrystals to Er^{3+} . *Applied Physics Letters*, Vol. 71, No. 9, pp. 1198–1200, 1 September 1997.
- V. P. Gapontsev and N. S. Platonov. Migration-accelerated quenching in glasses activated by rare-earth ions. In Y. M. Yen, editor, *Dynamical Processes in Disordered Systems*. Aedermannsdorf, Switzerland, 1989.
- R. N. Ghosh, J. Shmulovich, C. F. Kane, M. R. X. de Barros, G. Nykolak, A. J. Bruce, and P. C. Becker. 8-mW Threshold Er^{3+} -Doped Planar Waveguide Amplifier. *IEEE Photonics Technology Letters*, Vol. 8, No. 4, pp. 518–520, April 1996.

- H. Giesche. Synthesis of monodisperse silica powders. II. Controlled growth reaction and continuous production process. *Journal of the European Ceramic Society*, Vol. 14, No. 3, pp. 205–214, 1994.
- C. Graf and A. van Blaaderen. Metallo-dielectric colloidal core-shell particles for photonic applications. *Langmuir*, accepted 2001.
- F. Hache, D. Ricard, and C. Flytzanis. Optical nonlinearities of small metal particles: surface-mediated resonance and quantum size effects. *Journal of the Optical Society of America B*, Vol. 3, No. 12, pp. 1647–1655, December 1986.
- Y. Hamanaka, A. Nakamura, S. Omi, N. Del Fatti, F. Vallée, and C. Flytzanis. Ultrafast response of nonlinear refractive index of silver nanocrystals embedded in glass. *Applied Physics Letters*, Vol. 75, No. 12, pp. 1712–1714, 20 September 1999.
- T. Hayakawa, S. T. Selvan, and M. Nogami. Enhanced fluorescence from Eu^{3+} owing to surface plasma oscillation of silver particles in glass. *Journal of Non-Crystalline Solids*, Vol. 259, pp. 16–22, 1999a.
- T. Hayakawa, S.T. Selvan, and M. Nogami. Field enhancement effect of small Ag particles on the fluorescence from Eu^{3+} -doped SiO_2 glass. *Applied Physics Letters*, Vol. 74, No. 11, pp. 1513–1515, 15 March 1999b.
- M. P. Hehlen, N. J. Cockroft, T. R. Gosnell, and A. J. Bruce. Spectroscopic properties of Er^{3+} - and Yb^{3+} -doped soda-lime silicate and aluminosilicate glasses. *Physical Review B*, Vol. 56, No. 15, pp. 9302–9317, 15 October 1997.
- T. H. Hoekstra. Erbium-Doped Y_2O_3 Integrated Optical Amplifiers. Ph.D. thesis, University of Twente, the Netherlands, March 1994.
- H. Hofmeister, W.-G. Drost, and A. Berger. Oriented prolate silver particles in glass – characteristics of novel dichroic polarizers. *NanoStructured Materials*, Vol. 12, pp. 207–210, 1999.
- H. Hövel, S. Fritz, A. Hilger, U. Kreibig, and M. Vollmer. Width of cluster plasmon resonances: Bulk dielectric functions and chemical interface damping. *Physical Review B*, Vol. 48, No. 24, pp. 18178–18188, 15 December 1993.
- B.-C. Hwang, S. Jiang, T. Luo, J. Watson, G. Serbello, and N. Peyghambarian. Cooperative upconversion and energy transfer of new high Er^{3+} - and Yb^{3+} - Er^{3+} -doped phosphate glasses. *Journal of the Optical Society of America B*, Vol. 17, No. 5, pp. 833–839, May 2000.
- D. Ila, E. K. Williams, C. C. Smith, D. P. Poker, D. K. Hensley, C. Klatt, and S. Kalbitzer. Post-implantation bombardment assisted formation of colloidal Au in silica. *Nuclear Instruments and Methods B*, Vol. 148, No. 1–4, pp. 1012–1016, January 1999.

- P. B. Johnson and R. W. Christy. Optical Constants of the Noble Metals. *Physical Review B*, Vol. 6, No. 12, pp. 4370–4379, 15 December 1972.
- P. Kabro, J. A. Capobianco, F. S. Ermeneux, R. Moncorgé, M. Bettinelli, and E. Cavalli. Excited state dynamics and energy transfer processes in $\text{YVO}_4:\text{Er}^{3+}$ crystals. *Journal of Applied Physics*, Vol. 82, No. 8, pp. 3983–3986, 15 October 1997.
- M. Karásek. Optimum Design of Er^{3+} - Yb^{3+} Codoped Fibers for Large-Signal High-Pump-Power Applications. *IEEE Journal of Quantum Electronics*, Vol. 33, No. 10, pp. 1699–1705, October 1997.
- A. Kawabata and R. Kubo. Electronic Properties of Fine Metallic Particles. II. Plasma Resonance Absorption. *Journal of the Physical Society of Japan*, Vol. 21, No. 9, pp. 1765–1772, September 1966.
- T. Kitagawa, K. Hattori, K. Shuto, M. Yasu, M. Kobayashi, and M. Horiguchi. Amplification in erbium-doped silica-based planar lightwave circuits. *Electronics Letters*, Vol. 28, pp. 1818–1819, 1992.
- U. Kreibig. Kramers Kronig Analysis of the Optical Properties of Small Silver Particles. *Zeitschrift für Physik*, Vol. 234, pp. 307–318, 1970.
- U. Kreibig. Electronic properties of small silver particles: the optical constants and their temperature dependence. *Journal of Physics F*, Vol. 4, pp. 999–1014, July 1974.
- C. Labbé, J.-L. Doualan, S. Girard, R. Moncorgé, and M. Thuau. Absolute excited state absorption cross section measurements in $\text{Er}^{3+}:\text{LiYF}_4$ for laser applications around $2.8\ \mu\text{m}$ and $551\ \text{nm}$. *Journal of Physics: Condensed Matter*, Vol. 12, pp. 6943–6957, 2000.
- P. Laporta, S. De Silvestri, V. Magni, and O. Svelto. Diode-pumped cw bulk $\text{Er}:\text{Yb}:\text{glass}$ laser. *Optics Letters*, Vol. 16, No. 24, pp. 1952–1954, 15 December 1991.
- J. A. Lázaro, J. A. Vallés, and M. A. Rebolledo. Determination of emission and absorption cross sections of Er^{3+} in $\text{Ti}:\text{LiNbO}_3$ waveguides from transversal fluorescence spectra. *Pure and Applied Optics*, Vol. 7, pp. 1363–1371, 1998.
- N. N. Lepeshkin, W. Kim, V. P. Safonov, J. G. Zhu, R. L. Armstrong, C. W. White, R. A. Zuhr, and V. M. Shalaev. Optical nonlinearities of metal-dielectric composites. *Journal of Nonlinear Optical Physics and Materials*, Vol. 8, No. 2, pp. 191–210, June 1999.
- C. Lester, A. Bjarklev, T. Rasmussen, and P. G. Dinesen. Modeling of Yb^{3+} -Sensitized Er^{3+} -Doped Silica Waveguide Amplifiers. *Journal of Lightwave Technology*, Vol. 13, No. 5, pp. 740–743, May 1995.

- D. E. McCumber. Einstein Relations Connecting Broadband Emission and Absorption Spectra. *Physical Review*, Vol. 136, No. 4A, pp. A954–A957, 16 November 1964.
- A. Meijerink, M. M. E. van Heek, and G. Blasse. Luminescence of Ag^+ in crystalline and glassy SrB_4O_3 . *Journal of Physics and Chemistry of Solids*, Vol. 54, No. 8, pp. 901–906, 1993.
- Z. Meng, T. Yoshimura, K. Fukue, M. Higashihata, Y. Nakata, and T. Okada. Large improvement in quantum fluorescence yield of Er^{3+} -doped fluorozirconate and fluoroindate glasses by Ce^{3+} codoping. *Journal of Applied Physics*, Vol. 88, No. 5, pp. 2187–2190, 1 September 2000.
- Z. Meng, T. Yoshimura, Y. Nakata, N. J. Vasa, and T. Okada. Improvement of Fluorescence Characteristics of Er^{3+} -Doped Fluoride Glass by Ce^{3+} Codoping. *Japanese Journal of Applied Physics*, Vol. 38, No. 12A, pp. L1409–L1411, 1 December 1999.
- M. Mesnaoui, M. Maazaz, C. Parent, B. Tanguy, and G. Le Flem. Spectroscopic properties of Ag^+ ions in phosphate glasses of NaPO_3 – AgPO_3 system. *European Journal of Solid State Inorganic Chemistry*, Vol. 29, pp. 1001–1013, 1992.
- G. Mie. Beiträge zur Physik trüber Medien, speziell kolloidaler Metallösungen. *Annalen der Physik*, Vol. 4, No. 25, pp. 377–445, 1908.
- W. J. Miniscalco and R. S. Quimby. General procedure for the analysis of Er^{3+} cross sections. *Optics Letters*, Vol. 16, No. 4, pp. 258–260, 15 February 1991.
- Y. Mita, T. Ide, M. Togashi, and H. Yamamoto. Energy transfer processes in Yb^{3+} and Tm^{3+} ion-doped fluoride crystals. *Journal of Applied Physics*, Vol. 85, No. 8, pp. 4160–4164, 15 April 1999.
- J. Nilsson, P. Scheer, and B. Jaskorzynska. Modeling and Optimization of Short Yb^{3+} -Sensitized Er^{3+} -Doped Fiber Amplifiers. *IEEE Photonics Technology Letters*, Vol. 6, No. 3, pp. 383–385, March 1994.
- A.-F. Obaton, J. Bernard, C. Parent, G. Le Flem, C. Labbé, P. Le Boulanger, and G. Boulon. Spectroscopic investigations of Yb^{3+} – Er^{3+} -codoped $\text{LaLiP}_4\text{O}_{12}$ glasses relevant for laser applications. *The European Physical Journal–Applied Physics*, Vol. 4, pp. 315–321, 1998.
- I. Okur, P. D. Townsend, and P. J. Chandler. New techniques for optical measurement of implanted nanoparticles in float glass. *Nuclear Instruments and Methods in Physics Research B*, Vol. 148, pp. 1069–1073, 1999.
- X. Orignac, D. Barbier, X. M. Du, R. M. Almeida, O. McCarthy, and E. Yeatman. Sol-gel silica/titania-on-silicon Er/Yb waveguides for optical amplification at $1.5\ \mu\text{m}$. *Optical Materials*, Vol. 12, pp. 1–18, 1999.

- D. H. Osborne, R. F. Haglund, F. Gonella, and F. Garrido. Laser-induced sign reversal of the nonlinear refractive index of Ag nanoclusters in soda-lime glass. *Applied Physics B*, Vol. 66, pp. 517–521, 1998.
- R. H. Page, K. I. Schaffers, P. A. Waide, J. B. Tassano, S. A. Payne, W. F. Krupke, and W. K. Bischel. Upconversion-pumped luminescence efficiency of rare-earth-doped hosts sensitized with trivalent ytterbium. *Journal of the Optical Society of America B*, Vol. 15, No. 3, pp. 995–1008, March 1998.
- D. P. Peters. Silver nanocrystals in sodalime glass. Master's thesis, FOM-Institute for Atomic and Molecular Physics, Amsterdam, The Netherlands, 1998.
- D. P. Peters, C. Strohhofer, M. L. Brongersma, J. van der Elsken, and A. Polman. Formation mechanism of silver nanocrystals made by ion irradiation of $\text{Na}^+ \leftrightarrow \text{Ag}^+$ ion-exchanged sodalime silicate glass. *Nuclear Instruments and Methods in Physics Research B*, Vol. 168, pp. 237–244, 2000.
- P. M. Peters, D. S. Funk, A. P. Peskin, D. L. Veasey, N. A. Sanford, S. N. Houde-Walter, and J. S. Hayden. Ion-exchanged waveguide lasers in $\text{Er}^{3+}/\text{Yb}^{3+}$ codoped silicate glass. *Applied Optics*, Vol. 38, No. 33, pp. 6879–6886, 20 November 1999.
- J. Qiu, M. Shojiya, Y. Kawamoto, and K. Kadono. Energy transfer process and Tb^{3+} up-conversion luminescence in $\text{Nd}^{3+}\text{-Yb}^{3+}\text{-Tb}^{3+}$ co-doped fluorozirconate glasses. *Journal of Luminescence*, Vol. 86, pp. 23–31, 2000.
- E. Radius. Optical characterization of Er-implanted Y_2O_3 waveguide films. Master's thesis, University of Amsterdam, The Netherlands, June 1994.
- R. V. Ramaswamy and R. Srivastava. Ion-Exchanged Glass Wave-Guides – a Review. *Journal of Lightwave Technology*, Vol. 6, No. 6, pp. 984–1002, June 1988.
- K. L. Shaklee, R. E. Nahory, and R. F. Leheny. Optical gain in semiconductors. *Journal of Luminescence*, Vol. 7, pp. 284–309, 1973.
- B. Simondi-Teisseire, B. Viana, D. Vivien, and A. M. Lejus. Yb^{3+} to Er^{3+} energy transfer and rate-equations formalism in the eye safe laser material $\text{Yb:Er:Ca}_2\text{Al}_2\text{SiO}_7$. *Optical Materials*, Vol. 6, pp. 267–274, 1996.
- L. H. Slooff, A. Polman, M. P. Oude Wolbers, F. C. J. M. van Veggel, D. N. Reinhoudt, and J. W. Hofstraat. Optical properties of erbium-doped organic polydentate cage complexes. *Journal of Applied Physics*, Vol. 83, No. 1, pp. 497–503, 1 January 1998.
- M. K. Smit. Integrated optics in silicon-based aluminium oxide. Ph.D. thesis, Optics Laboratory, Department of Applied Physics, Delft University of Technology, the Netherlands, 1991.
- M. K. Smit, C. J. van der Laan, and G. A. Acket. Aluminium oxide films for integrated optics. *Thin Solid Films*, Vol. 138, pp. 171–181, 1986.

- A. L. Stepanov, D. E. Hole, and P. D. Townsend. Reflectance of the dielectric layers containing metal nanoparticles formed by ion implantation. *Journal of Non-Crystalline Solids*, Vol. 244, pp. 275–279, 1999.
- W. Stöber, A. Fink, and E. Bohn. Controlled Growth of Monodisperse Silica Spheres in the Micron Range. *Journal of Colloid and Interface Science*, Vol. 26, No. 1, pp. 62–69, 1968.
- C. Strohhofer, P. G. Kik, and A. Polman. Selective modification of the Er^{3+} $^4\text{I}_{11/2}$ branching ratio by energy transfer to Eu^{3+} . *Journal of Applied Physics*, Vol. 88, No. 8, pp. 4486–4490, 15 October 2000.
- C. Strohhofer and A. Polman. Absorption and emission spectroscopy in Er^{3+} - Yb^{3+} doped aluminum oxide waveguides. *submitted to Optical Materials*, 2001.
- Y. P. Sun, J. E. Riggs, H. W. Rollins, and R. Guduru. Strong optical limiting of silver-containing nanocrystalline particles in stable suspension. *Journal of Physical Chemistry B*, Vol. 103, No. 1, pp. 77–82, 7 January 1999.
- S. Taccheo, P. Laporta, and C. Svelto. Widely tunable single-frequency erbium-ytterbium phosphate glass laser. *Applied Physics Letters*, Vol. 68, No. 19, pp. 2621–2623, 6 May 1996.
- S. Tanabe, T. Kouda, and T. Hanada. Excited energy migration and fluorescence decay in Yb-doped and Yb/Pr-codoped tellurite glasses. *Optical Materials*, Vol. 12, pp. 35–40, 1999.
- J. Tiggesbäumker, L. Köller, K.-H. Meiwes-Broer, and A. Liebsch. Blue shift of the Mie plasma frequency in Ag clusters and particles. *Physical Review A*, Vol. 48, No. 3, pp. R1749–R1752, September 1992.
- J. E. Townsend, W. L. Barnes, K. P. Jedrzejewski, and S. G. Grubb. Yb^{3+} sensitised Er^{3+} doped silica optical fibre with ultrahigh transfer efficiency and gain. *Electronics Letters*, Vol. 27, No. 21, pp. 1958–1959, 10 October 1991.
- M. Tsuda, K. Soga, H. Inoue, and A. Makishima. Comparison between the calculated and measured energy transfer rates of the $^4\text{S}_{3/2}$ state in Er^{3+} -doped fluorozirconate glasses. *Journal of Applied Physics*, Vol. 88, No. 4, pp. 1900–1906, 15 August 2000.
- E. Valentin, H. Bernas, C. Ricolleau, and F. Creuzet. Ion Beam "Photography": Decoupling Nucleation and Growth of Metal Clusters in Glasses. *Physical Review Letters*, Vol. 86, No. 1, pp. 99–102, 1 January 2001.
- A. van Blaaderen, K. P. Velikov, J. P. Hoogenboom, D. L. J. Vossen, A. Yethiraj, R. Dullens, T. van Dillen, and A. Polman. Manipulation of colloidal crystallization for photonic applications: from self-organization to do-it-yourself organization. In C. M. Soukoulis, editor, *Photonic Crystals and Light Localization in the 21st Century*. Kluwer Academic, Dordrecht, 2001.

- G. N. van den Hoven, R. J. I. M. Koper, A. Polman, C. van Dam, J. W. M. van Uffelen, and M. K. Smit. Net optical gain at $1.53\ \mu\text{m}$ in Er-doped Al_2O_3 waveguides on silicon. *Applied Physics Letters*, Vol. 68, No. 14, pp. 1886–1888, 1 April 1996a.
- G. N. van den Hoven, E. Snoeks, A. Polman, C. van Dam, J. W. M. van Uffelen, and M.K. Smit. Upconversion in Er-implanted Al_2O_3 waveguides. *Journal of Applied Physics*, Vol. 79, No. 3, pp. 1258–1266, 1 February 1996b.
- G. N. van den Hoven, J. A. van der Elsken, A. Polman, C. van Dam, J. W. M. van Uffelen, and M.K. Smit. Absorption and emission cross sections of Er^{3+} in Al_2O_3 waveguides. *Applied Optics*, Vol. 36, No. 15, pp. 3338–3341, 20 May 1997.
- H. J. van Weerden, T. H. Hoekstra, P. V. Lambeck, and T. J. A. Popma. Low-threshold amplification at $1.5\ \mu\text{m}$ in Er: Y_2O_3 IO-amplifier. In *Proceedings of the 8th European Conference on Integrated Optics*, page 169. Royal Institute of Technology, Stockholm, Sweden, 1997.
- D. L. Veasey, D. S. Funk, P. M. Peters, N. A. Sanford, G. E. Obarski, N. Fontaine, M. Young, A. P. Peskin, W.-C. Liu, S. N. Houde-Walter, and J. S. Hayden. Yb/Er-codoped and Yb-doped waveguide lasers in phosphate glass. *Journal of Non-Crystalline Solids*, Vol. 263&264, pp. 369–381, 2000.
- M. V. D. Vermelho, U. Peschel, and J. S. Aitchison. Simple and Accurate Procedure for Modeling Erbium-Doped Waveguide Amplifiers with High Concentration. *Journal of Lightwave Technology*, Vol. 18, No. 3, pp. 401–408, March 2000.
- M. A. Villegas, J. M. Fernández Navarro, S. E. Paje, and J. Llopis. Optical spectroscopy of a soda lime glass exchanged with silver. *Physics and Chemistry of Glasses*, Vol. 37, No. 6, pp. 248–253, 6 December 1996.
- Y. Watanabe, M. Inoue, and T. Tsuchiya. Intensity-dependent photobleaching through bulk oxide glass containing silver particles. *Journal of Applied Physics*, Vol. 84, No. 11, pp. 6457–6459, 1 December 1998.
- P. F. Wysocki, N. Park, and D. DiGiovanni. Dual-stage erbium-doped erbium/ytterbium-codoped fiber amplifier with up to +26 dBm output power and a 17 nm flat spectrum. *Optics Letters*, Vol. 21, No. 21, pp. 1744–1746, 1 November 1996.
- C. Wyss, W. Lüthy, H. P. Weber, P. Rogin, and J. Hulliger. Energy transfer in $\text{Yb}^{3+}:\text{Er}^{3+}:\text{YLF}$. *Optics Communications*, Vol. 144, pp. 31–35, 1 December 1997.
- N. Yamada, S. Shionoya, and T. Kushida. Phonon-Assisted Energy Transfer between Trivalent Rare Earth Ions. *Journal of the Physical Society of Japan*, Vol. 32, No. 6, pp. 1577–1586, June 1972.
- Y. C. Yan, A. J. Faber, H. de Waal, P. G. Kik, and A. Polman. Erbium-doped phosphate glass waveguide on silicon with 4.1 dB/cm gain at $1.535\ \mu\text{m}$. *Applied Physics Letters*, Vol. 71, No. 20, pp. 2922–2924, 17 November 1997.

- B. Zandi, L. D. Merkle, J. A. Hutchinson, H. R. Verdun, and B. H. T. Chai. Upconversion and energy transfer modeling in Er,Yb:CaYAlO₄. *Journal de Physique IV*, Vol. 4, pp. C4-587—C4-590, April 1994.
- J. F. Ziegler, J. P. Biersack, and U. Littmark. *The Stopping and Range of Ions in Solids*. Pergamon, New York, 1985.

Summary

Integrated optics, the part of optical communication technology dealing with signal processing in small components, tries to functionalise data handling processes on a single optical chip in order to save cost and space. While data transfer via optical fibres is well established, concepts and materials for data processing (routing, amplification, reshaping, switching, filtering) in integrated optical waveguides have met with difficulties due to the small interaction length between light and matter.

This thesis focusses on two issues concerning materials with potential applications in all optical data processing: increasing the efficiency of erbium doped optical amplifiers by introducing a second dopant besides erbium into the waveguide material, and the fabrication and optical properties of nanometer-size silver crystals in optical waveguides on glass that may be used in filters or optical switches.

Part I is devoted to the study of energy transfer between dopants as a means to increase the efficiency of erbium doped amplifiers. Erbium ions have an electronic transition which can be used for amplification of light around 1540 nm, the standard wavelength for optical communication. Chapters 2 and 3 investigate a method to increase the transition rate between the second and first excited states of erbium in Y_2O_3 . These two energy levels are the one excited by the pump radiation at 980 nm and the one involved in the stimulated emission for amplification, respectively. In materials with low phonon energies the transition rate between them is low. As a consequence, energy is lost in radiative de-excitation of the second excited state to the ground state. To alleviate the transition bottleneck we introduce the rare earth ions europium and cerium, that both have levels at such energies that they can serve as acceptors for the energy difference between the Er^{3+} states. We show that Er^{3+} indeed transfers the energy difference between its first two excited states to the codopant. Energy transfer to Eu^{3+} is more efficient than toward Ce^{3+} , which can be made plausible from the exact energy level spectra of the two ions.

In the two subsequent chapters we study waveguides of Al_2O_3 doped with erbium and ytterbium. Absorption by Yb^{3+} together with energy transfer to Er^{3+} is more efficient than direct pumping of Er^{3+} around 980 nm. In chapter 4 we measure ab-

sorption and emission cross sections of Yb^{3+} and of various energy levels of Er^{3+} in Al_2O_3 . Subsequently we evaluate the efficiency of the energy transfer between Yb^{3+} and Er^{3+} . Codoping with Yb^{3+} can increase the photoluminescence output of Er^{3+} at 1530 nm by an order of magnitude. Chapter 5 makes use of the measured data on cross sections and energy transfer to numerically estimate the gain in an erbium doped waveguide amplifier sensitised with Yb^{3+} . Our calculations reveal the need to carefully adjust the Yb^{3+} concentration with respect to waveguide length, available pump power, and required gain. Doping with high Yb^{3+} concentrations, for instance, leads to enhanced gain at short waveguide lengths. However, the strong absorption of Yb^{3+} at the wavelength of the pump limits the length of the waveguide over which gain can be obtained.

In chapter 6 we describe sensitising of Er^{3+} in silicate glass doped with silver. The silver was introduced into the glass by an ion exchange process as used for waveguide fabrication. Sensitisation apparently involving pairs of silver ions/atoms is observed for excitation in the visible and ultraviolet. A photoluminescence enhancement of a factor of 70 is achieved when exciting at 488 nm.

The topic of part II of this thesis are nanometre-scale crystals of silver in silicate glass. This composite material has interesting optical properties: their absorption spectrum is dominated by a strong band in the blue caused by the excitation of surface plasmons in the nanocrystals. Paired with this absorption (described by the imaginary part of the index of refraction) is a large variation of the real part of the index of refraction over the visible spectral range.

Chapter 7 describes the formation mechanism of silver nanocrystals in glass: Ag^+ ions are introduced into the glass by $\text{Na}^+ \longleftrightarrow \text{Ag}^+$ ion exchange in a silver salt melt. Irradiation of such an ion-exchanged glass with different ions of an energy of several hundred keV gives rise to the formation of silver nanocrystals with average sizes in the 1 – 2 nm range. According to our data, the formation mechanism is related to the energy deposited in atomic displacement collisions during the irradiation.

The two subsequent chapters give examples of applications of glass/silver nanocrystal composites fabricated in this way. In chapter 8 we estimate the complex index of refraction of the composite from reflection and transmission measurements. Transmission measurements through ion-exchanged waveguides containing regions of different length doped with silver nanocrystals show that these waveguides act as long-wavelength pass filters, with the cutoff wavelength determined by the length of the region containing silver nanocrystals. Finally, in chapter 9 we make use of the elevated index of refraction of the composite in the visible to write an index grating into glass. The ion irradiation to form silver nanocrystals was performed through a self-organised mask of colloidal silica particles. Light scattering experiments confirm the existence of an index grating with hexagonal symmetry.

The study of the optical properties of materials engineered on the atomic scale, as presented here, has led to insights into their functionality for applications in integrated optics. Based on this knowledge, integrated components with new or improved functionality may be developed in the time to come.

Samenvatting

Geïntegreerde optica is het onderdeel van de optische communicatietechnologie dat zich bezighoudt met signaalverwerking in kleine componenten, en heeft als doel ruimte en kosten te besparen. Terwijl dataoverdracht middels optische vezels algemeen in gebruik is, blijkt optische dataverwerking in geïntegreerde schakelingen moeilijk wegens de korte interactielengte tussen licht en materie.

Dit proefschrift behandelt twee thema's die met de ontwikkeling van materialen voor toepassingen in de optische dataverwerking te maken hebben: 1) het bevorderen van de efficiëntie van erbium-gedoteerde optische versterkers door middel van de introductie van een tweede soort ion in het lichtgeleider materiaal, en 2) de fabricage en optische eigenschappen van zilverkristallen met een diameter van enkele nanometers in optische lichtgeleiders gebaseerd op glas. De laatste kunnen worden toegepast als filters, optische schakelaars of in fotonische kristallen.

Deel I van dit proefschrift behandelt de energieoverdracht tussen de zeldzaamaardionen als een manier om de efficiëntie van met erbium gedoteerde planaire lichtversterkers te verbeteren. Erbium ionen hebben een elektronische overgang die voor de versterking van licht met een golflengte van 1540 nm gebruikt kan worden. Hoofdstukken 2 en 3 onderzoeken een methode om de overgangswaarschijnlijkheid tussen het tweede en eerste aangeslagen niveau van Er^{3+} in Y_2O_3 te vergroten. Optisch pompen met 980 nm-licht brengt de ionen in hun tweede aangeslagen niveau, terwijl de gestimuleerde emissie plaats vindt vanaf het eerste aangeslagen niveau. In materialen met een lage fononenenergie is de overgangswaarschijnlijkheid tussen de twee aangeslagen niveaus laag. Daardoor gaat energie verloren door stralend verval vanaf het tweede niveau. Om de overgangswaarschijnlijkheid te verhogen wordt europium of cerium toegevoegd. Deze zeldzame aardmetalen werken als ontvangers van de energie tussen de twee aangeslagen toestanden van Er^{3+} door middel van energieoverdracht. Energieoverdracht naar europium is efficiënter dan naar cerium, wat uit de precieze energieniveauschema's van deze ionen kan worden verklaard.

In de twee volgende hoofdstukken worden lichtgeleiders van Al_2O_3 beschreven, die met erbium en ytterbium gedoteerd zijn. Absorptie van 980 nm pompricht door Yb^{3+} gevolgd door energieoverdracht naar Er^{3+} is efficiënter dan direct pompen van Er^{3+} . In hoofdstuk 4 worden werkzame doorsneden voor absorptie en emissie van Yb^{3+} en Er^{3+} in Al_2O_3 bepaald. Ook wordt het rendement van energieoverdracht tussen Er^{3+} en Yb^{3+} bestudeerd. Codoteren met Yb^{3+} verhoogt de luminescentie opbrengst van Er^{3+} bij 1530 nm met een factor 10. Hoofdstuk 5 gebruikt de gemeten data uit

hoofdstuk 4 om numeriek de versterking te berekenen in een optische versterker die gedoteerd is met erbium en ytterbium. De resultaten laten zien dat de concentratie van Yb^{3+} geoptimaliseerd moet worden naar gelang de lengte van de lichtgeleider, het beschikbaar pompvermogen, en de gewenste versterking. Doteren met Yb^{3+} leidt tot grotere versterking voor korte lichtgeleiders. Maar de sterke absorptie van Yb^{3+} bij de pompgolflengte beperkt de lengte van de lichtgeleider waarover versterking behaald kan worden.

Hoofdstuk 6 beschrijft de optische eigenschappen van Er^{3+} in silicaatglas dat tevens is gedoteerd met zilver. De zilverdoting vindt plaats met een ionenuitwisselingsproces zoals gebruikelijk voor het maken van optische lichtgeleiders. De aanwezigheid van zilverionen vergroot het excitatierendement van de Er^{3+} ionen met een factor 70 bij een excitatiegolflengte van 488 nm. Dit verschijnsel lijkt met paren van zilverionen/-atomen te maken te hebben.

Het onderwerp van deel II van dit proefschrift zijn kleine zilverkristallen met afmetingen van enkele nanometers in silicaatglas. Deze composietmaterialen tonen interessante optische eigenschappen: hun absorptiespectrum wordt gedomineerd door een sterke band in het blauw, veroorzaakt door de excitatie van oppervlakteplasmonen in de nanokristallen. Deze absorptie (die door het imaginaire deel van de brekingsindex wordt beschreven) is gerelateerd aan een grote variatie van het reële deel van de brekingsindex over het hele zichtbare spectrum. Hoofdstuk 7 beschrijft het formatiemechanisme van zilver nanokristallen in silicaatglas: het glas wordt met Ag^+ ionen gedoteerd door middel van een $\text{Na}^+ \longleftrightarrow \text{Ag}^+$ ionenuitwisseling in een gesmolten zilverzoutbad. Bestraling van het Ag^+ gedoteerde glas met verschillende ionen met energien van enige honderden keV's leidt tot de vorming van zilver nanokristallen met een gemiddelde diameter van 1 – 2 nm. De data laten zien dat het vormingsmechanisme gerelateerd is aan de energie die tijdens de bestraling in atoom-verplaatsingsbotsingen gedeponeerd wordt. De twee volgende hoofdstukken zijn voorbeelden van toepassingen van glas/zilver nanokristal-composietmaterialen, gemaakt op de boven beschreven manier. In hoofdstuk 8 wordt de complexe brekingsindex van het composietmateriaal geschat aan de hand van reflectie- en transmissie-metingen. Optische transmissiemetingen door lichtgeleiders, die over verschillende lengtes met zilver nanokristallen gedoteerd zijn, laten zien dat zulke lichtgeleiders als laagdoorlaatfilters gebruikt kunnen worden. Hun afkapgolflengte wordt door de lengte van het gebied met de zilver nanokristallen bepaald. In hoofdstuk 9 wordt de verhoogde brekingsindex van het composietmateriaal gebruikt om een indextralie in glas te schrijven. Hiertoe wordt de ionenbestraling voor de vorming van zilver nanokristallen uitgevoerd door een masker van colloïdale silicadeeltjes die door een zelforganisatieproces een hexagonaal patroon vormden. Lichtverstrooiingsmetingen bevestigen het bestaan van een indextralie.

De bestudering van de optische eigenschappen van op atomaire schaal gemodificeerde materialen, zoals hier gepresenteerd, geeft inzicht in de toepasbaarheid van zulke materialen voor geïntegreerde optica. Gebaseerd op deze kennis kunnen in toekomst geïntegreerde componenten met nieuwe of verbeterde functionaliteit ontwikkeld worden.

Zusammenfassung

Integrierte Optik ist der Teil der optischen Kommunikationstechnologie, der sich mit Signalverarbeitung in kleinen optischen Komponenten beschäftigt. Ihr Ziel ist die platz- und kostensparende Implementierung von Signalverarbeitungsprozessen auf einem optischen Chip. Während die Datenübertragung mit optischen Fasern bereits weit verbreitet ist, leiden Konzepte und Materialien für Signalverarbeitung (wie Verstärker, Schalter, Filter) unter Problemen, die durch die geringe Wechselwirkungslänge zwischen Licht und Materie in optischen Wellenleitern entstehen.

Diese Dissertation behandelt zwei verschiedene Sorten Materialien und ihre möglichen Anwendungen in der optischen Signalverarbeitung: Erstens, Materialien, die die Effektivität von mit Erbium dotierten Lichtverstärkern durch das Einbringen einer zweiten Ionensorte verbessern. Zweitens, Glaswellenleiter, die nanometergroße Silberkristalle enthalten und für die Herstellung von Filtern oder optischen Schaltern von Interesse sein können.

Teil I ist der Untersuchung von Energieübertrag zwischen zwei Ionenspezies gewidmet, durch den die Effektivität von Erbiumverstärkern erhöht werden kann. Erbiumionen besitzen einen Elektronenübergang, der für Verstärkung von Licht um die 1540 nm, der Standardwellenlänge für optische Datenübertragung, gebraucht werden kann. Kapitel 2 und 3 behandeln eine Methode zur Erhöhung der Übergangswahrscheinlichkeit zwischen dem zweiten und ersten angeregten Energieniveau von Erbium in Y_2O_3 . Diese zwei Zustände sind das Pumpniveau für Anregung bei 980 nm bzw. das Niveau, von dem stimulierte Emission ausgeht. In Materialien mit niedriger Phononenenergie ist die Übergangswahrscheinlichkeit zwischen diesen beiden Zuständen niedrig. Als Folge daraus geht Energie in Form von Strahlung (Abregung zum Grundzustand) verloren. Um die Übergangswahrscheinlichkeit zwischen den beiden angeregten Niveaus zu vergrößern, bringen wir Europium- und Ceriumionen in das Material ein. Dadurch kann gezeigt werden, daß diese zwei Ionen als Akzeptoren für die Energie zwischen den angeregten Zuständen von Er^{3+} dienen, wobei der Energieübertrag auf Eu^{3+} effizienter ist als auf Ce^{3+} . Letzteres folgt aus der Lage der Energiezustände der beiden Ionen.

In den zwei folgenden Kapiteln untersuchen wir Al_2O_3 Wellenleiter, die mit Erbium und Ytterbium dotiert sind. Bei einer Anregung mit Licht bei 980 nm ist die Anregung von Er^{3+} nach Absorption des Lichts durch Yb^{3+} und anschließendem Energieübertrag effizienter als das direkte Pumpen der Er^{3+} Ionen. In Kapitel 4 bestimmen wir die Absorptions- und Emissionsquerschnitte von Yb^{3+} und verschiedener

Energieniveaus von Er^{3+} in Al_2O_3 . Außerdem messen wir die Effizienz des Energieübertrags zwischen Yb^{3+} und Er^{3+} . Dotierung mit Yb^{3+} führt zu einer um bis zu eine Größenordnung erhöhten Photolumineszenz von Er^{3+} . Kapitel 5 verwendet die Daten für die Querschnitte und den Energieübertrag für eine numerische Abschätzung der Verstärkung in einem mit Erbium und Ytterbium dotierten integriert-optischen Verstärker. Unsere Berechnungen zeigen, daß die Yb^{3+} Konzentration gut an andere Parameter des Verstärkers wie Wellenleiterlänge, vorhandene Pumpleistung und gewünschte Verstärkung angepasst werden muß. Eine hohe Yb^{3+} Konzentration führt einerseits zu erhöhter Verstärkung in kurzen Wellenleitern, die starke Absorption der Yb^{3+} Ionen beschränkt andererseits die Länge der erbiumdotierten Wellenleiter. In Kapitel 6 beschreiben wir die Erhöhung der Photolumineszenz von Er^{3+} in Silikatglas, welches Silber enthält. Ag wird mittels eines Ionenaustauschprozesses, wie für die Herstellung von optischen Wellenleitern gebräuchlich, in das Glas eingebracht. Die Photolumineszenz wird bei Anregung mit 488 nm um einen Faktor 70 erhöht. Sie kann im ganzen sichtbaren und ultravioletten Spektralbereich angeregt werden, was wir auf einen Energieübertrag von einem Silberatom-/ionenpaar auf Er^{3+} zurückführen.

Teil II widmet sich Silbernanokristallen in Silikatglas. Dieses Kompositmaterial besitzt interessante optische Eigenschaften: Sein Absorptionsspektrum wird von einem starken Band im blauen Spektralbereich beherrscht, das durch die Anregung von Oberflächenplasmonen in den Nanokristallen erzeugt wird. Mit dieser Absorption geht eine starke Veränderung des Realteils des Brechungsindex im Sichtbaren einher. Kapitel 7 beschreibt die Erzeugung von Silbernanokristallen in Glas: Ag^+ Ionen werden mittels eines $\text{Na}^+ \longleftrightarrow \text{Ag}^+$ Ionenaustauschs in einem Bad aus geschmolzenem Silbersalz in das Glas eingebracht. Bestrahlung mit verschiedenen Ionen bei einer Ionenenergie von einigen hundert keV führt zur Entstehung von Silberkristallen mit einer durchschnittlichen Größe von 1 – 2 nm. Unsere Messungen zeigen, daß der Entstehungsmechanismus abhängt von der Energie, die während der Bestrahlung in Kollisionen zwischen Ionen und Atomen freikommt. Die zwei folgenden Kapitel behandeln Beispiele für Anwendungen der beschriebenen Glas/Silbernanokristall Kompositmaterialien. In Kapitel 8 schätzen wir den komplexen Brechungsindex eines Komposits mit Hilfe von Reflektions- und Transmissionsmessungen ab. Transmissionsmessungen durch ionenausgetauschte Wellenleiter, die auf Teilstücken Silbernanokristalle enthalten, zeigen, daß diese Wellenleiter Tiefpassfilter darstellen. Ihre Grenzwellenlängen werden durch die Länge des Teilstücks mit Nanokristallen bestimmt. Schließlich verwenden wir in Kapitel 9 den erhöhten Brechungsindex des Komposits im Sichtbaren, um ein Indexgitter in Glas zu schreiben. Die Ionenbestrahlung zur Erzeugung der Silbernanokristalle findet dabei durch eine selbstorganisierende Maske aus kolloidalen SiO_2 Teilchen statt. Lichtstreuungsmessungen an dieser Struktur bestätigen die Existenz eines Indexgitters mit hexagonaler Symmetrie.

Die in dieser Dissertation beschriebenen Untersuchungen der optischen Eigenschaften von Materialien, die auf einer atomaren Skala modifiziert wurden, führt zu besserem Verständnis ihrer Anwendbarkeit in der integrierten Optik. Auf der Basis dieser Kenntnis können in Zukunft integriert-optische Komponenten mit neuer oder verbesserter Funktionalität entwickelt werden.

Publications

This thesis is based on the following publications:

- Chapter 2: *Selective modification of the $Er^{3+} {}^4I_{11/2}$ branching ratio by energy transfer to Eu^{3+}*
C. Strohhöfer, P. G. Kik, and A. Polman
Journal of Applied Physics, Vol. 88, No. 8, pp. 4486–4490, 15 October 2000
- Chapter 3: *Enhancement of $Er^{3+} {}^4I_{13/2}$ population in Y_2O_3 by energy transfer to Ce^{3+}*
C. Strohhöfer and A. Polman
Optical Materials, Vol. 17, No. 4, pp. 445–451, August 2001
- Chapter 4: *Absorption and emission spectroscopy in Er^{3+} - Yb^{3+} doped aluminum oxide waveguides*
C. Strohhöfer and A. Polman
submitted to Optical Materials
- Chapter 5: *Relationship between gain and Yb^{3+} concentration in Er^{3+} - Yb^{3+} doped waveguide amplifiers*
C. Strohhöfer and A. Polman
Journal of Applied Physics, Vol. 90, No. 9, pp. 4314–4320, 1 November 2001
- Chapter 6: *Energy transfer to Er^{3+} in Ag ion-exchanged glass*
C. Strohhöfer and A. Polman
submitted to Applied Physics Letters
- Metal-sensitized planar optical amplifier*
C. Strohhöfer, A. Polman, and E. Demaray
provisional patent application

- Chapter 7: *Formation mechanism of silver nanocrystals made by ion irradiation of $\text{Na}^+ \leftrightarrow \text{Ag}^+$ ion-exchanged sodalime silicate glass*
D. P. Peters, C. Strohhofer, M. L. Brongersma, J. van der Elsken, and A. Polman
Nuclear Instruments and Methods in Physics Research B, Vol. 168, No. 2, pp. 237–244, 2 June 2000
- Chapter 8: *Silver nanocrystal doped waveguides with controlled transmission*
C. Strohhofer and A. Polman
submitted to the Journal of the Optical Society of America B
- Chapter 9: *Highly dispersive micropatterns in ion-exchanged glass formed by ion irradiation through a mask of colloidal particles*
C. Strohhofer, J. P. Hoogenboom, and A. Polman
submitted to Advanced Materials

Related publications, to which the author contributed:

Active optical properties of Er-containing crystallites in sol-gel derived glass films

C. Strohhofer, J. Fick, H. C. Vasconcelos, and R. M. Almeida

Journal of Non-Crystalline Solids, Vol. 226, No. 1–2, pp. 182–191, 16 June 1998

Active optical properties of erbium-doped GeO_2 -based sol-gel planar waveguides

C. Strohhofer, S. Capecchi, J. Fick, A. Martucci, G. Brusatin, and M. Guglielmi

Thin Solid Films, Vol. 326, No. 1–2, pp. 99–105, 4 August 1998

Fabrication and Characterization of Sol-Gel GeO_2 - SiO_2 Erbium-Doped Planar Waveguides

A. Martucci, G. Brusatin, M. Guglielmi, C. Strohhofer, J. Fick, S. Pelli and G. C. Righini

Journal of Sol-Gel Science and Technology, Vol. 13, No. 1–3, pp. 535–539, 1998

Dankwoord

Allereerst bedank ik mijn promotor Albert Polman. Hij gaf mij de kans om dit onderzoek op Amolf te verrichten. Al liep de planning niet altijd synchroon, de samenwerking was toch succesvol.

Verder zou het leven in de groep veel minder interessant geweest zijn zonder mijn collega promovendi Mark Brongersma en Pieter Kik, Michiel de Dood en Lenneke Slooff, Teun van Dillen en Jeroen Kalkman. Ik wil ze danken voor de inspirerende discussies over fysica en algemeen.

Veel steun had ik ook aan andere mensen in de groep. Veel kwamen en vertrokken in de tijd die ik hier zat. Bedankt, studenten Daniel Peters en Freek Suyver, Dirk Vossen, Michael Hensen, Max Siem, Joan Penninkhof, en postdocs Edwin Snoeks, Nicolas Hamelin, José dos Santos. Ook de gasten van de groep, Hideo Isshiki, Sjoerd Roorda, Regina Ragan en Tadamasa Kimura, wil ik hier heel hartelijk bedanken.

Jan van der Elsen, die altijd probeerde om mij aan de wijn te krijgen, is dit nooit gelukt, maar heeft me weten te doordringen met scheikundige ideeën en daarmee mijn nauwe blikveld verruimd.

Ook de technici van onze groep,
Johan Derks en Jan ter Beek, bedankt.
Jullie hielden met veel expertise
de machines aan de praat en maakten
het zo mogelijk efficiënt te werken.

Dan ben ik van het Amolf nog een paar
collega's dank verschuldigd voor hun hulp:
Hans Zeijlemaker, Ad de Snaijer, Hester
Volten en Wim van der Zande. Met
hun inzet maakten zij de lichtverstrooiings-
metingen voor dit proefschrift mogelijk.

Het waveguidewerk kwam tot stand met de
hulp van Koos van Uffelen en Tony
Zijlstra. Het polijstwerk aan de waveguides
werd door René Koper perfect gedaan.

Zonder yttriumoxide laagjes
gemaakt door Harm van Weerden en Paul Lambeck
was een groot gedeelte van dit proefschrift
niet mogelijk geweest. Ed Vlietstra hielp
snel en effectief met de metingen
op zijn Cary photospektrometer.

Dank komt ook het hele Amolf toe
voor het scheppen van een sfeer waarin
succesvol werk bevorderd wordt. In het
bijzonder wil ik Jacob Hoogenboom
voor de goede samenwerking danken.
Georgiana Languri stond altijd
voor me klaar met een luisterend oor.

Ten slotte wil ik nog mijn ouders danken
voor hun begrip en steun, die zij door al die
jaren heen aan mij hebben gegeven.
Ik moet het deels aan hun opvoeding wijden
dat ik dit proefschrift af heb kunnen maken.

Curriculum Vitae

Op 22 juni 1970 ben ik geboren te Nürnberg. In 1988 behaalde ik het Amerikaanse high school diploma aan de John Stark Regional High School in Weare, New Hampshire, en in 1990 de Abitur aan het Melanchthon Gymnasium in Nürnberg. Na aan mijn dienstplicht te hebben voldaan ben ik natuurkunde gaan studeren aan de Universität Karlsruhe (TH). Tijdens mijn studie beleefde ik een schitterend jaar als Erasmusstipendiaat aan het Trinity College Dublin in Ierland, en volgde de opleiding tot het Diplome d'Etudes Approfondis in de vakrichting Optique, Optoélectronique et Microondes aan het Institut National Polytechnique in Grenoble. Mijn afstudeerwerk, "Caractérisation des propriétés actives des terres rares dans des couches minces vitreuses fabriquées par sol-gel", heb ik eveneens in Grenoble verricht, en wel aan het Laboratoire d'Electromagnétisme Microondes et Optoélectronique, onder begeleiding van Dr. Jochen Fick. In September 1997 behaalde ik het Diplom in de natuurkunde aan de Universität Karlsruhe. In oktober 1997 begon ik met mijn promotieonderzoek aan nieuwe materialen voor de optoelectronica op het FOM-Instituut voor Atoom- en Molecuulfysica in Amsterdam. De resultaten van dat onderzoek staan beschreven in dit proefschrift.